UNIVERSITÀ DEGLI STUDI DI BARI ALDO MORO

Dipartimento Interateneo di Fisica "M. Merlin"

Dottorato di Ricerca in Fisica

XXIV Ciclo

Settore Scientifico Disciplinare: FIS/01

Tesi di Dottorato

Inclusive charged hadrons production in pp collisions with the ALICE-HMPID detector at the LHC

Dott. Francesco Barile

UNIVERSITÀ DEGLI STUDI DI BARI ALDO MORO

Dipartimento Interateneo di Fisica "M. Merlin"

Dottorato di Ricerca in Fisica

XXIV Ciclo

Settore Scientifico Disciplinare: FIS/01

Tesi di Dottorato

Inclusive charged hadrons production in pp collisions with the ALICE-HMPID detector at the LHC

Dottorando:

Francesco Barile

Coordinatore:

Ch.ssimo Prof. F. Romano

Supervisore:

Prof. D. Di Bari

ESAME FINALE 2012

Contents

Introduction

The Large Hadron Collider (LHC), the world's largest and highest-energy particle accelerator is designed to address fundamental questions about matter and the origin of the Universe. The LHC lies in a tunnel 27 km in circumference, as deep as 175 m beneath the Franco-Swiss border near Geneva, Switzerland. It brings to collide both proton and heavy-ion beams with a center-of-mass energy never reached before. It can recreates the conditions just after the Big Bang by colliding heavy-ion beams head-on at extremely high energy. The study of the nuclear matter under extreme conditions represents the main task of the ALICE experiment, the dedicated heavy-ion detector at LHC. It also studies proton-proton collisions, both as a benchmark sample to understand the Pb-Pb collisions and to carry out p-p physics studies connected to the exploration of a new energy domain and to access to the region of low Bjorken-x value. The goal of this thesis is the study of the particles identification provided by a small acceptance detector: the High Momentum Particle IDentification detector. Installed during September 2006 and located at about 5 m from the primary vertex, it can contribute to several ALICE physics items using the Cherenkov radiation.

This thesis is made of 5 chapters. An overview of the Heavy Ion collisions, the Quark Gluon Plasma, and the main points of the ALICE physics program are described in the first chapter. Some recent results on particles production and hadron ratios are also presented. Chapter 2 is dedicated to the LHC machine, to the ALICE apparatus and to the High Momentum Particle Detector. The layout, the principle of operation and some recent performance results of this RICH detector will be described. Chapter 3 is dedicated to the evaluation of the HMPID PID efficiency. This study exploit the unique possibility to extract the efficiency directly from data using the V^0's decay. Also, it provides a comparison with Monte-Carlo simulation. A detailed description of this study is presented. In addition, the measurement of the refractive index of the C_6F_{14} radiator in the HMPID chamber has been carried out. The main topic of the thesis is presented in Chapter 4. The measurement of the pions, kaons and protons spectra and hadrons ratios (π^-/π^+, K^-/K^+ and $\bar{p}/p$) in pp collisions at $\sqrt{s}$ = 7 TeV is presented. All the correction factors, MC and data comparison and systematics uncertainties will be described. The results will be discussed and compared with previous experiments. The end of this thesis (Chapter 5) is dedicated to *work in progress* item: the HMPID analysis in pp collisions at $\sqrt{s}$ = 2.76 TeV. Preliminary raw spectra and ratios will be presented.

The small geometrical acceptance of the HMPID motivated a trigger study (Appendix D) with the aim to select interesting events for the HMPID. The use of a dedicated trigger could allow fast and simple performance studies (alignment and calibration, for example), but not only this. It could be used in the HMPID physics analysis. This study and its results will be presented.

Chapter 1

Physics with ALICE at LHC

1.1 Heavy Ion collisions and Quark Gluon Plasma

The main goal of the ultra-relativistic heavy-ion collision experiments is the study of the strongly interacting matter in condition of high density and temperature. In theoretical physics, quantum chromodynamics (QCD) [1] is the theory of the strong interaction, a fundamental force describing the interactions of the quarks and gluons making up hadrons. QCD is a an example of gauge theory, i.e. a quantum field theory that has a local symmetry described by a symmetry (gauge) group. In particular it is the SU(3) gauge symmetric part of the Standard Model of particle physics. QCD enjoys two peculiar properties:

- asymptotic freedom: at high energy or very short distance ($Q^2 \gg \Lambda^2$), quarks and gluons interact weakly

$$\alpha_s(Q^2) \simeq \frac{12\pi}{(33 - 2n_{flavour}) \ln \frac{Q^2}{\Lambda^2}} \tag{1.1}$$

  in $Q^2 >> \Lambda^2$, where $\Lambda \approx 200$ MeV;

- confinement: the interaction of quarks and gluons becomes stronger at large

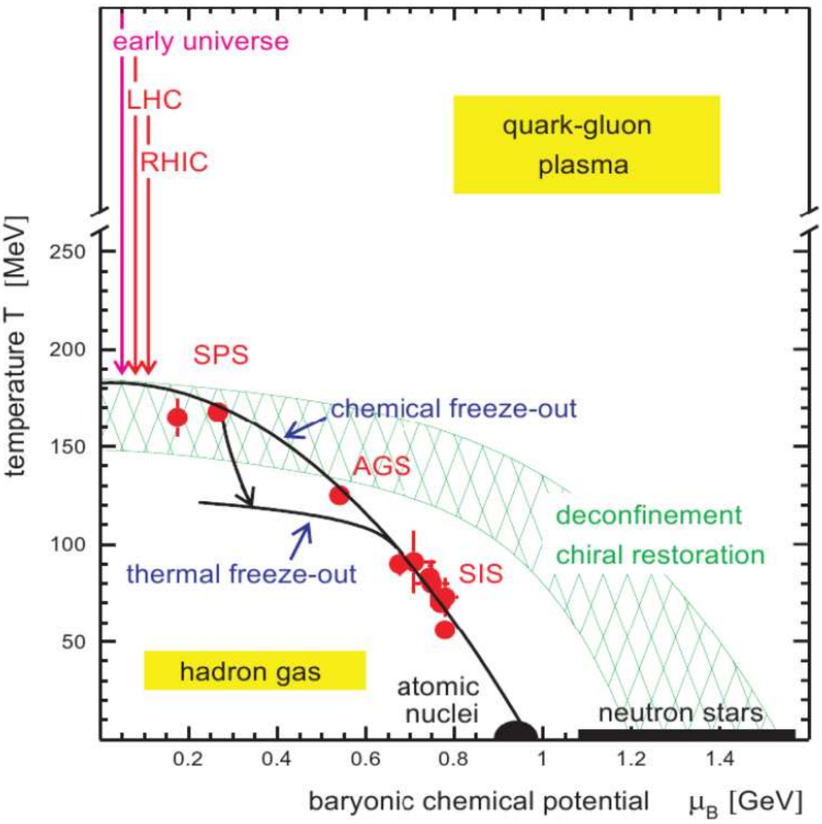

Figure 1.1: *QCD phase diagram in the (T, μ_B) plane. The green area indicates the expected phase transition region within its present uncertainty. Transitions provided by various heavy ion experiment are indicated.*

distance or low energy, which means that they cannot be separated (typical scale: 1 fm or 200 MeV) as the potential energy between the quarks increases with the distance

$$V(r) = -\frac{A(r)}{r} + Kr \tag{1.2}$$

where K ≈ 1 GeV/fm. Once the energy is above the threshold for $q\bar{q}$-pair production, such a pair is created and rapidly forms colour singlet bound states (hadrons). This prediction of QCD was first discovered in the early 1970s by David Politzer and by Frank Wilczek and David Gross. For this work they were awarded the 2004 Nobel Prize in Physics.

At high temperature T or high baryochemical potential μ_B [1] a phase transition is predicted to a state where quarks and gluons are not confined: the quark-gluon plasma [9, 10, 11, 3, 4]. The existence of the QGP state is of interest in cosmological and astrophysical research topics. It is expected that the QGP was the state of matter in the first instants of the Universe after the Big-Bang (Fig.1.2). The plasma of quark and gluons at low temperature with high baryon density could be present in the core of the neutron stars.

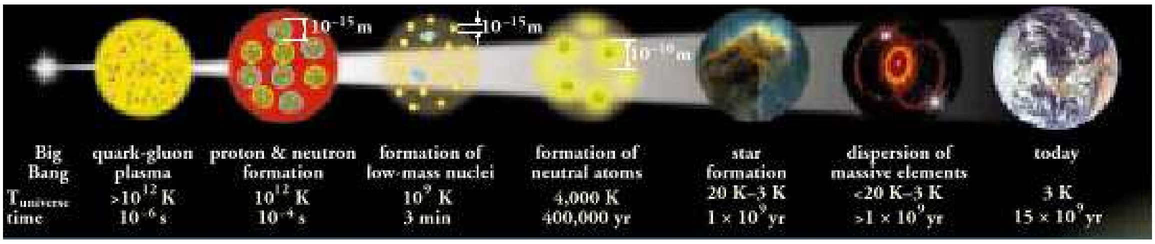

Figure 1.2: *Expansion od the Universe.*

The phase transition can be approached in two ways: compressing cold nuclear matter beyond the critical density or heating hadronic matter. In the relativistic

[1]The baryonic chemical potential μ_B of a system is defined as the change in energy E of the system when the total baryonic number N_B is increased by one unit: $\mu_B = \partial E/\partial N_B$.

thermodynamics, heating hadronic matter leads to particle production and thus also increases density. As a result, strongly interacting matter has a T - μ_B phase diagram as shown in Fig.1.1. As temperature increases, the coupling between quarks become weak, leading to deconfinement of the quarks and chiral symmetry restoration (the quark appear as nearly massles particles compared to having masses of the order of more than 100 MeV when they are confined inside hadrons). This means that the long-range interactions are screened and quarks and gluons are only subject to short-range interactions. The coupling constant at short distances is small, thus leading to only weak coupling between the quarks and gluons. Since the QCD interaction is typically strong, perturbative approximations fail. To overcome this problem, it has been introduced of a non-perturbative approximation based on discretizing four-dimension space-time onto a lattice of points, giving a theory called *lattice QCD*. Recent lattice QCD calculations predict the phase transition to the QGP for $\mu_B = 0$ at approximately 170 MeV [2].

In the laboratory, such phase transition is produced via ultra-relativistic heavy-ion collisions, where one expects to reach energy densities which exceed the critical value, thus making possible the transition to a deconfined state. The geometry of the collision plays an important role. It depends from the b, the impact parameter, that measures the distance between the centre of the colliding two nuclei. We denote as partecipants, the nucleons that primary suffer at least one collision with a nucleon of the other nucleus, and spectators, the nucleons that proceed with little perturbation along the original direction. Hence, we distinguish between central and peripheral collisions.

The space-time evolution of high energy ion-ion central collisions is now considered. It cannot be explained by a simple superposition of individual nucleon-nucleon interaction. The re-scattering of partons and secondary particles changes the particles production and eventually leads to a local thermal equilibrium. In the

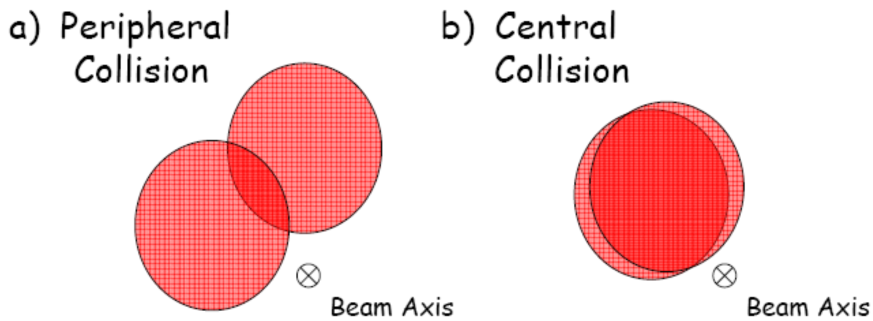

Figure 1.3: *Schematic representation of two possible collisions geometries:* ***a)****Peripheral ,* ***b)****Central.*

center-of-mass frame of the relativistic heavy ion collision, the colliding nuclei appear as two disc as they fly towards each other (see Fig.1.3).

The space-time evolution can be summarized in three main phases listed below [12]:

- Thermalization: the pre-equilibrium stage is the first phase in the collision, where the energy carried by the nuclei is released. High energy partons start escaping and direct photons are produced. At same time, the remaining nucleons scatter several times and the system reaches very high temperatures. Within 1 fm/c[4] the energy density and the temperature should become higher than the threshold values for deconfinement and the quarks and gluons can interact in a bigger volume: after the system has thermalized the Quark Gluon Plasma should be formed. In this phase the degrees of freedom are just quarks and gluons no more confined inside the nuclei. The time duration of the QGP-phase should be of the order of a few fm/c.

- Expansion: After the thermalization, the system starts expanding in the vacuum, then it cools down and the system goes through a hadron gas phase. When it reaches the typical energy density of about 1 GeV/fm^3 the partons rearrange themselves into hadrons that can still interact (the system in fact continues expanding and inelastic and elastic scattering occur between the particles). The hadron abundances are formed at the chemical freeze out time. The yields of various species are fixed even if they will be perturbed by the hadronic phase.

- Decoupling: after the hadron formation, particles continue to interact until no more interactions occur due to the system expansion. The time of the hadron decoupling is named kinetic freeze out time. Such a decoupling should happen about 15 fm/c after the beginning of the collision. This can be considered as a rough estimate of the time duration of the collision.

The evolution of the high-energy nucleus-nucleus collision is usually pictured as in Fig.1.4.

Since a hypothetical QGP, if created in heavy-ion collisions, will have an extremely short life time before hadronization occurs, its presence and characteristics can only be determined using indirect observables. A variety of signature has been proposed, although experimental measurements are complicated, due to the time/space evolution of the system and final state hadronic interactions. The probes can be divided into three groups: hadron radiation, electromagnetic radiation and hard probes.

- The first group provides an information about the hadronization stage of the plasma and allows the thermodynamical state at the stage when hadrons cease to interact and decouple to be determined. Enhanced production of strange particles [5] was predicted to be a signature of the QGP formation. In addition, collective features (e.g. flow) of the hadron emission also gives information on the pre-hadronic stage: the QGP seems to behave as a nearly ideal fluid while expanding.

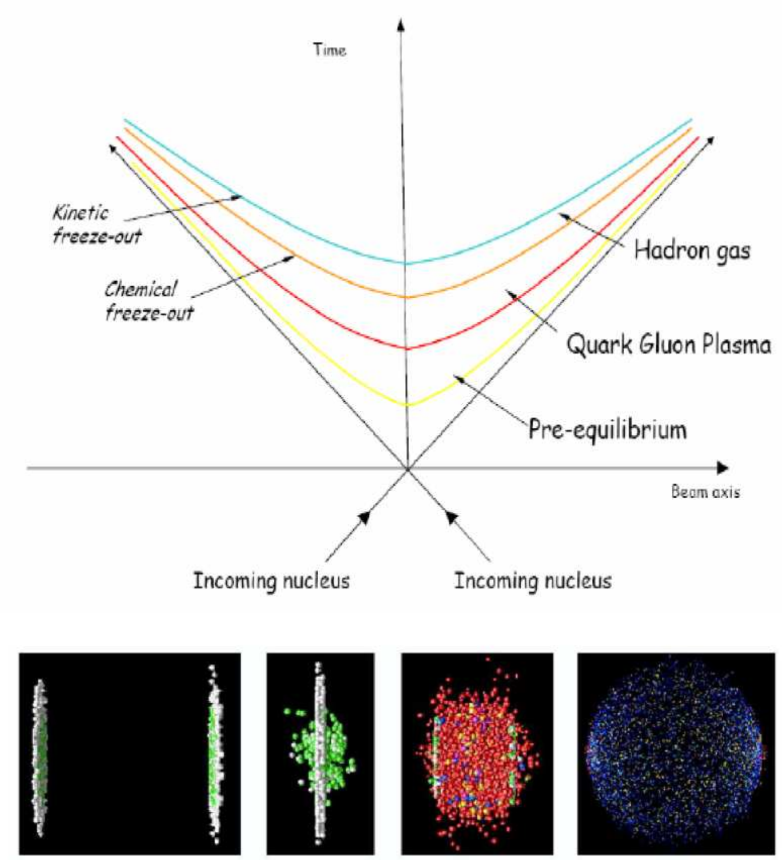

Figure 1.4: *Schematic picture of the time evolution of a central relativistic heavy ion collision.*

- The electromagnetic radiation. Electromagnetic processes involving quarks and gluons at thermal equilibrium are expected even in the transient plasma. These processes should lead to emission of photons and leptons pair. The background of photons and leptons from post-hadronization decays represent the main problem.

- Hard probes are mainly heavy quarks and quarkonia, jets and hard photons. They are produced early in the interaction before thermalization of the medium, calculable in pQCD and comparable to production in pp and in pA interactions. In particular, charmonium states (J/Ψ, Ψ', X_c) are predicted to be suppressed [6] when compared to pp reference measurement. These states are produced at the early stage of the collision, before the plasma is formed. They interact with the medium and may be dissociated since their binding energy is comparable to the mean energy of the plasma. They dissolve sequentially in the plasma at different temperatures: the more loosely bound the state, the lower the dissociation temperature. Jet suppression (quenching) is also expected. Parton radiative energy loss through multiple gluon radiation of the produced hard parton is induced by the dense QCD medium: energy loss is flavour dependent and is determined by the density of the medium, increasing with the temperature.

1.1.1 ALICE physics performance

A theoretical overview of some of the observables and probes that ALICE are listed below.

Charged-particle multiplicity: The charged-particle multiplicity and in particular the average number of charged particles, on the theoretical side, fixes a global property of the medium produced in the collision. It is related to the energy density

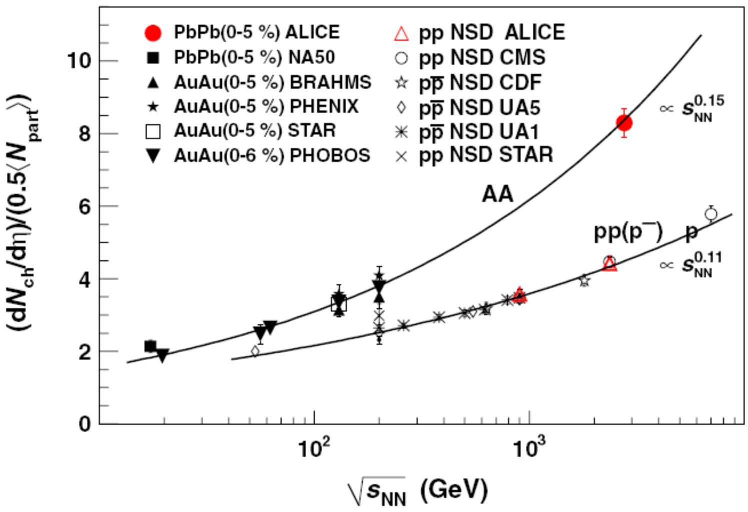

Figure 1.5: *Charged-particle pseudorapidity density per partecipant pair for central nucleus-nucleus and pp ($p\bar{p}$) collisions as a function of* $\sqrt{s_{NN}}$.

reached in the collision and features in the calculation of many other observables. On the experimental side, the charged-particle multiplicity per unit of rapidity (see Appendix A) largely determines the accuracy with which many observables can be measured. This variable is not derivable in any way from the QCD lagrangian since it is dominated by soft non-perturbative QCD and the relevant processes must be modelled using the new, large-scale, $R_A \approx A^{1/3}$ fm.

ALICE measured the charged-particle multiplicity density at midrapidity (see Appendix A) in PbPb collisions at a center-of-mass energy per nucleon pair $\sqrt{s_{NN}}$ = 2.76 TeV. For an event sample corresponding to the most central 5 % of the hadronic cross section, the pseudorapidity density of primary charged particles at midrapidity is 1584 $\pm$ 4 (stat) $\pm$ 76 (syst), which corresponds to 8.3 $\pm$ 0.4 (syst) per participating nucleon pair. This results represents an increase of about 1.9 relative to pp collisions at similar collision energies, and about a factor 2.2 to central Au-Au collisions at $\sqrt{s_{NN}}$ = 0.2 TeV. In Fig.1.5 this value is compared to the measurements for Au-Au and Pb-Pb and pp and $p\bar{p}$ collisions over a wide range of collision energies.

Particle production: The bulk of the particles emitted in a heavy-ion collision consists of soft hadrons, which decouple from the collision region in the late hadronic freeze-out stage of the evolution. They provide information on the freeze-out temperature and chemical potential. In addition, parameters characterizing the freeze-out distributions constrain the dynamical evolution and thus provide indirect information about the early stage of the collision. Theoretical arguments also show that different aspects of the measured final hadronic momentum distributions are determined at different times. By combining the information from different PID detectors of the ALICE apparatus, stable charged hadrons (pions, kaons, and protons) can be identified and measured from very low momentum (hundreds of MeV) up to at least 50 GeV. Secondary vertices are used to identify charged and neutral kaons as well as hyperons up to, and beyond 10 GeV. Baryon production is measured in the central region (p, $\bar{p}$, Λ, $\bar{\Lambda}$, Ξ^+, Ξ^-, Ω^-, and Ω^+) to study the baryon number transfer in rapidity both in PbPb and pp collisions. Resonances bring additional information about the final stages of the collision: $\rho(770)^0$, $K^*(892)^0$, and the $\phi(1020)$ are investigated. Also, ALICE is able to measure to some extent variations in the resonance parameters (mass, width, line shape), which may arise from the restoration of chiral symmetry. Recent results from ALICE experiment will be described in the last section of this chapter.

Jets: Jets are clusters of hadrons and they are defined with dedicated algorithms. They are formed by a hard parton produced in the hadronic collision that further produces a shower of hadrons. The definition of a jet strongly depends on the algorithm used and the background of the underlying event: this is produced in the soft scattering of the incoming hadrons, and is quite large in particular for heavy-ion collisions, making the reconstruction a challenge for all experiments and requiring the development of proper techniques for its subtraction.

At the LHC, high rates are for the first time expected for energies at which jets can be fully reconstructed against the high background from the underlying nucleus–nucleus event. Jet study will have much higher sensitivity to the medium properties with respect to the nuclear modification factor R_{AA} [2] [13]. Jets in p-p interaction are fairly well understood and described by Monte Carlo models based on perturbative QCD in a wide kinematical range. In A-A interactions, fragmentation is strongly modified by the medium at $p_t \approx$ 1-5 GeV/c even for the highest energy jets. High-p_t partons mainly lose energy through a radiative effect called gluon rescattering. Recent studies concluded that this loss grows quadratically with the in-medium path length, thus being very sensitive to the geometry of the collision region. The same parameter determines the p_t broadening and energy loss of jets. This leads to a jet quenching effect, that sensitively depends on the scattering properties of the medium.

Direct photons: Studies in p-p collisions are still necessary, even though direct photon production has been studied for years: there is indeed no agreement between theory and experimental results. In A-A collisions prompt photons from the colliding hadron can probe the medium at the time of their production as they do not interact with the medium afterwards. However, several contributions to the photon production add to the initial production in different temporal stages of the collision (e.g. background from $\pi^0 \rightarrow \gamma\gamma$ which can be, of course, subtracted). Thermal photons are produced in the plasma till the freeze-out. These thermal effects can be disentangled from QCD effects (p-p interactions) and nuclear effects (p-A interactions): in p-p interactions there are no thermal effects, in p-A interactions there are only nuclear

[2] This quantity is defined as the ratio between particle yield in nucleus–nucleus collisions, normalized to the number of binary collisions given by the Glauber model calculation, to the corresponding yield in p-p collisions:

$$R_{AA}(p_T) = \frac{(1/N_{evt}^{AA})d^2N_{ch}^{AA}/d\eta dp_T}{\langle N_{coll}\rangle(1/N_{evt}^{pp})d^2N_{ch}^{pp}/d\eta dp_T} \quad (1.3)$$

If there is no medium effect, the yield should scale with the number of binary collisions and the ratio is 1.

effects and no thermal effects while in nucleus–nucleus collisions both nuclear and thermal effects are present.

Dileptons: Lepton pairs are produced throughout the evolution of the system: these come from prompt production in nucleon–nucleon collisions, thermal radiation from the QGP and hot hadronic phase and final state meson decays after freeze-out. Each of these contributions will dominate the continuum in the dilepton mass range in different regions. Since leptons and dileptons, once produced, are not affected by later stages of the collision, their production is an important tool for measuring the temperature and the dynamical evolution of the system.

Heavy-quark and quarkonium production: Heavy quarks (charm and bottom) provide sensitive probes of the collision dynamics both at short and long timescales: their production takes place on the timescale of $1/\mathrm{m}_Q$, where m_Q is the mass of the quark, and their lifetimes are long enough to let them go through the thermalization phase of the plasma so that they can probe its presence. Production of heavy-quark pairs can also take place: these pairs can form quarkonium states that can very likely dissolve since their binding energy is comparable to the mean energy of the plasma (color screening of the $c\overline{c}$ potential by the surrounding color charges). As a result, open heavy flavours emerge in the final state. Therefore quarkonium states should be suppressed and open heavy flavour enhanced. However, at high p_t open heavy flavours are expected to be suppressed due to the parton energy loss through the medium. To extract information about the QGP phase from the features of heavy-quark and quarkonium production, a deep understanding of p-p and p-A collision is mandatory. In particular the measurement of the total cross-sections both in p-p and A-A is necessary, as no measurements were possible at Tevatron the theoretical uncertainties on them are great. The typical variables to be studied are the total production rates, transverse momentum distributions and kinematical correlations between the quark and the antiquark.

1.2 Proton–proton physics with ALICE

Proton–proton data at a centre-of-mass energy up to 14 TeV represents both

- a good benchmark for the understanding of heavy-ion data:
  - Particle multiplicities: difference in the multepleplicity p-p/ Pb-Pb are due to the different parton distributions in the nucleon and in the nuclei;
  - Jet fragmentation functions;
  - Slopes of transverse-mass distribution;
  - Particles yields and ratios;
  - Ratios of momentum spectra;
  - Strangeness enhancement: the strangeness enhancement observed in heavy ion collisions between 2 and 10 GeV can be compared with the very regular behaviour in pp collisions;
  - Heavy-quark and quarkonium production cross section: possible suppressions or enhancement can be estimated and compared with p-p collisions;
  - Dilepton spectra;
  - Photon spectra;
- to explore p-p physics in a new energy domain (genuine pp physics in ALICE):
  - Charged-particle spectra: charged-particle spectra, inclusive and for identified species, will be measured in rapidity and transverse momentum. Correlations between mean p_t and multiplicity are of great interest, for example for each particle specie, since at Tevatron different correlations were found;

- Baryon-number transfer in rapidity: the mechanism by which the baryon number is transported to the central rapidity region in hadronic collisions is an open question: there are models explaining the transfer with different mechanisms (quark–diquark string breaking) and estimates. ALICE will measure with abundant statistic baryons in several channels in the central-rapidity region to clarify this issue. The baryon-number asymmetry will be studied for identified baryons (protons, Λs, Ξs and Ωs) at low p_t and as a function of particle multiplicity.

- Two-particle correlations: in particular, studying two-particle correlations will allow the energy dependence and the dependence on particle type of the two-particle pseudorapidity correlations to be determined.

- Heavy-flavour production: measuring heavy-quark production cross sections will help in understanding discrepancies found between theoretical predictions and measurements at SPS, Tevatron, HERA and LEP. The measurements will be extended to very low p_t, improving the precision with respect to existing results.

- Jets: in pp collisions the main interest is in characterizing events with several jets at relatively low p_t. ALICE will be also able to study jet fragmentation as it can measure and identify particles in a highly dense environment, this being crucial for the reconstruction of jet topology.

- Diffractive physics: ALICE should be able to observe large rapidity gaps, due to its wide coverage in central and forward pseudorapidity, as well as for low-x phenomena (down to 10^{-6}). Diffractive processes will have a sizeable effect since single and double-diffractive dissociation cross-sections are predicted to increase at the LHC. Investigation of the hadronic structure of the final state produced in diffractive processes can provide, as well as particle identification, important information on the mechanism of high-energy hadronic interactions.

– Double-parton collisions: increasing the energy of p-p collisions, multi-parton collisions become increasingly important since the parton flux increases. Such a measurement has already been performed at the Tevatron showing that the structure of the proton is much richer than the independent superposition of single-parton distribution functions accessible by deep-inelastic scattering. At the LHC a significant cross-section is estimated for double-parton collisions into final states with four jets and three jets and one photon.

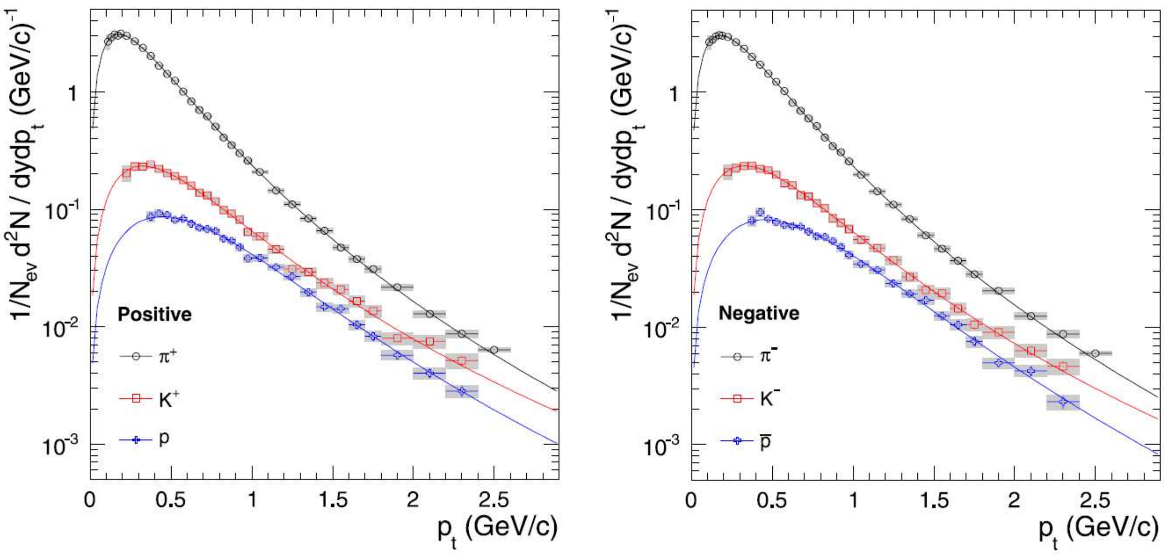

Figure 1.6: *Transverse momentum spectra of positive (left) and negative (right) hadrons from pp collisions at* $\sqrt{s}$ = *900 GeV. Grey bands: total* p_t*-dependent error (systematic plus statistical); normalization systematic error (3.6% not shown). The curves represent fits using a Lévy function.*

1.3 Results from ALICE experiment: spectra and ratios

The partonic matter created in the ultrarelativistic collisions of heavy ions hadronizes into a large number of hadronic species. The yields, momentum distributions and correlations of these particles can give information on the hadronisation process and also on characteristics of the matter created in the initial partonic state. It is possible to divide the particles emerging from the system into two wide categories: those particles hadronizing out of a system which is essentially in chemical equilibrium, called the *soft part*, with $p_t <$ 1-2 GeV/c, and those coming from hard partonic interactions, called the *hard part*, with $p_t >$ 5 - 6 GeV/c. The soft particles usually exhibit a thermal spectrum and the dN/dp_t distributions follow a Boltzmann exponential behaviour which does not depend on the centre-of-mass energy:

$$\frac{d^2N}{dydp_t} = Ap_te^{\frac{-m_t}{T}} \tag{1.4}$$

At high p_t the spectra follow a power law:

$$\frac{d^2N}{dydp_t} = Bp_t(1 + \frac{p_t}{p_0})^{-n} \tag{1.5}$$

The ALICE apparatus with its ability to identify particles up to high momenta allows us to obtain detailed information on particle momentum distribution. Particles at low momenta are also measured, allowing us to extract the chemical composition.

In this section, we briefly report recent results on spectra and hadron ratio.

- **Production of pion, kaons and protons in pp collisions at $\sqrt{s}$ = 900 GeV with ALICE at the LHC [14]**

  In the pp collisions at ultra-relativistic energies the bulk of the particles produced at mid-rapidity has transverse momenta, p_t , below 1 GeV/c. This low p_t particle production must be measured providing a crucial input for the modelling of hadronic interaction and the hadronization process. It is important to study the bulk production of particle as a function of both p_t and particle species. At the LHC energies, a new energy regime is being explored where particle production from hard interactions, which are predominantly gluonic in nature, is expected to play an increasing role. ALICE measured the transverse momentum spectra and yields of identified particle at mid-rapidity in pp collisions at $\sqrt{s}$ = 900 GeV. The measurement has been performed with Inner-Tracking-System, Time-Projection-Chamber and Time-Of-Flight from p_t = 100 MeV to 2.5 GeV. In Fig.1.6 transverse momentum spectra of positive and negative hadrons are shown. The combined spectra are fitted with the Lévy function. Also the ratio π^+/π^- and K^+/K^- as a function of p_t is close to unity within the errors, allowing the combination of both spectra in the Lèvy fits.

- **Mid-rapidity anti-proton to proton ratio in pp collisions at $\sqrt{s}$ = 0.9 and 7 TeV measured by the ALICE experiment at the LHC [15]** The high precision measurement of the proton to antiproton ratio at mid-rapidity has been carried out. The LHC opens a unique possibility to investigate baryon stopping over very large rapidity gaps by measuring this ratio. The measurement has been performed using the Inner-Tracking-System, the Time-Projection-Chamber. The data used for this analysis were recorded during the first LHC pp runs at $\sqrt{s}$ = 0.9 (December 2009) and 7 TeV (March 2010). It is found to be very close to unity (Fig. 1.7), $(\bar{p}/p)_{|y|<0.5} = 0.966 \pm 0.014$(stat.) $\pm$ 0.013 (syst.) at 0.9 $(\bar{p}/p)_{|y|<0.5} = 0.999 \pm 0.006$(stat.) $\pm$ 0.013 (syst.) at 7 TeV, and independent of both rapidity and transverse momentum. The result is fully consistent with the standard picture of baryon transport and

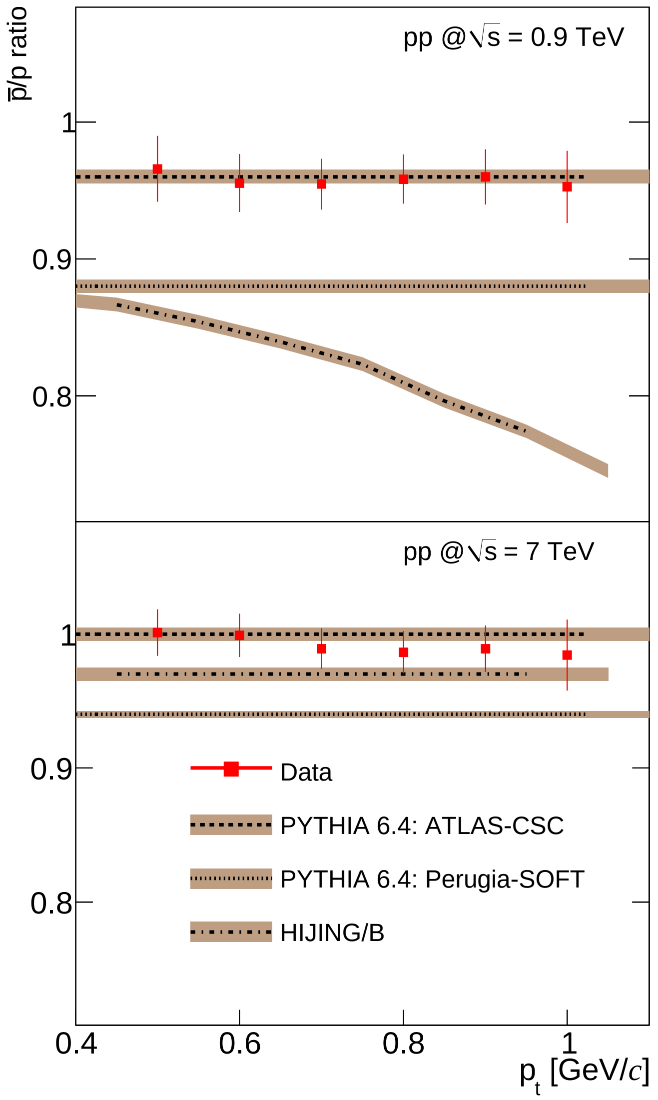

Figure 1.7: *The p_t dependence of the $\bar{p}/p$ ratio integrated over $|y| < 0.5$ for pp collisions at $\sqrt{s}$ = 0.9 TeV (top) and $\sqrt{s}$ = 7 TeV (bottom). Only statistical errors are shown for the data; the width of the Monte Carlo bands indicates in general the statistical error of the simulation results but has been omitted, for clarity, from three PHYTIA tunes at 0.9 TeV.*

sets stringent limits on any additional contributions to baryon stopping over very large rapidity gaps in pp collisions.

In Fig.1.8, central rapidity $\bar{p}/p$ ratio as a function of the rapidity interval Δy [3] (lower axis) and center-of-mass energy (upper axis) is shown. The ALICE measurement corresponds to $\Delta y = 6.87$ and $\Delta y = 8.92$ for the two energies respectively. The lower energy data correspond to both pp and heavy-ion collisions. The other points come from the ISR[4] [16] and RHIC [5] [17] experiment. At the ISR energy ($\sqrt{s} = 23, 31, 45, 53, 63$ GeV) the ratio rises from 0.3 to 0.8 for pp and central AuAu collisions at RHIC energy ($\sqrt{s} = 200$ GeV). At this lower energies, the ratio differs significantly from 1 indicating that a substantial fraction of the baryon number associated with the beam particles is transported towards mid-rapidity. The excess (slightly) of protons found in nuclear collisions compared to pp reactions at the same energy has contributed to the development of models with enhanced baryon stopping mechanism like HIJING/$B\bar{B}$.

- **Preliminary transverse momentum spectra of charged hadrons with the ALICE detector in Pb-Pb at $\sqrt{s} = 2.76$ TeV [22]** The transverse momenta spectra of pion, kaon and proton are measured from 100 MeV/c up to 3 GeV/c for pions, from 200 MeV/c up to 2 GeV/c for kaons and from 300 MeV/c up to 3 GeV/c for protons and antiprotons using the dE/dx and time-of-flight identification technique. In Fig.1.9 (upper panel) the transverse momentum spectra of primary protons and corresponding fits in several centrality classes (the centrality depends on the impact parameter). Individual fits to the data are performed following a blast-wave parametrization [23] to extrapolate the spectra

[3] For more details see Appendix A
[4] Intersecting Storage Rings.
[5] Relativistic Heavy Ion Collider. Four detectors: STAR [18], PHENIX [19], PHOBOS [20] and BRAHMS [21].

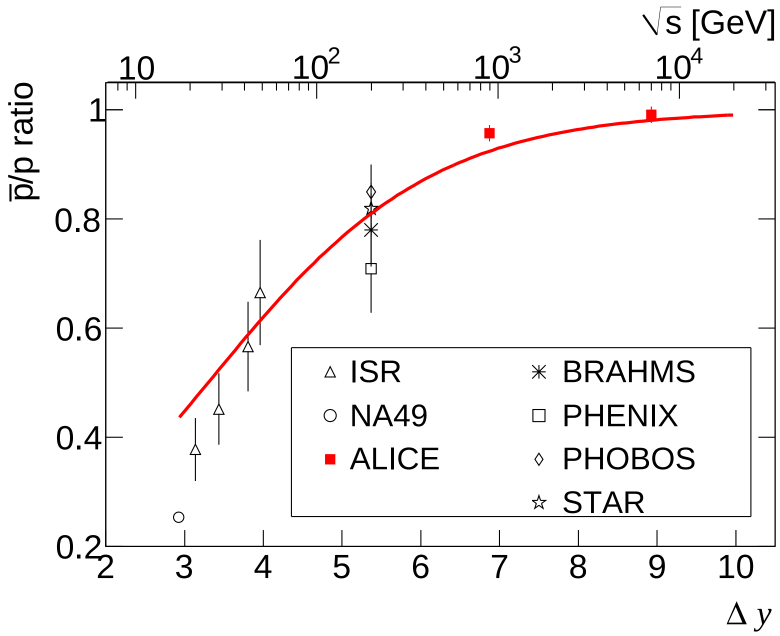

Figure 1.8: *Central rapidity* $\bar{p}/p$ *ratio as a function of the rapidity interval* Δy *(lower axis) and center-of-mass energy (upper axis). Error bars correspond to the quadratic sum of statistical and systematic uncertainties for the RHIC and LHC measurements and to statistical errors otherwise.*

outside the measured p_t range. Antiparticle/particle integrated production ratios are observed to be consistent with unity for all particles species in all centralities suggesting that the baryochemical potential is close to zero as expected at LHC energies. In Fig.1.9 (lower panel) the comparison between the ALICE results with RHIC data in Au - Au collisions at $\sqrt{s} = 200$ GeV for the 0-5% most central collisions (see [24, 25, 26, 27, 28, 29, 30, 31, 32, 33, 34]).

- **Recent results in pp collisions at $\sqrt{s}$ = 7 TeV** The analysis for the measurement of pion, kaon and proton spectra in pp collisions at $\sqrt{s} = 7$ TeV is on going [35, 36]. In Fig.1.10 preliminary pion, kaon and proton spectra for positive and negative are shown. The Lévy fit to spectra has

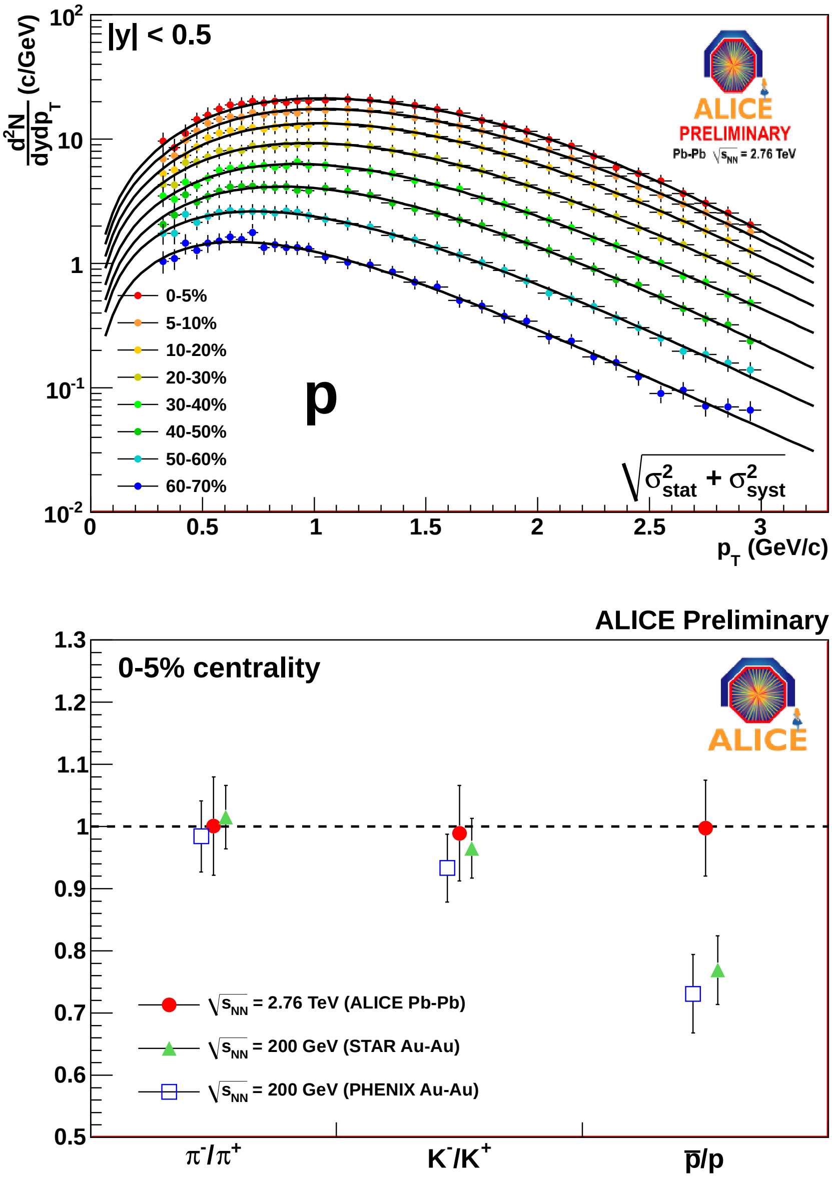

Figure 1.9: *Upper panel: transverse momentum spectra of primary protons and corresponding fits in several centrality classes (Pb-Pb at 2.76 TeV). Lower panel: antiparticle/particle production ratios in the 0-5% most central collisions (Pb-Pb at 2.76 TeV).*

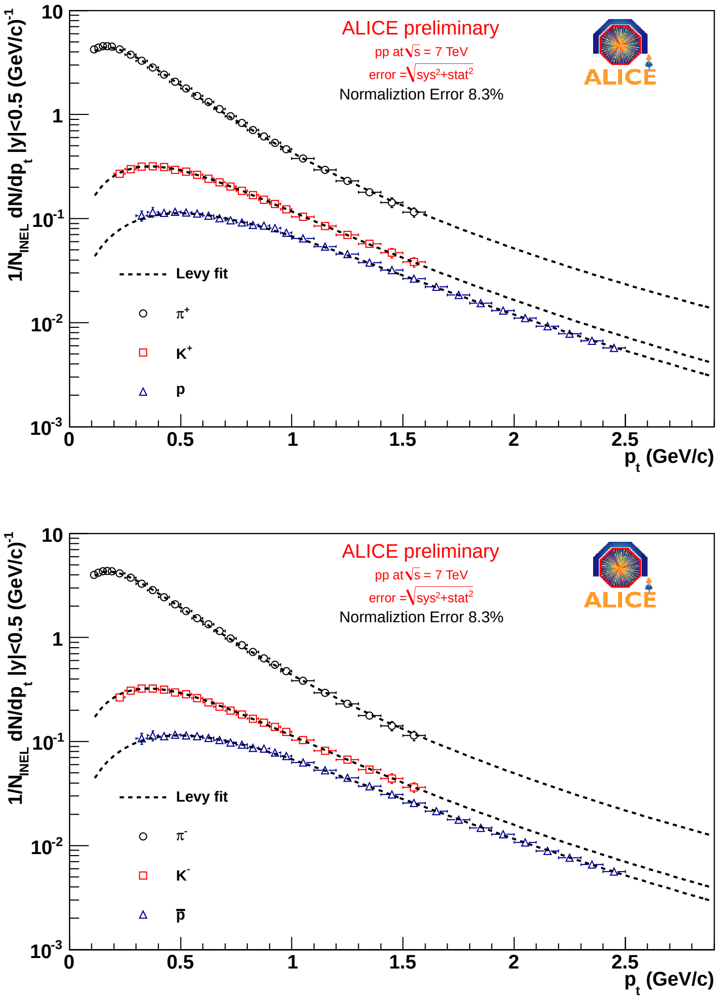

Figure 1.10: *Preliminary pion, kaon and proton spectra of negative and positive particles in pp collisions at* $\sqrt{s}$ = *7 TeV. The fully corrected spectra are normalized to the inelastic collisions. Statistical and systematic errors are added.*

been performed. These spectra are measured using the dE/dx and time-of-flight particle-identification technique. The determination of the yield of charged kaons identified by their weak decays (kink topology) inside the Time-Projection-Chamber detector is also, performed. The HMPID detector gives his contribute on this item measuring momentum transverse spectra from 1.5 GeV/c up to 3.4 GeV/c for pions and kaons, and from 1.5 GeV/c up to 6 GeV/c for protons and antiprotons using the Cherenkov radiation technique as will be shown in this thesis.

Chapter 2

The ALICE experiment and the High Momentum Particle IDentification detector

2.1 Introduction: LHC

The Large Hadron Collider (LHC) [37, 38, 39], is the biggest and most powerful particle accelerator in the world. It is a two-ring-superconducting-hadron accelerator and collider installed in the existing 26.7 km tunnel that was constructed between 1984 and 1989 for the CERN LEP machine. The LEP tunnel lies between 45 m and 170 m below the surface on a plane inclined at 1.4% sloping towards the Léman lake. The approval of the LHC project was given by the CERN Council in December 1994. At that time, the plan was to build a machine in two stages starting with a center-of-mass energy of 10 TeV, to be upgraded later to 14 TeV. However, in December 1996 the CERN Council approved construction of the 14 TeV machine in a single stage.

The LHC is designed to collide two counter-rotating beams of protons or heavy

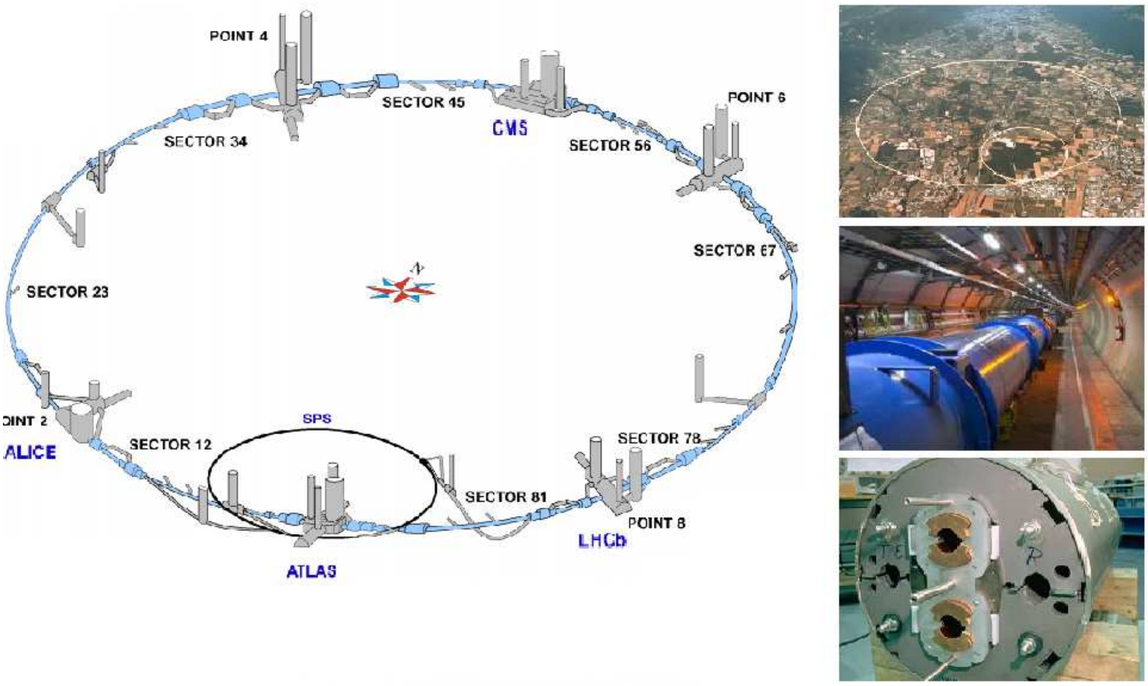

Figure 2.1: *Overview schematic of the LHC and some related picture;*

ions and is currently accelerating lead beams (November 2011). The aim is to reveal the physics beyond the Standard Model with centre of mass collision energies of up to 14 TeV. The number of events per second generated in the LHC collisions is given by:

$$N_{event} = L\sigma_{event} \tag{2.1}$$

where σ_{event} is the cross section for the event under study and L the machine luminosity. The machine luminosity depends only on the beam parameters and can be written for a Gaussian beam distribution as:

$$L = \frac{N_b^2 n_b f_{rev} \gamma_r}{4\pi\epsilon_n \beta*} F \tag{2.2}$$

where N_b is the number of particles per bunch, n_b the number of bunches per beam, f_{rev} the revolution frequency, γ_r the relativistic gamma factor, ϵ_n the normalized

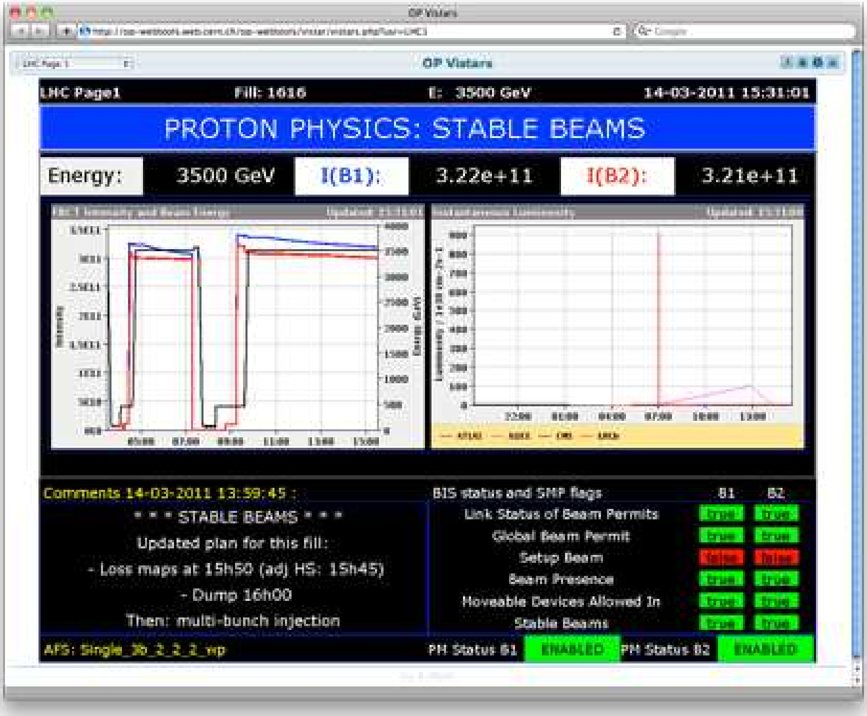

Figure 2.2: *A screen shot of LHC Page, which displays the status of the accelerator, showing stable beams in the LHC [40].*

transverse beam emittance, $\beta*$ the beta function at the collision point, and F the geometric luminosity reduction factor due to the crossing angle at the interaction point (IP):

$$F = (1 + (\frac{\theta_c \sigma_z}{2\sigma*})^2)^{-1/2} \tag{2.3}$$

θ_c is the full crossing angle at the IP, σ_z the RMS bunch length, and $\sigma*$ the transverse RMS beam size at the IP. The above expression assumes round beams, with $\sigma_z << \beta$, and with equal beam parameters for both beams. The exploration of rare events in the LHC collisions therefore requires both high beam energies and high beam intensities.

The LHC has two high luminosity experiments, ATLAS [41] and CMS [42], both aiming at a peak luminosity of L = 10^{34} cm^2 s for proton operation and two low luminosity experiments, LHCB for B-physics, L = 10^{32} cm^2, and TOTEM [45] for the detection of protons from elastic scattering at small angles, aiming at a peak luminosity of L = 10^{29} cm^2 with 156 bunches. In addition to the proton beams, the LHC will also be operated with ion beams. The LHC has one dedicated ion experiment, ALICE , aiming at a peak luminosity of L = 10^{27} cm^2 for nominal lead-lead ion operation.

The serious technological challenge in the LHC are the superconducting (1.9 K) dipoles which bend the beams around the 27 km circumference of the LHC. At 7 TeV these magnets have to produce a field of around 8.4 Tesla at a current of around 11,700 A. The magnets have two apertures, one for each of the counter-rotating beams. Each dipole is 14.3 meters long, for a total number of 1232. The magnets are superconducting and are cooled by a complex cryogenics system. The cables conduct current without resistance in their superconducting state.

The seven experiments approved for data taking at LHC are: ATLAS (A Toroidal LHC ApparatuS), CMS (Compact Muon Solenoid), LHCb [43] (Large Hadron Collider beauty experiment), ALICE (A Large Ion Collider Experiment), TOTEM (Total Cross Section, Elastic Scattering and Diffraction Dissociation), LHCf [44] (LHC forward) and MoEDAL [46] (the Monopole and Exotics Detector At the LHC).

2.2 The ALICE detector

ALICE is a general purpose, heavy-ion detector at the CERN devoted to study the physics of nucleus nucleus interaction at LHC energies. It allows a comprehensive study of hadrons, electron, muon, and photons produced in the collisions. ALICE, in fact, has great capability to identify particles in a broad momentum range, from very low ($\approx$ $100MeV/c$) to high ($\approx$ $100GeV/c$) transverse momentum, with high-momentum resolution in an environment with large multiplicity. The ALICE p-p physics, at same time, plays a relevant role providing the reference to understand the

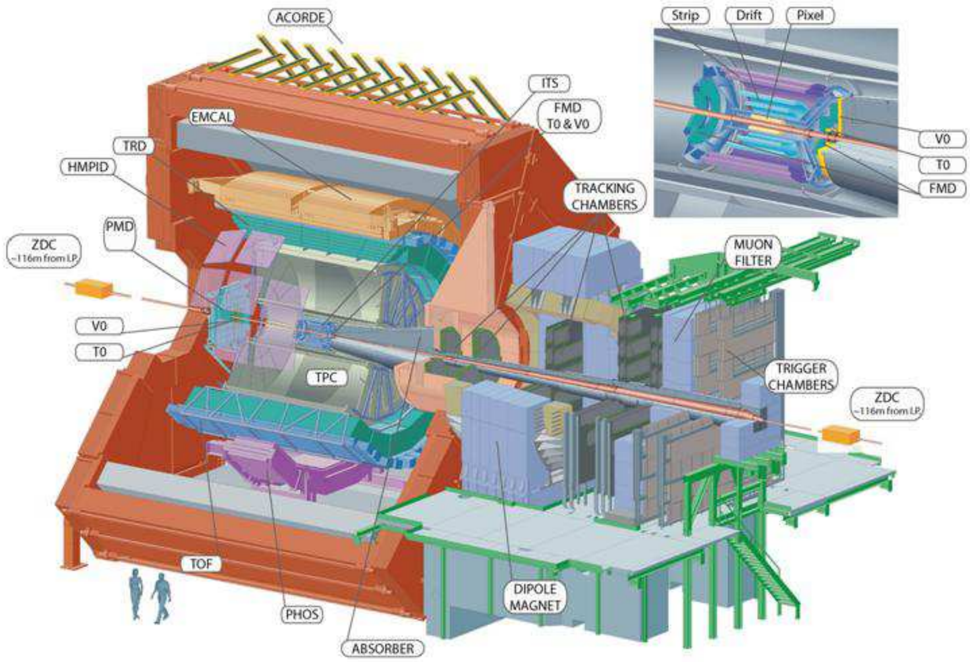

Figure 2.3: *ALICE detector layout: the central system detectors, the L3 magnet and the muon spectrometer. The HMPID is not shown in its actual position (2 o'clock) for sake of visibility.*

heavy-ion data and to carry out specific p-p studies. The ALICE experiment was approved in 1997 and it's built by a collaboration including over 1000 physicists and engineers from 105 Institutes in 30 countries. Its overall dimension are $16\times16\times26$ m^3 with a total weight of 10000t. The detector and area facilities are located at Point 2 of the LHC accelerator tunnel in the commune of St. Genis-Pouilly, France. An brief overview of the ALICE detector introducing the various sub-detectors will be present in this chapter.

The general layout of the experiment is shown in Fig.2.3. The detector is composed of 18 sub-detectors and their associated systems for power supply, cooling, gas, detector control, detector safety, trigger and data acquisition. The central part of ALICE is enclosed in the L3 solenoid, which has an internal length of 12.1 m and a radius of 5.75 m. The ITS, TPC, TRD and TOF detectors are supported inside the L3 solenoid magnet by the so-called space-frame. The space-frame is a cylindrical, 7 m long and 8.5 m diameter stainless steel construction. This structure rests on two 12 m long rails, which span the length of the solenoid magnet. There is a second pair of rails for the PHOS detector and a third pair for the EMCal detector. The HMPID is mounted on a cradle, which is attached to the space-frame. The experiment includes a solenoid magnet previously used in the L3 experiment of LEP which houses the central detectors and a dipole magnet situated next to the solenoid which is part of the forward muon spectrometer. From the inside out, the barrel contains an Inner Tracking System (ITS) of six planes of high-resolution silicon pixel (SPD), drift (SDD), and strip (SSD) detectors, a cylindrical Time-Projection Chamber (TPC), three particle identification arrays of Time-of-Flight (TOF), Ring Imaging Cherenkov (HMPID) and Transition Radiation (TRD) detectors, and two electromagnetic calorimeters (PHOS and EMCal). All detectors except HMPID, PHOS, and EMCal cover the full azimuth. The forward muon arm consists of a complex arrangement of absorbers, a large dipole magnet, and fourteen planes of tracking and triggering chambers. Several smaller detectors (ZDC, PMD, FMD, T0, V0) for global event characterization and triggering are located at small angles. An array of scintillators (ACORDE) on top of the L3 magnet is used to trigger on cosmic rays. ALICE will concentrate on physics at or close to mid-rapidity where the lowest baryon density and the maximum energy density is reached. Therefore detectors are mainly concentrated around mid-rapidity, covering about two units in rapidity, while 1.5 units of rapidity at small angles with respect to the beam line is the coverage of the muon spectrometer. For details on the ALICE coordinate system see Appendix B.

2.2.1 The Central barrel

2.2.1.1 Inner Tracking System (ITS)

The ITS [47] consists of six cylindrical layers of silicon detectors with radii between 3.9 cm and 43.0 cm:

- two layers of Silicon Pixel Detectors (SPD);
- two layers of Silicon Drift Detectors (SDD);
- two layers of Silicon Strip Detectors (SSD).

It covers the rapidity range of $|\eta|< 0.9$ for the vertices located within the length of the interaction diamond ($\pm$ 1 σ). Because of the high particle density and to achieve the best impact parameter resolution, pixel detector have been chosen for the inner layers. The two outer layers, where the track density is expected to be below one particle per cm^2, are equipped with double-sided Silicon micro-Strip Detectors (SSD). The four outer layers have analogue readout and therefore can be used for particle identification via dE/dx measurement in the non-relativistic ($1/\beta^2$) region. The analogue readout provides the dE/dx measurement for low momenta, highly ionizing particles, down to the lowest momentum at which tracks can still be reconstructed. This feature gives the ITS stand-alone capability as a low-pt particle spectrometer. The amount of the material in the active region has been reduced to minimize the effect of multiple scattering for particles that have a small transverse momentum. The spatial resolution is of the order of a few tens of μm with the best precision for the detectors closest to the primary vertex (12 μm). A geometrical layout of the ITS is shown in the left-hand panel of Fig. 2.4. The ALICE global reference system has the z axis on the beam-line, the x axis in the LHC (horizontal) plane, pointing to the center of the ring, and the y axis pointing upward. The axis of the ITS barrel coincides with the z axis. The tasks of the ITS are summarized in the following list:

- to contribute with the TPC to the global tracking of ALICE by improving the angle and momentum resolution;
- to reconstruct the position of the primary interaction vertex;
- to reconstruct secondary vertices from decays of heavy-flavor and strange particle decays;
- to track and identify particles with momentum below 100 MeV/c;
- to improve the momentum, impact parameter and angle resolution for the measurement of high-p_t particles performed with the TPC;
- to detect particles traversing dead regions of the TPC.

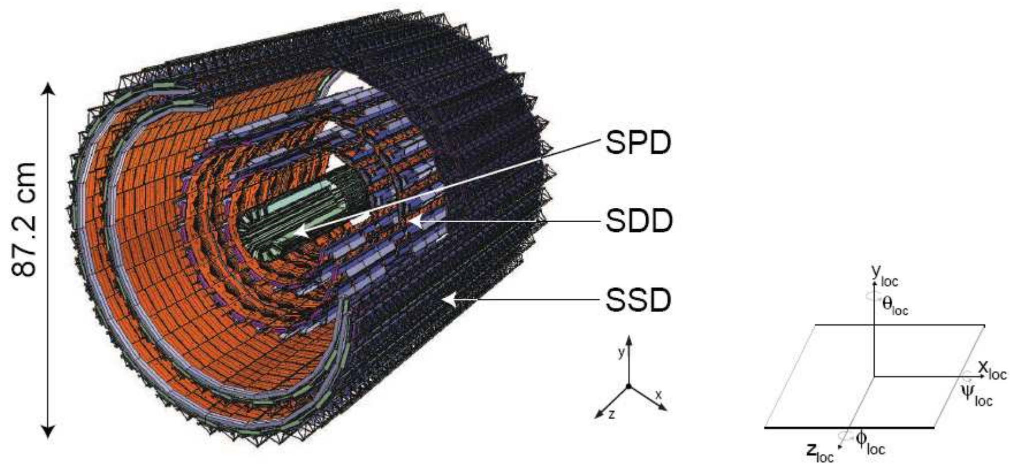

Figure 2.4: *Layout of the ITS (left) and orientation of the ALICE global (middle) and ITS-module local (right) reference systems. The global reference system has indeed its origin in the middle of the ITS, so that the z direction coincides with the beam-line.*

In the Fig. 2.5 the measured energy loss per unit length as a function of particle momentum is shown in pp collisions at $\sqrt{s}$ = 7 TeV (2010 data). Clear bands of pions, kaons and protons are shown.

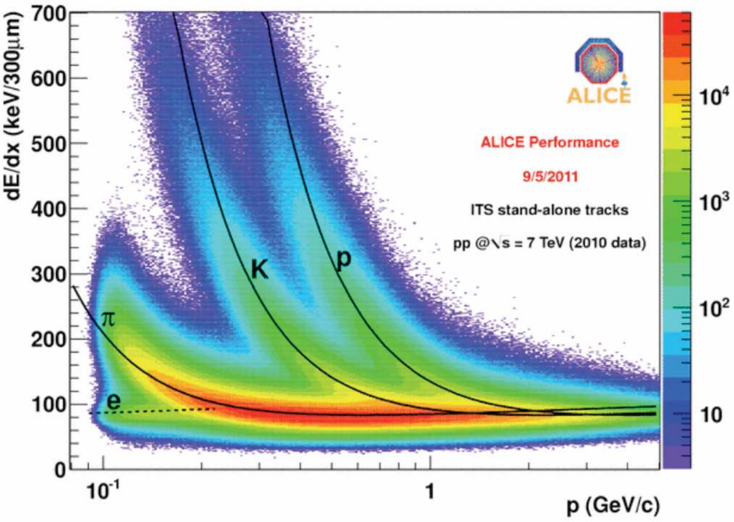

Figure 2.5: *The measured energy loss per unit length as a function of particle momentum in the ITS.*

2.2.1.2 Time Projection Chamber (TPC)

The TPC [48] is the main tracking detector of the ALICE apparatus. Together with the other central barrel detectors, the TPC provides charged particle momentum measurements with good two-track separation, particle identification, and vertex determination. It has a cylindrical shape and covers the pseudorapidity range $|\eta| < 0.9$ for tracks with full radial track length and up to $\eta = 1.5$ for reduced track length. It covers the full azimuth. The inner radius is determined by the maximum acceptable hit density and is about 85 cm, the outer radius is 250 cm and is determined by the length required to have a dE/dx resolution better than 5 - 7 %. The length along the beam direction is 500 cm. It consists of a large cylindrical field cage, filled with 90 m^3 of $Ne/CO_2/N_2$ (90/10/5), in which the primary electrons are transported over a distance of up to 2.5 m on either side of the central electrode to the end plates. Multi-wire proportional chambers with cathode pad readout are mounted into 18 trapezoidal sectors at each end plate. The field cage is operated at high voltage gradients because

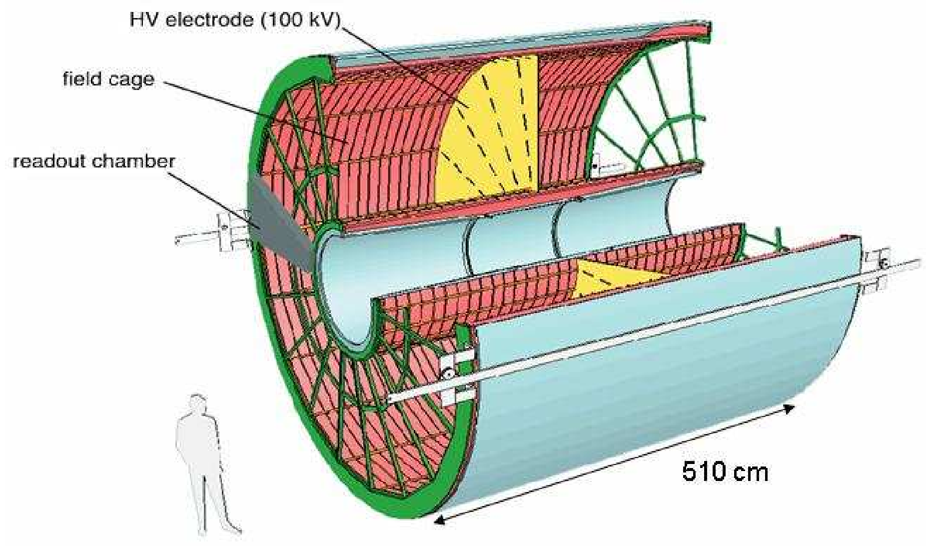

Figure 2.6: *Schematic view of the Time Projection Chamber (TPC) of ALICE. The readout chambers and the central electrode relative position and the direction of the field cage is shown. The drift time of ionization electrons produced by a particle traversing the TPC near the central electrode is about 90 μs.*

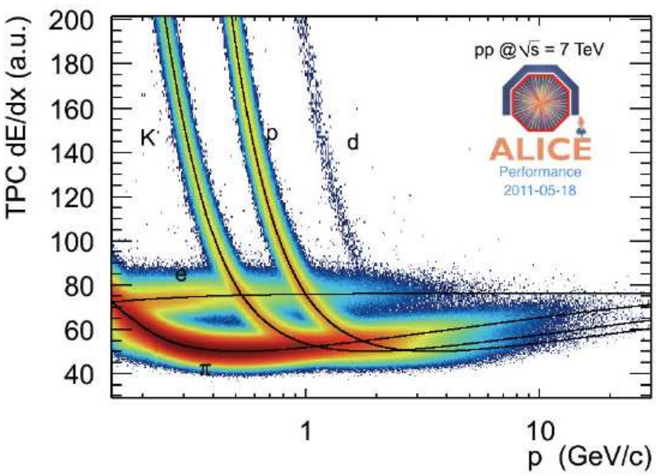

Figure 2.7: *The measured energy loss per unit length as a function of particle momentum in the TPC gas (pp at $\sqrt{s}$ = 7 TeV).*

of the gas mixture used, with a high voltage of 100 kV at the central electrode that results in a maximum drift time of about 90 μs. The TPC identifies particles in the region of the relativistic rise momenta, up to 50 GeV/c. The Bethe-Bloch equation, in fact,

$$\langle dE/dx \rangle = C_1/\beta^2 \left(ln(C_2 \beta^2 \gamma^2) - \beta^2 + C_3 \right)$$

with $\gamma = 1/\sqrt{1-\beta^2}$ and detector-specific constants C_1, C_2 e C_3 relates the mean energy loss per path length, $\langle dE/dx \rangle$, to the velocity β of the particle. Combining the momentum information with the measured dE/dx value yields the particle mass, its identify. Despite its data volume and speed, only such a tracking detector can guarantee the desirable performance at the order of 20 000 particles within the acceptance. In Fig.2.7 a TPC performance plot is shown (up to about 15 GeV/c).

2.2.1.3 Time-Of-Flight detector (TOF)

The Time-Of-Flight [49](Fig. 2.8) detector is a large area array devoted to particle ID in the intermediate momentum range $0.2 < p_t < 3$ GeV/c, below about 2.5 GeV/c for pions and kaons, up to 4 GeV/c for protons, with a π/K and K/p separation better than 3σ (in Fig. 2.9 a TOF performance plot). It covers the central pseudorapidity region $|\eta| < 0.9$. The TOF, coupled with the ITS and TPC for track and vertex reconstruction and for dE/dx measurements in the low-momentum range (up to about 1 GeV/c), provides event-by-event identification of large samples of pions, kaons, and protons. In addition, at the inclusive level, identified kaons allow invariant mass studies, in particular the detection of open heavy-flavored states and vector-meson resonances such as the ϕ meson. It measures the time of flight of the individual particles coming from the TPC with a very good resolution (about 120 ps). The detector covers a cylindrical surface of polar acceptance $|\theta - 90^0| < 45^0$. It consists of 18 azimuthal sectors in ϕ with 5 segments in z. The basic unit of the TOF system

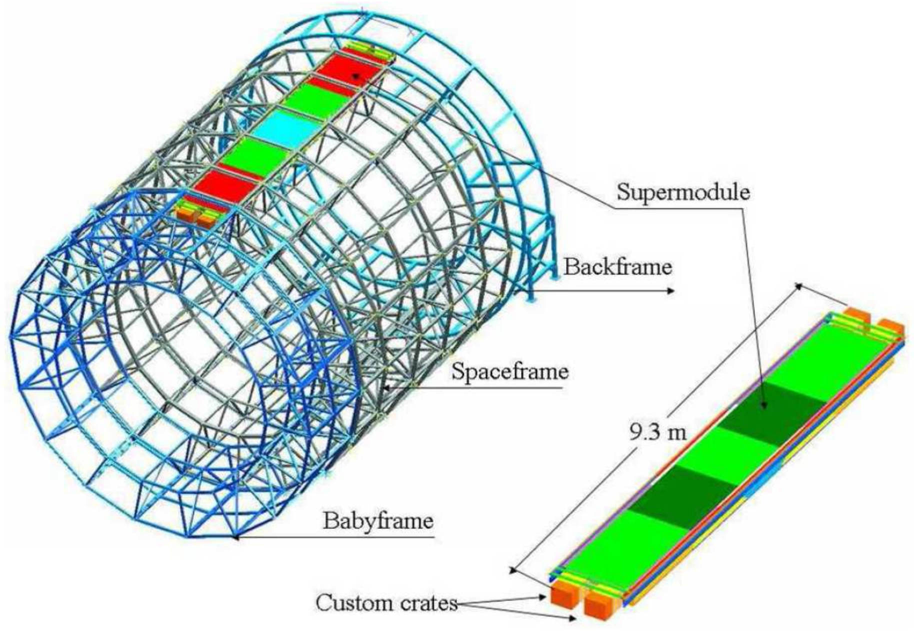

Figure 2.8: *Schematic drawing of the TOF super-module, consisting of 5 modules, in the ALICE spaceframe.*

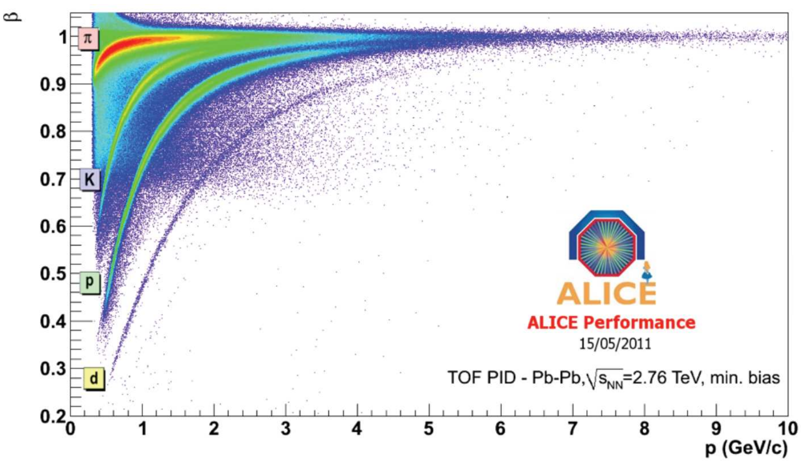

Figure 2.9: *The plot shows the dependence of the particle velocity measured by TOF on the particle momentum (Pb-Pb collisions).*

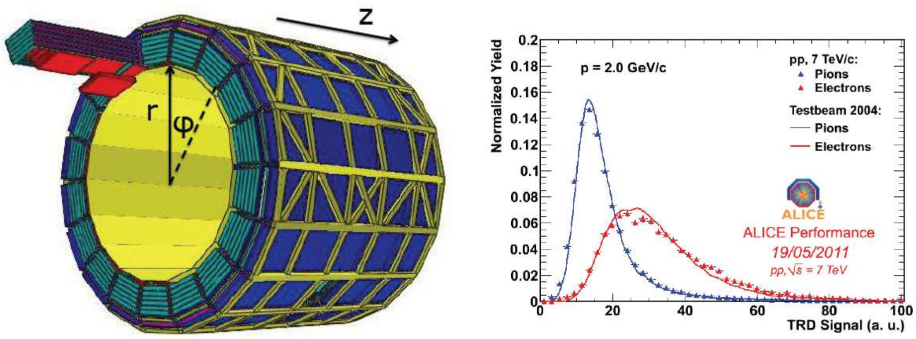

Figure 2.10: *Overview of the ALICE TRD. A cylindrical coordinate is applied. In the taking period 2010 7 out of 18 supermodules were installed, covering* $|\eta| < 0.9$ *respectively* $340° < \varphi < 40°$ *and* $140° < \varphi < 220°$ *(left).Charge deposit for a track segment in a chamber, called tracklet, for electrons (red) and pions (blue). A higher average charge deposit is measured for electrons, also due to the absorption of transition radiation photons in the drift gas. The charge deposit distributions from data are in good agreement with the distributions from testbeam measurements (right).*

is an MRPC strip 1220 mm long and 130 mm wide. The RPC is a gaseous detector with resistive electrodes.

2.2.1.4 Transition Radiation Detector (TRD)

The TRD [51] (see Fig.2.10) provides electron identification in the central barrel for momenta grater than 1 GeV/c, where the pion rejection capability through energy loss measurement in the TPC is no longer sufficient. In addition to that provided by ITS and TPC, it allows production rates of quarkonia near mid-rapidity, as well as the dilepton continuum in Pb-Pb and in p-p, to be measured. Using the impact parameter determination provided by ITS, it is also possible to measure open charm and beauty in semi-leptonic decays. It is segmented in 18 super modules in φ, each containing 30 modules arranged in 5 stacks along z and 6 layers in radius. Each detector element consists of a radiator, a drift section and a multi-wire proportional chamber section with pad readout. The layers are placed at a distance of 2.90 m

$< r < 3.68$ m from the beam line; they cover the full azimuth and a pseudorapidity range $|\eta| < 0.84$.

2.2.1.5 Electromagnetic calorimeters: PHOS and EMCal

The PHOton Spectrometer [53] is an electromagnetic calorimeter of high granularity consisting of 17280 detection channel of lead-tungstate crystal of 2.2 × 2.2 × 1.8 cm^3 dimensions, coupled to large area PIN diodes with low noise preamplifiers. It is made up of five modules and is placed on the bottom of the ALICE apparatus at a distance of 460 cm from the beam line. It will cover approximately a quarter of a unit of pseudorapidity ($|\eta| \leq 0.12$) and 100° in φ. The PHOS electromagnetic calorimeter is optimized for measuring photons in momentum range between 0.5 up to 10 GeV/c, π^0's between 1 - 10 GeV/c and η mesons, 2- 10 GeV/c. The main physics topic of the PHOS detector: thermal and dynamical parameters of the initial phase of the collision, in particular the initial temperature, via direct single photons and di-photons, jet quenching as a probe of deconfinement, studied via high p_T π^0.

EMCAL [54] was not present at original plan for ALICE. It (Fig. 2.11) is a Pb-scintillator sampling calorimeter with cylindrical geometry, placed adjacent to the L3 magnet coil at a radius of about 4.5 m from the beam line. It covers the pseudorapidity region $|\eta| < 0.7$ and $\Delta\varphi = 107°$ and is positioned approximately opposite to the PHOS in the azimuthal direction. Limitations on the weight and size of the detector were required. It is much larger than PHOS but with lower granularity and worse energy resolution.

The EMCal has to explore aspects related to the physics of jet and in particular of jet quenching, an effect due to the interaction of energetic partons with dense matter, relevant to the study of energy loss and interaction of high energy partons in a dense medium. Int provides fast and efficient trigger (L0, L1) for hard jets, photons and electrons and also measures the neutral component of jets allowing the

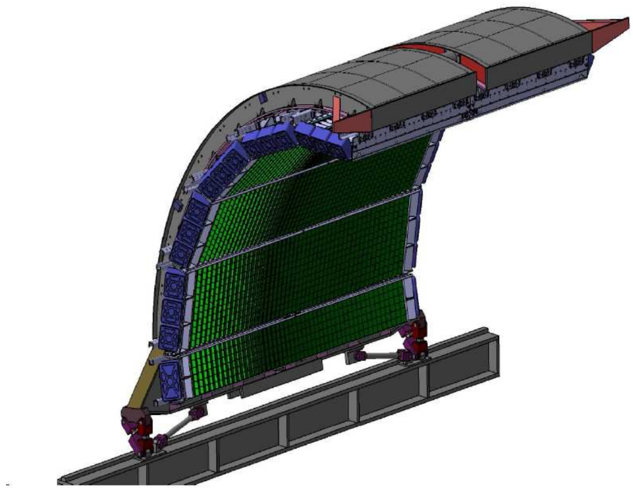

Figure 2.11: *A perspective view of the EMCal in its dedicated support structure is shown. Individual super modules are illustrated with front-end electronics crates mounted on the ends, just beyond the support structure.*

full reconstruction of jets in all collisions systems. It has, together with the TPC, a good jet energy resolution and an excellent sensitivity to the full range of jet-quenching effects expected at the LHC.

2.2.2 Forward detectors

Muon spectrometer

The Muon Spectrometer [55] consists of different absorbers, a dipole, five tracking stations and two trigger stations. The main components of the spectrometer are shown in Fig. 2.11. The front absorber (made of carbon and concrete) suppresses all particles except muons coming from the interaction vertex. The inner beam shield protects the chambers from background originating from particles at small angles. It is made of tungsten, lead and stainless steel to minimize the background arising from primary particles emitted in the collision and from their showers produced in the beam pipe and in the shield itself. The tracking system is made of 10 cathode pad/strip

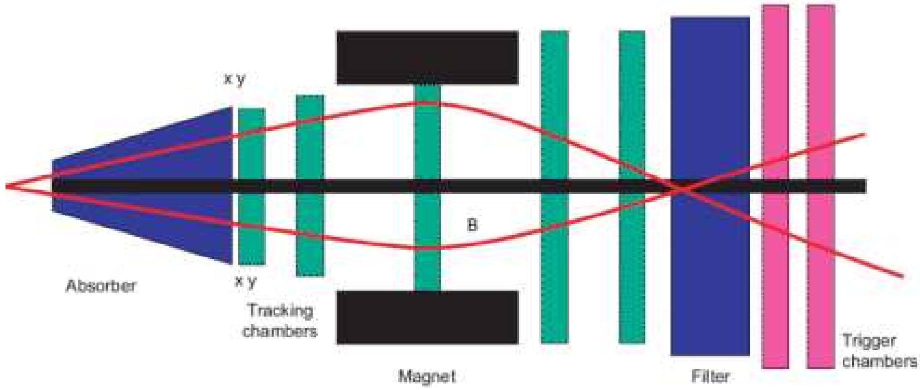

Figure 2.12: *The main components of the ALICE muon specrometer.*

chambers arranged in 5 stations of 2 chambers each. The spatial resolution should be better than 100 mm and all the chambers are made of composite material ($< 3\%$ X0 per chamber) to minimize the scattering of the muons in order to obtain the required resolution. The trigger system is designed to select heavy quark resonance decays. The selection is made on the p_t of the two individual muons. The 4 planes of RPCs (Resistive Plate Chambers) arranged in 2 stations and positioned behind a passive muon filter provide the transverse momentum of each μ. The spatial resolution is better than 1 cm. Special front-end electronics have been designed to obtain the time resolution of 2 ns necessary for the identification of the bunch crossing. The dipole magnet is positioned at about 7 m from the interaction vertex and it is one of the biggest warm dipoles in the world (free gap between poles $\approx$ 3 m, height of the yoke $\approx$ 9 m). The magnetic field (B = 0.7 T, 3 Tm field integral) is defined by the requirements on the mass resolution. The muon spectrometer detects and identifies muons and in particular it measures the production of heavy-quark vector-meson resonances (J/Ψ,Ψ',Υ, Υ', Υ''), as well as the ϕ meson, in the $\mu^+\mu^-$ decay channel with a sufficient mass resolution to separate all states. Furthermore it will be possible to study the production of open flavors measuring the e-μ coincidences, where the muon is detected by the muon spectrometer and the electron is detected by the TRD.

Zero-Degree Calorimeter (ZDC)

The ZDC [56] provides an estimate of the impact parameter of the heavy-ion collisions by the measurement of the number of spectator nucleons which is related to the energy carried forward (beam direction). The ZDC consists of two sets of two compact calorimeters (neutron and proton calorimeters) placed at 116 m from the IP on both sides in the machine tunnel. The spectator neutrons and protons are spatially separated by the magnetic elements of the LHC beam line, therefore the neutron calorimeter is placed in between the two beam pipes at $0°$ with respect to the LHC beam line, and the proton calorimeter is placed externally on the side where positive particles are deflected.

Photon Multiplicity Detector (PMD)

The PMD [57] measures the multiplicity distribution of photons (e.g. decay products from π^0 and η) in the forward region ($2.3 < \eta < 3.7$, full azimuth). It consists of two gas proportional chambers. Between these a lead converter is located. The plane in front of the converter is used as a veto for charged particles while the information from the second plane is used to identify photons. The detector is positioned at a 3.64 m distance from the nominal interaction point.

Forward Multiplicity Detector (FMD)

The Forward Multiplicity Detector [58](FMD) is designed to measure the charged particles that are produced in the collisions and which are emitted at small angles relative to the beam line direction. The FMD is the primary detector to measure the multiplicity distribution of charged particles over a wide kinematical range (rapidity coverage in the interval $1.7 < |\eta| < 5.1$ corresponding to an angular interval of about 0.75 degrees to 21 degrees with respect to the beam direction.

V0

The V0 [59] detector consists of two segmented arrays of plastic scintillator counters, placed around the beam-pipe on either side of the IP: one at z = 90 cm (in front of the absorber), covering the pseudorapidity range -3.7 $\leq \eta \leq$ -1.7, and the other at z = -340 cm, covering the pseudorapidity range $2.8 \leq \eta \leq 5.1$. The V0 is a trigger detector that will provide minimum-bias trigger for all colliding systems to the central barrel detectors and three centrality triggers in Pb-Pb collisions (multiplicity, central and semi-central).

T0

The T0 detector consists of two arrays of 12 Cherenkov counters each, mounted around the beam-pipe. One array is placed at -72.7 cm from the IP, the distance imposed by the layout and position of the muon spectrometer and of the other forward detectors, and has a pseudorapidity coverage of -3.28 $\leq \eta \leq$ -2.97. The other array is placed at 375 cm on the opposite side of the IP, grouped together with other forward detectors, and has a pseudorapidity coverage of $4.61 \leq \eta \leq 4.92$. In the radial direction they are placed as close as possible to the beam pipe to maximize the trigger efficiency. The T0 detector, together with the V0, will provide fast trigger signals. The main goals of the T0 are as follow:

- to measure the event time with a precision better than 25 ps;
- to provide the TOF with a start time signal, that is the real time of the collision plus a fixed delay and is independent of the position of the primary vertex;
- to measure the interaction vertex position with a precision of $\pm$ 1.5 cm and to provide a L0 trigger when the position is within a predefined window to discriminate against beam-gas interactions;
- to provide a wake-up signal to the TRD, prior the L0 trigger;
- to generate minimum-bias and multiplicity trigger signal (based on threshold on multiplicity in heavy-ion collisions).

It contributes to the L0 trigger of the experiment so its dead time has to be less than the bunch-crossing period in p-p collisions (25 ns).

2.3 The High Momentum Particle Identification Detector

The High Momentum Particle IDentification detector [71, 72, 73, 74] (Fig. 2.13) was the first detector installed inside the ALICE solenoid (2006 Sept.). Despite its geometrical acceptance (only 5 % of the barrel), the Cherenkov detector can play a central role in the ALICE physics program, both in pp and PbPb. In this chapter an overview of the Cherenkov detector will be given starting with a brief description of the layout, then its principle of operation. In the last sections results on the detector performance from 2010 data will be present.

2.3.1 Design considerations

The High-Momentum Particle Identification Detector is dedicated to inclusive measurements of identified hadrons at p > 1 GeV/c [76], enhances the PID capability of ALICE by enabling identification of charged hadrons beyond the momentum interval attainable through energy-loss (in ITS and TPC) and time-of-flight measurements (in TOF). The detector has been optimized to extend the useful range for p/K and K/p discrimination up to 3 GeV/c and 5 GeV/c, respectively. The HMPID was designed as a single-arm array with an acceptance of 5% of the central barrel phase space. In addition the identification of light nuclei and anti-nuclei (d, t, 3He, α) at high transverse momenta in the central rapidity region can also be performed. Since the particle identification plays a fundamental role in the physics topics of ALICE, HMPID can contribute to the following items [78]:

Figure 2.13: *The cupola-like structure of the HMPID detector. The picture has been taken during a installation phase.*

- the measurement of global event characteristics like event topology,
- inclusive momentum spectra of identified particles and particle ratios;
- particle correlations (HBT);
- the measurement of the ϕ decay in the K^+K^- channel.

2.3.2 Detector layout

The High Momentum Particle Identification detector [75] consists of an array of seven identical RICH detector modules of 1.4×1.3 m^2 each, arranged in a cupola-like structure. They are mounted in an independent support cradle fixed in the space frame in the two o'clock position. The HMPID is located at radial distance of about 4.7 m (Fig.2.14) from the interaction point. Its acceptance covers the region between

-0.6 < η < 0.6 in pseudo-rapidity and 57.6^0 in azimuth, for a total active area of about 11 m^2. Some relevant parameters of the HMPID are summarized in Fig.2.18. The module is basically made up of a radiator for the Cherenkov photon emission (closed at one side by a quartz window), a proximity focusing gap, a Multi Wire Proportional Chamber closed by a photocathode. The radiator is a 15 mm thick layer of low chromaticity C_6F_{14} (perfluorohexane) liquid with an index of refraction of $n = 1.2989$ at $\lambda = 175$ nm corresponding to $\lambda_{min} = 0.77$. The Cherenkov photons are detected by a photon counter which use a thin layer of CsI deposited onto the pad cathode of the MWPC. The photo-detector, filled with pure methane and operated at ambient temperature and pressure, is closed on one side by an end-flange which supports six CsI photocathodes 64 × 40 cm^2 each, segmented into 8 mm × 8.4 mm pads, for a total of 161280 channels in the 7 chambers. On the opposite side, a panel supports three C_6F_{14} radiator vessel placed at distance of 80 mm from the anode wire plane [77]. The liquid radiator containers consist of trays made out of NEOCERAM with the fused silica plates used as UV-transparent windows. The quartz window is 5 mm thick.

A C_6F_{14} liquid circulation system is required to purify, fill and empty at a constant flow. Filters are implemented in the circulation system in order to remove contaminants and achieve the best transparency in the UV region. The total gas volume of 1.4 m^3 of pure CH_4 is split in the seven independent RICH modules.
The front-end electronics is based on two dedicated ASIC chips: GASSIPLEX (a low-noise signal processor), and DILOGIC (a digital signal processor providing zero suppression and pedestal subtraction).

The GASSIPLEX-07 chip is a 16-channel analogue multiplexed low-noise signal processor featuring a dedicated filter to compensate for the long ion drift tail, a semi-Gaussian shaper and internal protection against discharges. During the commissioning before installation the number of dead or noisy pads was found to

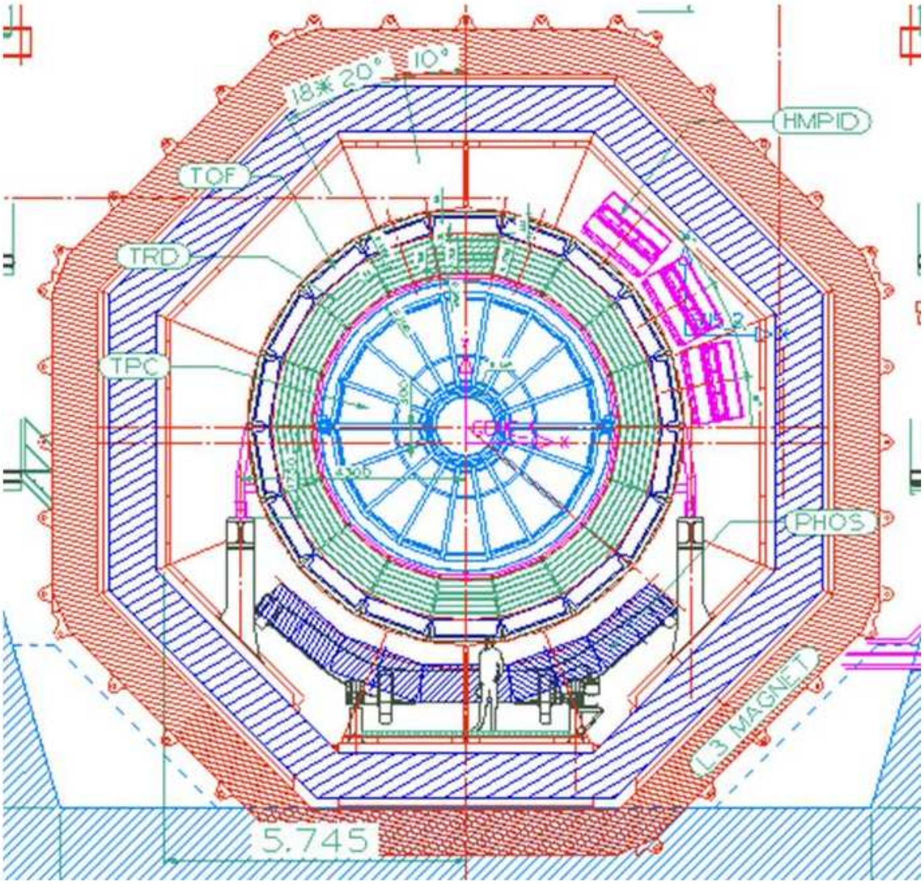

Figure 2.14: *ALICE 2D cut views along the xy direction. HMPID detector is located at about 4.7 m from the primary vertex.*

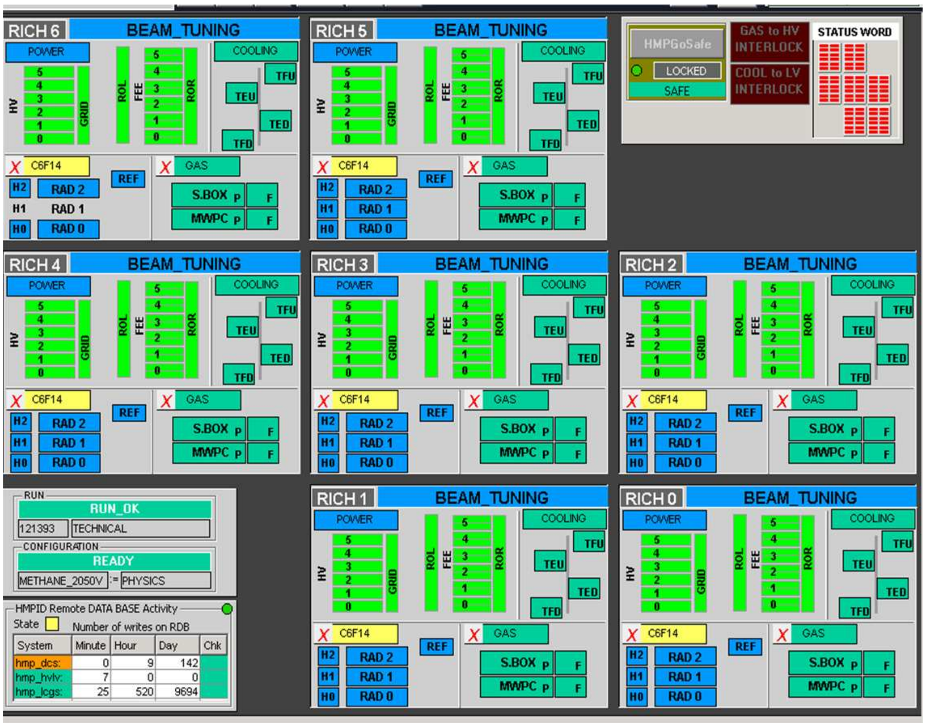

Figure 2.15: *Detector-oriented views of the HMPID DCS control panel.*

be less than 200 out of 161 280 pads. In the HMPID application the GASSIPLEX analogue output is presented to the input of a commercial 12-bit ADC. The multiplexing level is 3 chips (48 channels) per ADC at a maximum frequency of 10 MHz. The digitization and zero-suppression time does not depend on the occupancy, being determined only by the multiplexing rate.

The DILOGIC chip is a sparse data scan readout processor providing zero suppression and pedestal subtraction with individual threshold and pedestal values for up to 64 channels. Several chips are daisy-chained on the same 18-bit output bus. Asynchronous read/write operations are allowed. Data are read out via the standard ALICE Detector Data Link (DDL). The ALICE DDL Source Interface Unit (SIU) is housed, in the Readout and Control Board (RCB) which interfaces the detector readout electronics with the DAQ and Trigger subsystems. Since momentum information is fundamental to exploit the HMPID detector, only events for which the TPC information is available are of interest and the HMPID can perfectly cope with the readout rates foreseen for the TPC. The safe operation of the detector under commissioning and in normal operation is achieved via the Detector Control System (DCS), developed within the HMPID project. Since July 2007 all HMPID modules are fully powered and controlled by DCS. Fig. 2.15 shows the detector-oriented view of the fully powered HMPID, with most subsystems operational. The HMPID DCS controls the subsystems of gas, cooling, liquid circulation and transparency, high-voltage, low-voltage and the front end electronics. For expert operation, the DCS provides access down to a single hardware element of the HMPID, in the device oriented view.

2.3.3 Principle of operation

When a relativistic charged particle passes through the HMPID radiators (Fig. 2.17), Cherenkov photons are emitted in the UV region overcoming the quarts window (it is transparent to such photon energies). The photons travel along the proximity gap and are detected by a photon converter which uses the technology of a thin layer of CsI deposited onto a pad-segmented cathode as described in the previous section. On each pad the Cesium Iodide film works as a photon converter by means of the photoelectric effect (for CsI $E_{band-gap}$ = 6 eV). The MWPC detects charged particles by the avalanche they can produce close to the anodes, therefore the HMPID technology allows to detect both photons and particles at the same time. The charge yield due to the MIP[1] passage is higher than the photoelectron yield therefore it is possible to distinguish the two signals through charge detection. More charge implies more pads lightened up, therefore grouping sets of close pads (clusters), a MIP cluster

[1]MIP is the terminology to indicate the particle crosses the HMPID chambers.

Pseudo-rapidity coverage	$-0.6 < \eta < 0.6$
Azimuthal coverage (rad)	57.61°
Radial position	5 m
Segmentation in φ	3-fold
Segmentation in z	3-fold
Total number of modules	7
Detector active area	$10\ m^2$
Detector thickness radially	$X/X_0 = 18\%$
Radiator thickness	15 mm
Radiator medium	Liquid C_6F_{14}
Refractive index	1.2989 at 175 nm
Independent radiator trays	3 per module (21 total)
β threshold	0.77
Detector gas	CH_4
Gas volume	$1.4\ m^3$
MWPC anode–cathode gap	2 mm
Operating voltage	2050 V
Photon converter	Cesium Iodide (CsI)
CsI thickness	300 nm
Quantum Efficiency (QE)	> 25% at 175 nm
Number of Photo-Cathodes (PC)	42
Number of pads per PC	3840 (161 280 total)
Pad size	$8.0 \times 8.4\ mm^2 = 67.2\ mm^2$
Front-end chip (GASSIPLEX-07-3)	10 080
Peaking time	1.2 μs
Readout chip (DILOGIC-3)	3360
Front-end cards	3360
Readout cards	672
ADC (12-bit)	3360
Power consumption per module	500 W (total 3.5 kW)
Number of DDL	14
Multiplexing frequency	10 MHz (maximum)
Multiplexing time	5 μs at 10 MHz
Readout time (for 12% occupancy)	< 300 μs
Event size (for 12% occupancy)	< 0.1 MB
Number of readout channels	161 280
Occupancy ($dN_{ch}/d\eta = 8000$)	12%

Figure 2.16: *Synopsis of HMPID parameters.*

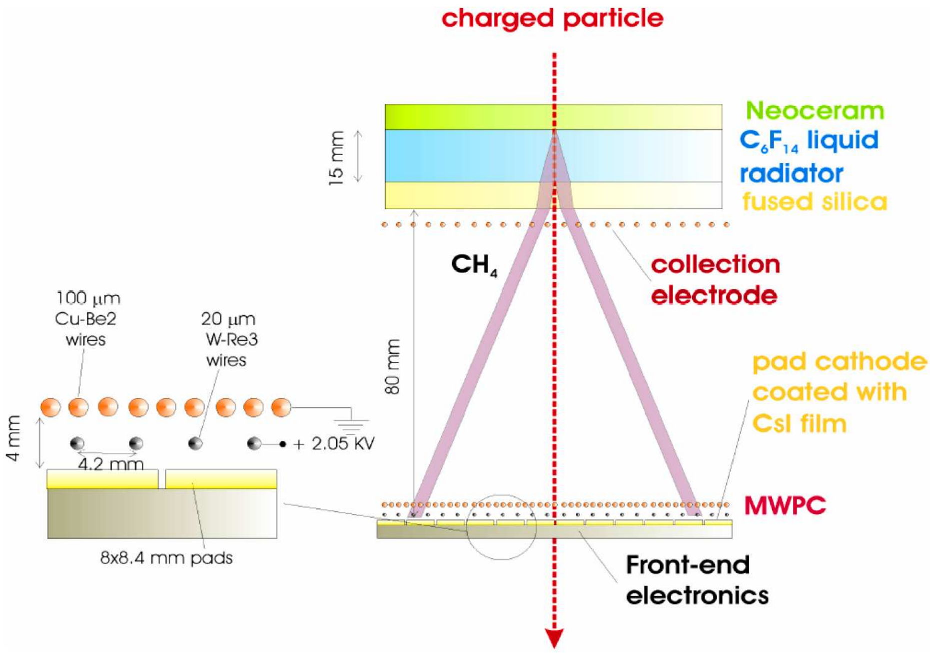

Figure 2.17: *Schematic picture of the module layout and how it operates. Each HMPID module is made up of a radiator for a Cherenkov photon emission (C_6F_{14}), a proximity focus gap (80 mm), the Multi Wire Proportional Chamber and a photochatode (pad chatode coated with CsI film.)*

will contain more pads than a photoelectron cluster. The charge distribution will be a superposition of a Landau for the MIP and a background due to photon cluster charge. The analog read-out of the pad charge allows also to calculate the charge centroid of the clusters that can be considered an estimate of the impact point of the MIP/photon at the photocathode plane. To discriminate photon cluster to MIP cluster a charge cut is applied: Q > 150 ADC selects MIP clusters. This is very important because the knowledge of the impact point of the particle makes a one-to-one Cherenkov angle (θ_C) association possible. The minimum distance d_{MIN} between the extrapolated track point on the HMPID photocathode plane of a given chamber and the coordinate of the nearest centroid, of a charge compatible with a MIP cluster is applied in the selection of the tracks at HMPID level. The selection reduced the probability of mismatch of a track with the MIP cluster of another particle even if the efficiency decreases. We denote this cut as *matching selection*. The extraction of the mean Cherenkov angle is made by the Hough transformation method. The HTM is an efficient implementation of a generalized template matching strategy for detecting complex patterns in binary images. For Cherenkov pattern, the Hough method finds the number of candidate photons related to the same Cherenkov cone and photon by photon it extracts the experimental error σ_{Ckov} according to the well know detector performances. In Fig. 2.18 a typical Cherenkov ring in the HMPID detector is shown (pp collisions at $\sqrt{s}$ = 7 TeV).

2.3.4 Detector performance: results from 2010 data

In this section an overview of the most important performance results using 2010 data is presented [79]. The HMPID performance study was carried out on minimum bias events selected by online trigger and offline physics event selection from $\sqrt{s}$ = 2.76 TeV and $\sqrt{s}$ = 7 TeV p-p collisions and $\sqrt{s_{NN}}$ = 2.76 TeV Pb-Pb collisions. The z component of the primary vertex is required to fall within ± 10 cm of the IP. Good tracks from ITS + TPC are selected based on the common 2010 primary track definition of ALICE [2] and propagated up to the HMPID. The propagated tracks are required to point within 3 cm of the measured charged particle position in HMPID, that is known with sub-mm precision along the anode wire direction and with less than 4 mm precision perpendicular to the anode wires.

Fig.2.19 shows the most probable value and sigma of the MIP charge distribution extracted from the Landau fit.

Fig. 2.20 shows the number of photon clusters from data and simulation as a

[2] for more details on the event and track selection see chapter 4 and 5.

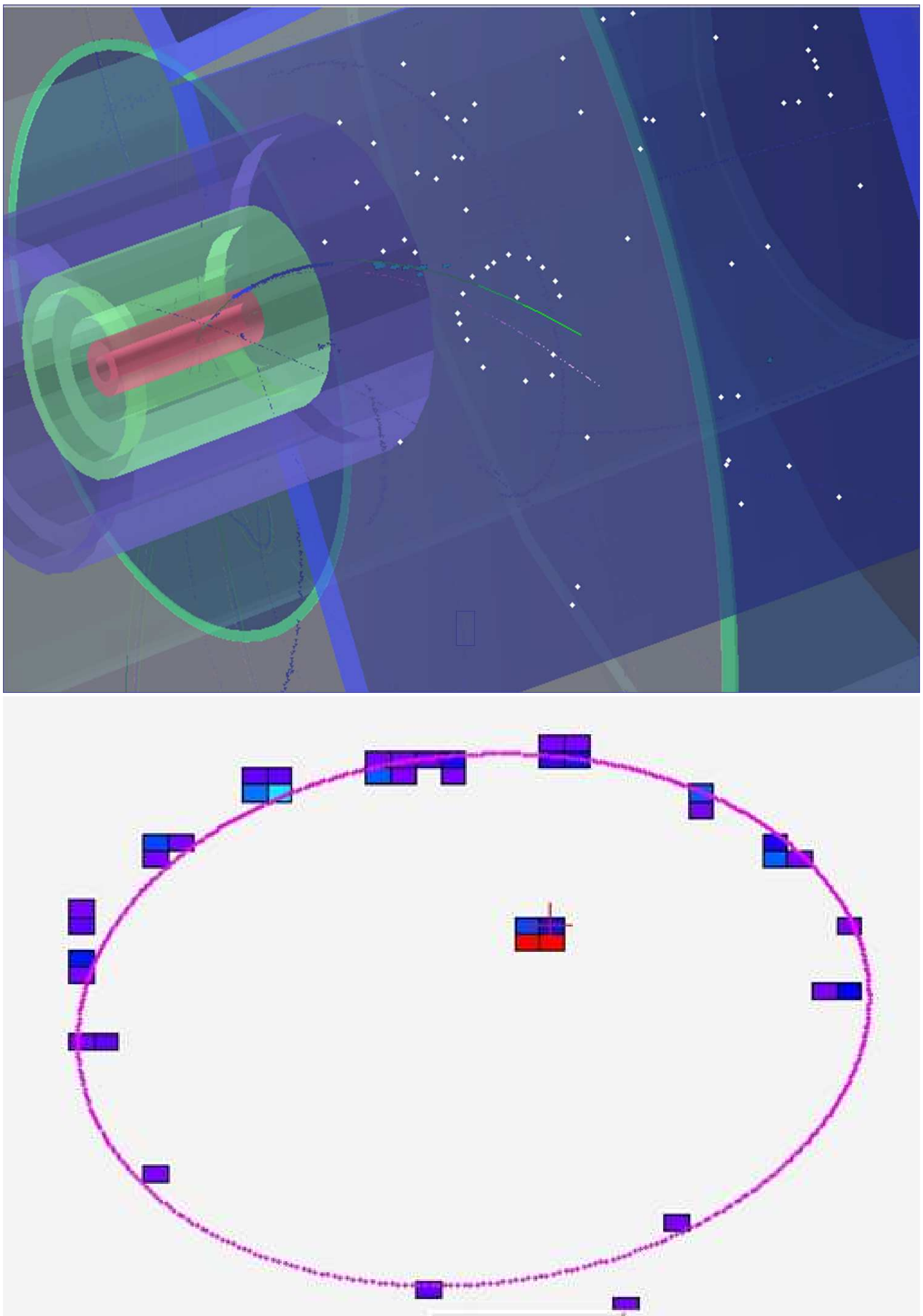

Figure 2.18: *Cherenkov ring in the HMPID detector (pp collisions at $\sqrt{s}$ = 7 TeV).*

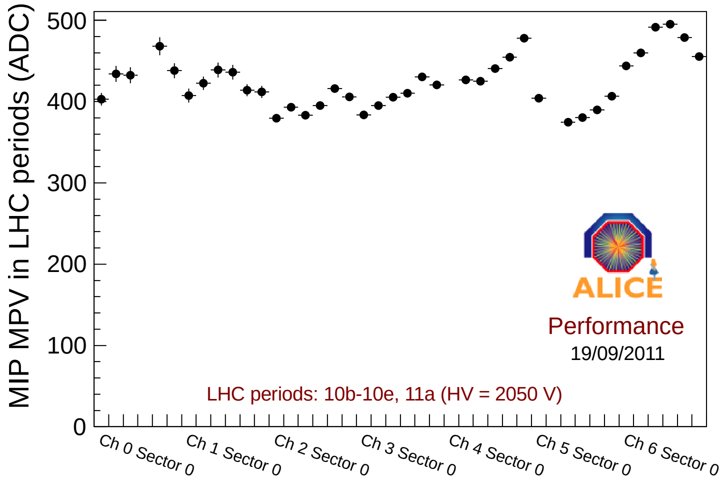

Figure 2.19: *Charged particles (MIPs) per HV sectors.*

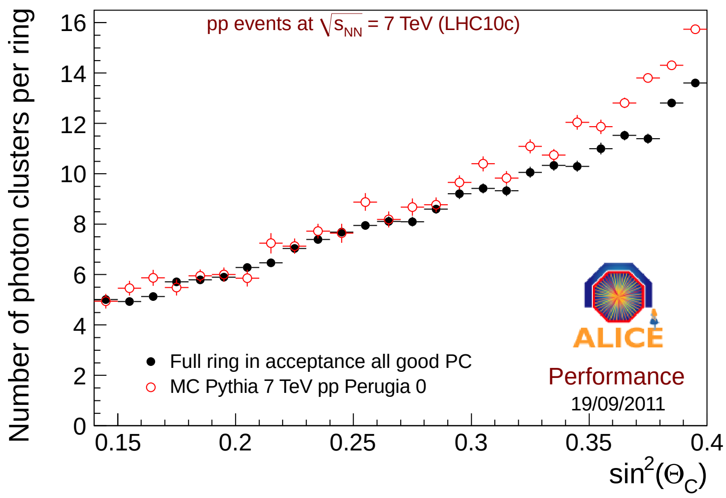

Figure 2.20: *Number of photon clusters from data and simulation as a function of* $\sin^2\theta_C$ *for rings fully contained in the photocathodes. The discrimination between MIP cluster and photon cluster is performed using a charge cut (Q > 150 ADC selects MIP cluster.)*

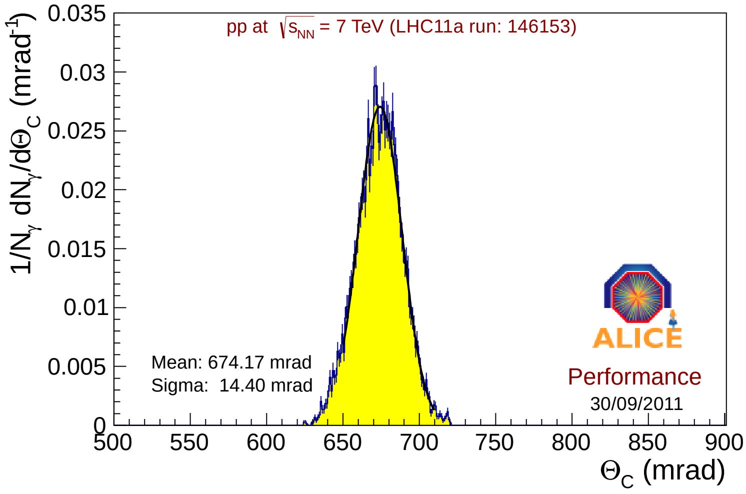

Figure 2.21: *Single-photon Cherenkov angle resolution obtained for $\pi^{\pm}$ at $p > 1.5$ GeV/c with $d_{MIP-track} < 3$ cm.*

function of $\sin^2\theta_C$ for rings fully contained in the photocathodes. In the simulation, the nominal gain (35 ADC) nominal QE and nominal C_6F_{14} radiator transparency are used. The trend and the absolute number of the photon cluster number show good agreement between data and simulation, where the number of photon cluster depends on the radiator thickness L, detector factor of merit N_0 and the $\sin^2\theta_C$ as shown in the following equation:

$$N_{photons} = 370 \times L \times N_0 \times sin^2\theta_C \tag{2.4}$$

While the above parameters are strictly determined by the HMPID performance the resolution of single-photon Cherenkov angle and particle identification are influenced by the properties of the propagated track to the HMPID (located 4.7 m from the interaction point with significant material budget in front with respect to other RICH detectors).

Fig. 2.21 shows the single-photon Cherenkov angle resolution obtained for $\pi^{\pm}$ at $p > 1.5$ GeV/c with $d_{MIP-track} < 3$ cm. The measured resolution: 14.4 mrad is close to the nominal value of 12 mrad obtained with ideal tracking in beam test.

2.3.5 Challenges in tracking and Cherenkov angle reconstruction

After enough statistics collected, some relevant improvements in tracking and reconstruction have been carried out in the last part of 2011. We remark that particle identification in the HMPID requires the particle's track to be extrapolated from the central tracking devices of ALICE and associated with the corresponding cluster of the MIP in the HMPID cathode plane as explained in the first part of this chapter. Since the HMPID is located at 5 m from the primary vertex, tracks have to be propagated through significant material budget after the TPC, with respect to other RICH detectors. Precise knowledge of the track parameters is essential, since the Cherenkov ring reconstruction resolution depends on them. Reconstructed tracks are propagated up to the HMPID chambers by means of a dedicated algorithm. The standard algorithm used was tuned already in the STAR experiment [80, 81, 82, 83, 84, 85], and it propagates the track from the last point in the TPC or TRD detectors to the HMPID chamber planes by means of a simple helix. In the real ALICE environment with its 0.5 T magnetic field and a significant material budget in front the HMPID, this procedure does not allow to obtain a good track angular resolution at the chambers entrance to perform the Cherenkov angle measurement, especially in the low momentum region (below 2 GeV/c). As we will show in the Chapter 4, the distribution of the distance between primary tracks intersection point at the HMPID plane and the corresponding MIP point have a distance greater than 2 cm. To obtain a satisfactory Cherenkov angular resolution it has been necessary to apply a strong cut ($d_{MIN} < 0.7$ cm) on this matching selection losing great available statistics. Significant effort has been devoted to improve the

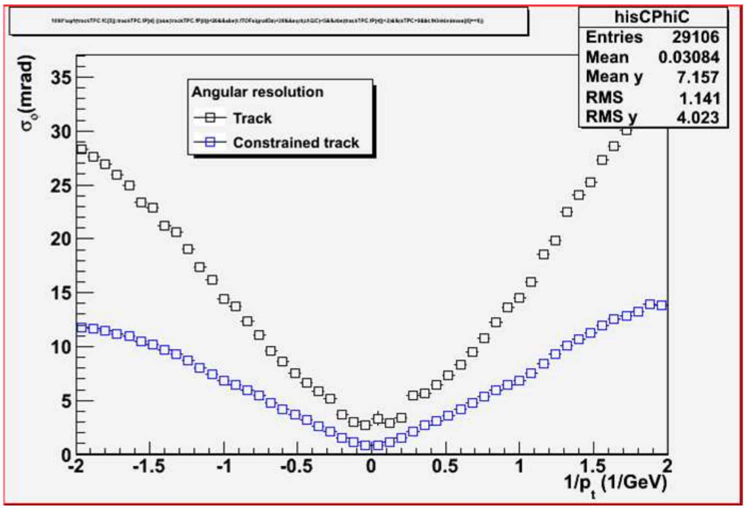

Figure 2.22: *Track angular resolution for constrained and uncostrained tracks. Negative particles correspond a negative value on x-axis.*

tracking during this year. In the improved tracking the running track is picked up at the last TPC point and propagated up to the HMPID through the TRD and TOF. The improved extrapolation algorithm takes better into account the energy loss and the dependence of the magnetic field value on the distance from the interaction point. In particular with the new procedure it is possible to exploit the precise knowledge (1 mm precision) of the HMPID MIP information in the track fitting. Fig.2.22 shows the track angular resolution for constrained and unconstrained tracks, the improvement obtained is evident. The constrained track is refitted using MIP information, while the other one is the results of a simple track propagation up to the HMPID planes. Improved tracking information brings the resolution of the Cherenkov angle close to the design values. The n-σ separation obtained for new tracking (*standard tracking*) and old tracking (*improved tracking*) will be present during the course of this thesis.

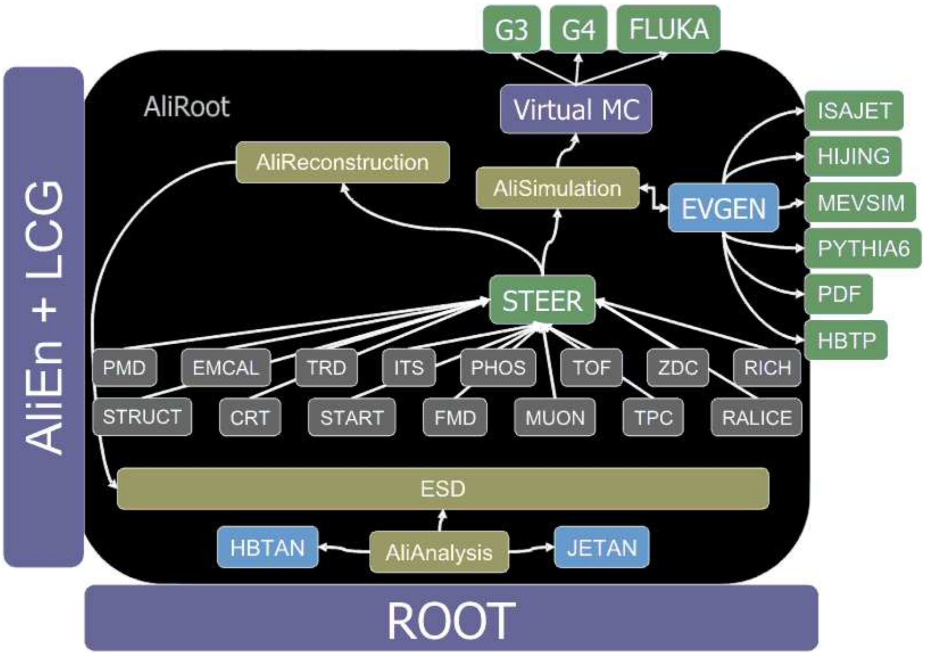

Figure 2.23: *Schema of the AliRoot framework.*

2.4 The AliRoot framework

AliRoot [62, 63] is the ALICE offline framework for simulation, alignment, calibration, reconstruction, visualization, quality assurance, and analysis of experimental and simulated data. It is shown schematically in Fig.2.23. It is based on the ROOT [64] framework and most of the code is written in C++ with some parts in Fortran. The AliRoot functionalities are summarized in two main steps: simulation and reconstruction. In Fig. 2.24 interaction of the reconstruction code with the other parts of AliRoot. In the first one, event generation, transport and digitization are performed.

In the second, raw data are produced and cluster finding and track reconstruction are applied.

Event generation:

A collision is simulated by an event generator (e.g PYTHIA [66], Phojet [67], or

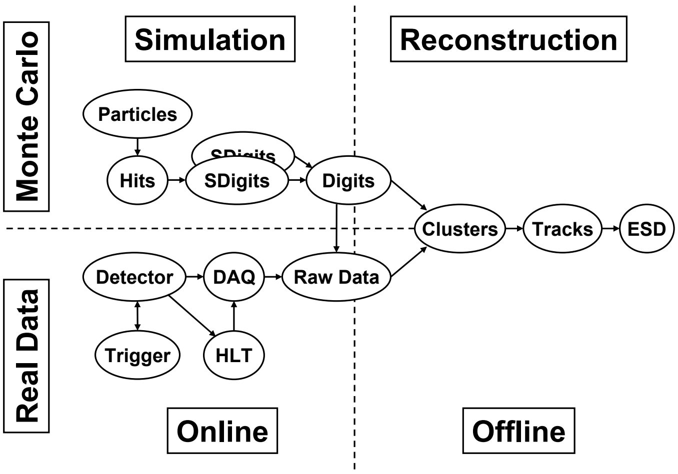

Figure 2.24: *Interaction of the reconstruction code with the other parts of AliRoot.*

HIJING [65]) that is interfaced with AliRoot. The kinematics tree produced will contain the full information about the generated particles (type, momentum, charge, production process, originating particle, and decay products).

Transport:

The particles are propagated through the detector material. The particles can interact with matter, decay, and create additional particles. These particles have to be propagated through the detector as well. The total number of particles after the transport is significantly larger than the number of particles created in the initial generation step. During this process all interactions of particles with sensitive detector parts are recorded as *hits* that contain the position, time, and energy deposit of the respective interaction ($track\ references$ are stored, mainly needed for the debugging of the reconstruction algorithms - used in the trigger study for the HMPID - in Appendix D). Programs that perform the transport and are interfaced with AliRoot are Geant3 [61], Geant4 [68, 69] , and Fluka [70].

Digitization:

The particle produces a signal in the sensitive part (hit) of the detector and the corresponding digital output is stored as a *summable digit* taking into account the detector's response function. Possible noise is then added to the summable digit and it is stored as a *digit*.

Raw data:

Data are stored in the specific hardware format of the detector. Raw data corresponds to the signals produced by an interaction within the detector. The subsequent reconstruction is identical, both for simulated as well as real events. Particles that interact with the detector usually leave a signal in several adjacent detecting elements or in several time bins of the detector.

Cluster finding:

These signals are combined to form clusters. This allows the exact position or time of the traversing particle to be determined and reduces the effect of random noise. Overlapping signals from several particles in a single cluster are unfolded. This step is performed for each subdetector where due to the different nature of the subdetectors the implementation vary significantly.

Track reconstruction:

The track reconstruction start when the clusters are combined to form tracks that allow the track curvature and energy loss to be calculated with the aim of determining their momentum and particle type. The tracking is a complex global procedure but at same time individual per detector. The global central barrel tracking starts from track seeds in the TPC which are found by combining information from the few outermost pad rows under the assumption that the track originates from the primary vertex. Tracks are then followed inwards using a procedure called the Kalman filter [8]. Further information are updated on the track, for example, a noise term is added. It represents the information loss by stochastic processes such as multiple scattering and energy-loss fluctuations. In the final step all clusters already associated to tracks are removed and the procedure is repeated without requiring that the seeds point to the primary vertex. The result, the so-called TPC-only tracks to which only TPC information contributes, is saved in the reconstruction output. Subsequently, these tracks are complemented with information from the ITS, TRD, and TOF as well as HMPID if the track is in the detector acceptance which produces so-called global tracks.

The output of the reconstruction is called Event-Summary Data (ESD) which contains only high-level information such as the position of the event vertex, parameters of reconstructed charged particles together with their PID information, positions of secondary vertex candidates, parameters of particles reconstructed in the calorimeters, and integrated signals of some subdetectors. This data is further reduced to Analysis-Object Data (AOD) format. These smaller-sized objects contain the information needed for the analysis. Therefore, the transformation procedure may already contain a part of the analysis algorithm, for example track selection. Several AODs, focusing on different physics studies, can be created for a given event.

Chapter 3

Identification efficiency of the ALICE HMPID detector in p-p collisions at $\sqrt{s} = 7$ TeV

3.1 Introduction

The aim of this study is the evaluation of the experimental PID efficiency for the HMPID detector in pp collisions at $\sqrt{s} = 7$ TeV using the V^0's decays. The appearance of decays of a neutral strange particle into two observed charged daughter particles gives rise to the terminology V^0 (V for the decay topology and 0 for the neutral particle).

The HMPID detector is devoted to identifying kaons and pions in the momentum range between 1.5 and 3 GeV/c and protons (and antiprotons) between 1.5 and 5 GeV/c using the Cherenkov technique. It can identify the daughters of the V^0 (pion and proton) produced with momentum range compatible with the HMPID identification range:

$$\Lambda \rightarrow p + \pi^- \tag{3.1}$$

$$\bar{\Lambda} \rightarrow \bar{p} + \pi^+ \tag{3.2}$$

$$K^0_S \rightarrow \pi^+ + \pi^- \tag{3.3}$$

Hence, using the V^0's decays, PID efficiency has been calculated selecting clean samples of Λ, $\bar{\Lambda}$ and K^0_S (as explained in this chapter). Usually, the efficiency is calculated from the Monte Carlo simulation: we took the opportunity to measure the PID efficiency for pions and protons directly from the data (experimental efficiency) in the HMPID momentum range, and at same time, this study provides a useful check for the MC result. We are in favour of using data for the evaluation of the PID efficiency due to several factors, for example, the non-perfect description of the geometry in the simulation and the uncertainties on the estimate of the large material budget thickness between the detector and the primary vertex. In the last part of the chapter, the comparison between MC simulation and data is described. The analysis is performed using the Inner-Tracking-System, the Time-Projection-Chamber and the High-Momentum-Particle-Identification detector.

3.2 V^0 finding procedure in the ALICE experiment

The secondary vertices, coming from the decay of strange particles, can be summarized in three types: *kink*, V^0 and *cascade* (as shown in Fig.3.1).
The **kink vertex** corresponds to the decay into a neutral and a charged particle; this is the case for the K^+ and the K^-.
As mentioned before, the $\mathbf{V}^0$ terminology comes from the decay topology: a neutral particle with quantum number $|S| = 1$ (Λ, $\bar{\Lambda}$ and K^0_S) decays in two daughters with

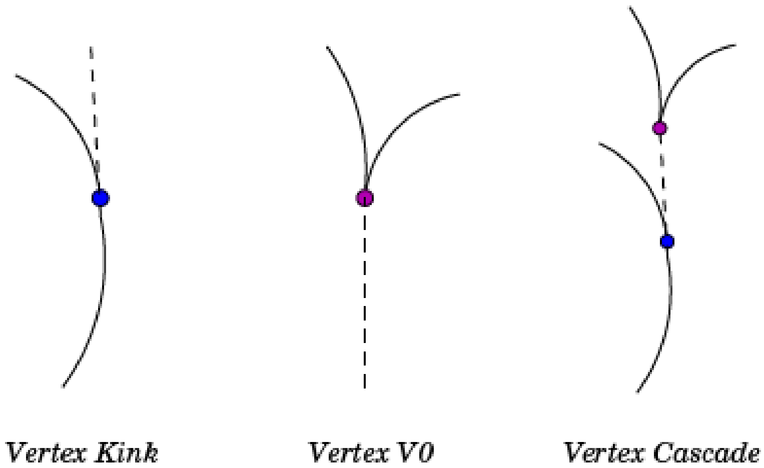

Figure 3.1: *Decay topologies of the strange particles. The solid lines represent the charged particles, where the trajectories are bent due to the magnetic field. The dotted lines are the neutral particles.*

opposite charge.

The **cascade vertex** corresponds to the decay of a charged particle (Ξ, Ω) into a charged and neutral daughter, the latter decaying into two charged particles (i.e. V^0).

In Tab.3.1 the main characteristics of the strange and multi-strange particles are summarized. In this chapter we describe the finding procedure of the V^0 vertex.

The V^0 reconstruction [8, 89] in the ALICE experiment can be done essentially with two main tracking detectors in the ALICE barrel: the Inner Tracking System and the Time Projection Chamber.

The identification of K^0_S, Λ and $\bar{\Lambda}$ is possible applying selections related to the characteristics of the daughter tracks and using their weak decay topologies. In the Fig.3.2 the main parameters concerning the geometrical selection for V^0 reconstruction are shown:

Particles	Mass (MeV/c^2)	cτ	Charged decays	B.R. (%)
		Kink vertex		
K^-	493.677	371.3 cm	$\pi^0 + \pi^-$	21.13 $\pm$ 0.14 %
K^+	493.677	371.3 cm	$\pi^0 + \pi^+$	21.13 $\pm$ 0.14 %
		V^0 vertex		
K^0_S	497.61	2.68 cm	$\pi^+ + \pi^-$	68.95 $\pm$ 0.14 %
Λ	1115.68	7.89 cm	p + π^-	63.9 $\pm$ 0.5 %
$\bar{\Lambda}$	1115.68	7.89 cm	$\bar{p} + \pi^+$	63.9 $\pm$ 0.5 %
		Cascade vertex		
Ξ^-	1321.31	4.91 cm	$\Lambda + \pi^-$	99.887 $\pm$ 0.035 %
Ξ^+	1321.31	4.91 cm	$\bar{\Lambda} + \pi^+$	99.887 $\pm$ 0.035 %
Ω^-	1672.45	4.91 cm	$\Lambda + K^-$	67.8 $\pm$ 0.7 %
Ω^+	1672.45	4.91 cm	$\Lambda + K^+$	67.8 $\pm$ 0.7 %

Table 3.1: *Main characteristics of the strange and multi-strange particles: mass, cτ and charged decays branching ratio (B.R.).*

- **positive and negative daughter impact parameters** (b$^+$ and b$^-$ respectively);
- **distance of closest approach (DCA)**: it is the minimum distance between the two daughters of the V^0 candidate;
- **fiducial zone**: it is the zone where the position of the secondary vertex reconstructed starting from the daughter parameters is expected.
- **decay length**: it represents the distance between the primary and secondary vertex;
- **pointing angle**: it is the angle between the vector momentum of the V^0 candidate ($\vec{P}$) and the vector connecting the primary vertex and the V^0 vertex position.

The first step in the V^0 finding procedure is the selection of secondary tracks. Tracks with a small impact parameter with respect to the primary vertex are rejected. A combination between each secondary track with all the secondary tracks having an

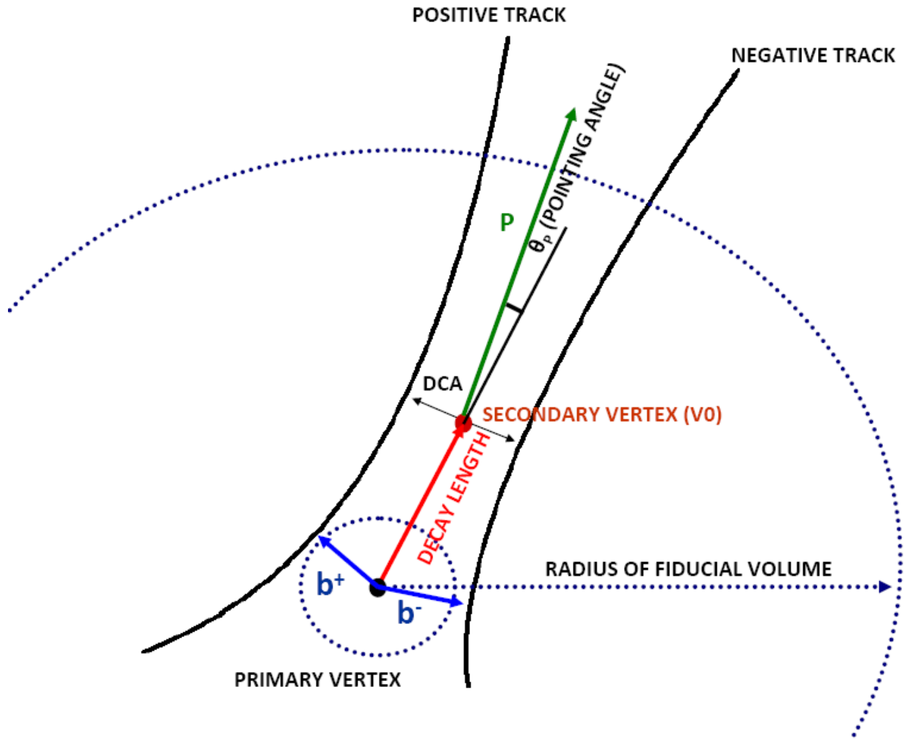

Figure 3.2: *Basic topology of V^0 decays.*

opposite charge is performed in the finding algorithm. Then, a cut on the positive and negative impact parameter (respectively b^+ and b^-) is applied.

A cut on the distance of closest approach (DCA) allows a further selection: if the distance of DCA in space between the two tracks is larger than a given value used in the analysis, such pair of tracks is rejected. Further improvement on the minimization of the distance is applied (see [8]). Once the vertex position is defined, only the secondary vertices inside a given fiducial volume are kept (in Fig.3.2, the dotted lines). Finally, the V^0 finding procedure checks whether the momentum of the V^0 candidate (calculated as the sum of the track momenta extrapolated to the position of the DCA) accurately points back to the primary vertex applying a cut on the cosine of the pointing angle ($\cos\Theta_p$).

3.3 Data analysis

3.3.1 Event and track selection

In this section the event and track selection will be described. We know, in fact, that not all the events are used for analysis. The primary vertex has been reconstructed using either Silicon Pixel Detector or global tracks. The events selected are those with a distance between the position of the primary vertex and the geometrical center of the apparatus along the beam axis less than 10 cm. Events with primary vertex outside the range $|z| > 10$ cm are discarded. In this way, it has been possible to minimize acceptance and efficiency effects for those tracks at the edge of the TPC detection volume. No conditions are applied on the x and y position of the vertex. The total number of events used for the study of the PID efficiency for protons (antiprotons) and pions consists of a sample of about 200 M events minimum bias pp collisions at $\sqrt{s} = 7$ TeV, corresponding to period LHC10b, LHC10c and LHC10d. The data were collected in 2010 and the reconstruction has been done with the ALICE offline framework, AliRoot [62].

Several quality criteria for the track selection are defined. Each track is required to have been reconstructed in the Time Projection Chamber in the initial step of tracking (from the primary vertex to the last point in the TPC) and then fully refitted in the last step (the back-propagation to the primary vertex). In the analysis, it is also required that each track has at least 110 TPC clusters. No specific condition on the number of ITS hits is requested for the track daughter of the weakly decaying particles, since the decay point (hence the number of the ITS layers crossed by the daughters) depends on the lifetime and on the momentum of the particle itself (Λ, $\bar{\Lambda}$

and K_S^0). Other quality criteria are applied for selecting the daughter tracks, based on the ones defined in [8][1] and optimized for efficiency. The track selection criteria are summarized in the following requirements.
Common selections:

- Detectors required for track rec./fit: ITS, TPC
- Number of TPC clusters > 110 (maximum number of the TPC is 159)

Primary track selections:

- χ^2 per cluster < 4
- DCA to primary vertex (r,z) < (0.5, 3.0) cm
- Number of SPD clusters $\geq$ 1 (maximum number for the SPD is 2)

The Λ, $\bar{\Lambda}$ and K_S^0 have been identified by applying selections on the characteristic of their daughter tracks and using their weak decay topologies. For the evaluation of the PID efficiency the used cuts have been optimized to select clean samples of V^0 candidates. As described before, the measurement of the V^0 candidate is based on the reconstruction of the secondary vertex (V^0) associated to their weak decay. In the present analysis, the V^0 has been accepted only if the DCA between the track pairs is smaller than 0.5 cm. If the V^0 vertex position (the mean point on the line connecting the points of closest approach between the two tracks) is located inside the fiducial volume between the radius of 0.2 cm and 100 cm, the V^0 candidates are kept. A cut on the pointing angle ($\theta_p > 0.999$) allows to check if the V^0 points back to the primary vertex (this cut rejects about 23% of the V^0 candidates).

The secondary vertex selection criteria used in the analysis are summarized in the following requirements:

[1]As discussed in the chapter 2, track reconstruction in ALICE is based on the Kalman filter approach.

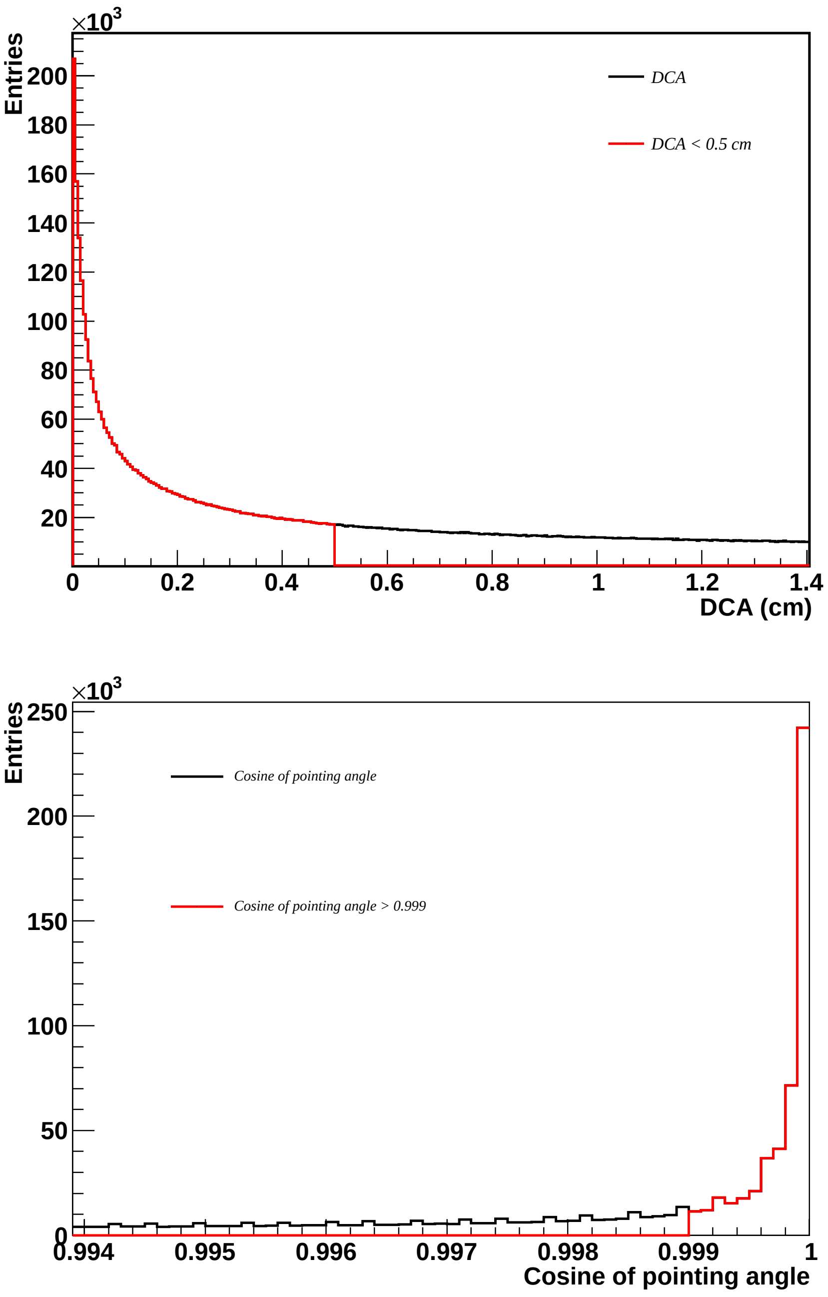

Figure 3.3: *Distribution of DCA between the V^0 daughter tracks (upper panel); distribution of cosine of pointing angle (lower panel).*

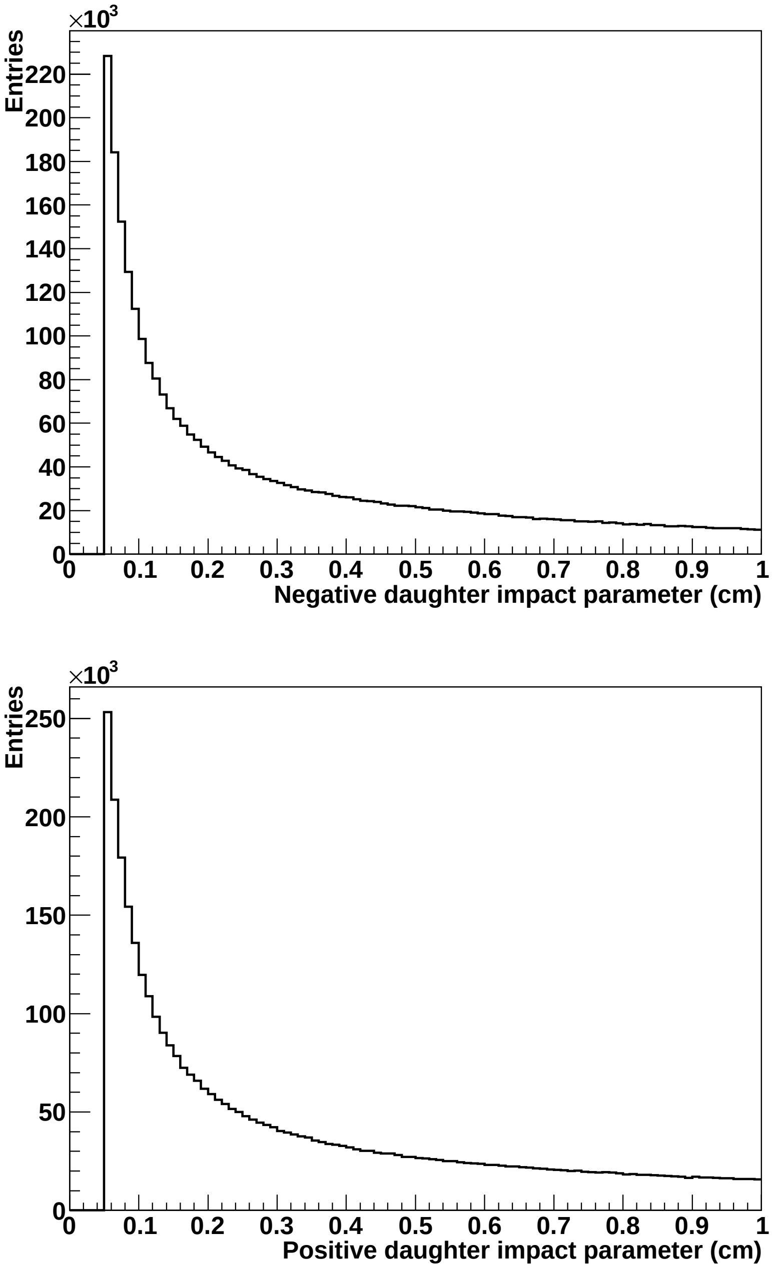

Figure 3.4: *Distribution of impact parameter for negative (upper panel) and positive daughter (lower panel).*

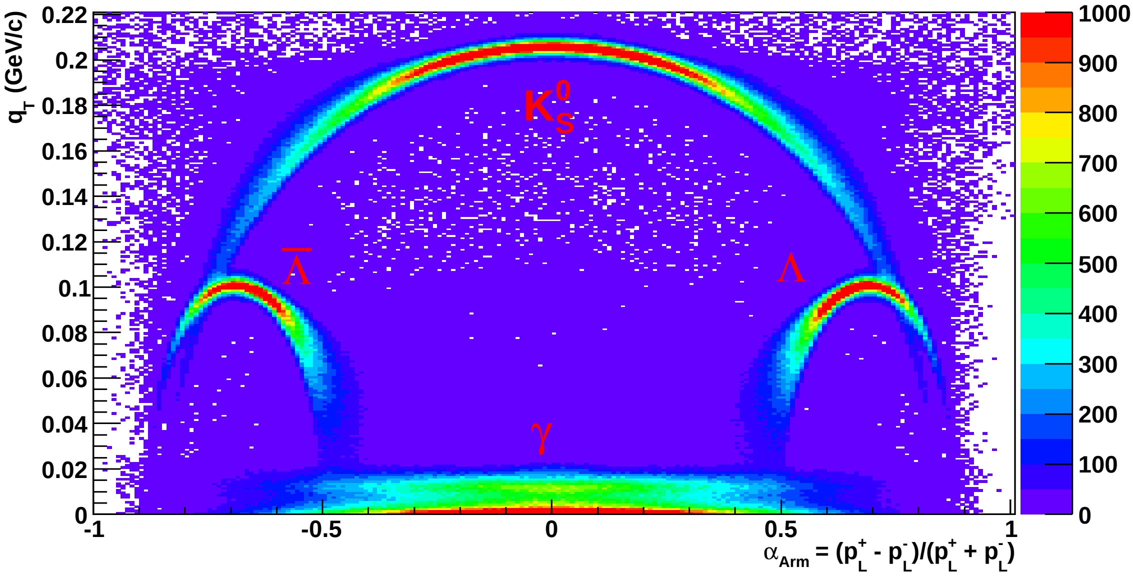

Figure 3.5: *Armenteros-Podolanski distribution for V^0 candidates in the ALICE-HMPID acceptance is plotted. The transverse momentum q_T as a function of the α_{Arm} in the V^0 coordinate system for the reconstructed V^0 candidates in the HMPID geometrical acceptance.*

- Minimum transverse decays radius = 0.2 cm;
- Maximum transverse decays radius = 100 cm;
- Impact parameters of V^0 daughter track to primary vertex > 0.05 cm;
- DCA between V^0 daughter tracks < 0.5 cm;
- Cosine of pointing angle > 0.999;

Fig.3.3 and Fig.3.4 show the DCA distribution for V^0 daughter tracks (the red line corresponds to the distribution for DCA < 0.5 cm), the cosine of pointing angle distribution (before and after the cut), and the impact parameter for positive and negative daughters.

Once the event and track selection is terminated, the invariant mass M of each candidate can then be calculated under the Λ, $\bar{\Lambda}$ and K^0_S hypotheses using the following equation, which is derived from energy and momentum conservation considerations:

$$M = \sqrt{m_1^2 + m_2^2 + 2(E_1 E_2 - \vec{p_1} \cdot \vec{p_2})} \tag{3.4}$$

Here, m_i is the rest mass, $\vec{p_i}$ is the momentum and E_i is the energy of the daughter particle. The energy is calculated from $E = \sqrt{m^2 + p^2}$.

By inserting the three possible combinations of the proton and pion masses for m_1 and m_2, one obtains the three possible invariant masses for each candidate:

$$M_\Lambda = \sqrt{m_p^2 + m_{\pi^-}^2 + 2(E_p E_{\pi^-} - \vec{p_p} \cdot \vec{p_{\pi^-}})} \tag{3.5}$$

$$M_{\bar{\Lambda}} = \sqrt{m_{\bar{p}}^2 + m_{\pi^+}^2 + 2(E_{\bar{p}} E_{\pi^+} - \vec{p_{\bar{p}}} \cdot \vec{p_{\pi^+}})} \tag{3.6}$$

$$M_{K^0_S} = \sqrt{m_{\pi^+}^2 + m_{\pi^-}^2 + 2(E_{\pi^+} E_{\pi^-} - \vec{p_{\pi^+}} \cdot \vec{p_{\pi^-}})} \tag{3.7}$$

.

3.3.2 The Armenteros-Podolanski plot

The usual visual tool for distinguishing ambiguous decays for Λ, $\bar{\Lambda}$ and K^0_S is the Armenteros-Podolanski [90] plot formed by plotting two kinematic variables against one another.

$$q_T = psin\theta \tag{3.8}$$

defined as the transverse momentum component of the daughter to the momentum vector of the parent particle (see Appendix C for more details). q_T is identical for each daughter particle due to the conservation of momentum. The other kinematic variable, α_{Arm}, is defined as

$$\alpha_{Arm} = \frac{q_L^+ - q_L^-}{q_L^+ + q_L^-} \tag{3.9}$$

where q_L^+ and q_L^- are the longitudinal momentum components of the $\pm ve$ particle respect with to the parent momentum, measured in the laboratory frame. The α_{Arm} variable measures the momentum asymmetry in the decay. In the Λ and $\bar{\Lambda}$ decays the proton and anti-proton carries most (about 80 %) of the momentum of the V^0 candidates, this means that the points of allowed values for these decays have centers shifted away from zero. The K_S^0 decays has products of identical mass so the pions distribution is symmetric around an α_{Arm} of zero. The resulting Armenteros-Podolanski distribution is shown in the Fig.3.5. Three clear half ellipses (bands) of Λ, $\bar{\Lambda}$ and K_S^0 are shown and, in the lower part, the reconstructed V^0 candidates coming from the γ in conversion e^+ e^- due to detector material are clearly visible. They are located in the low q_T region.

In the Armenteros-Podolanski distribution, regions where the Λ, $\bar{\Lambda}$ and K_S^0 bands are clean have been selected. In the selection, contamination between species (overlapped area) has been minimized. The corresponding selected regions for the Λ, $\bar{\Lambda}$ and K_S^0 (see Fig.3.6) are:

- for Λ selection:

$$\begin{aligned} 0.45 &< \alpha_{Arm} < 0.66 \\ 0.04 &< q_T < 0.12\ GeV/c \end{aligned}$$

- for $\bar{\Lambda}$ selection:

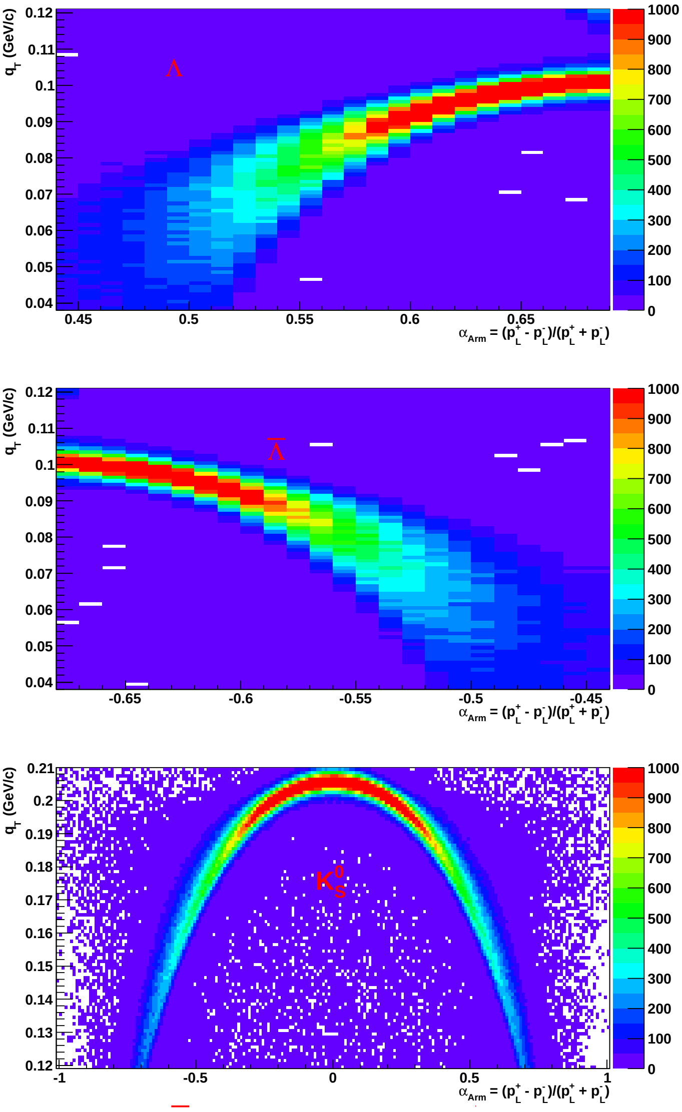

Figure 3.6: *From the Armenteros-Podolanski distribution for V^0 candidates the three regions for selecting Λ (upper panel), $\bar{\Lambda}$ (middle panel) and K_S^0 (lower panel).*

$$-0.66 < \alpha_{Arm} < -0.45$$
$$0.04 < q_T < 0.12\ GeV/c$$

- for K^0_S selection:

$$0.12 < q_T < 0.21\ GeV/c$$

The selected regions for $\bar{\Lambda}$ and Λ are symmetric. To further clean the samples, the following mass windows are applied to reject the tails on the invariant mass distributions:

$$1.11 < m_\Lambda < 1.12\ GeV/c^2$$
$$1.11 < m_{\bar{\Lambda}} < 1.12\ GeV/c^2$$
$$0.48 < m_{K^0_S} < 0.51\ GeV/c^2$$

After this selection, we kept only V^0 daughter that released a signal in the HMPID detector. This means, we selected only V^0 candidates in the HMPID acceptance. The final invariant mass distributions for Λ, $\bar{\Lambda}$ and K^0_S, after the topological cuts, in the previous selected regions of the Armenteros-Podolansky plot and in the HMPID acceptance are shown in Fig.3.7.

3.3.3 Background estimate

For minimum bias pp collisions, the signals for the Λ, $\bar{\Lambda}$ and K^0_S are clearly distinguishable from the combinatorial background. In Fig.3.8, the Λ invariant mass as a function of different cuts is shown. The black line represents the invariant mass

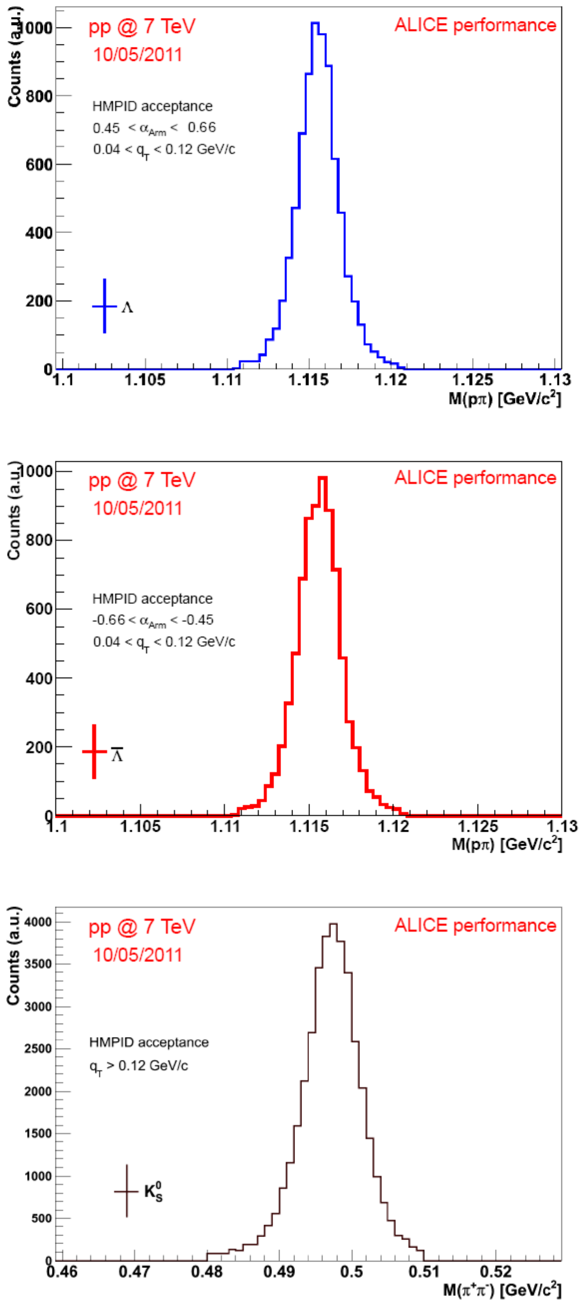

Figure 3.7: *Invariant mass distribution for* Λ, $\bar{\Lambda}$ *and* K^0_S *obtained selecting specific regions in the Armenteros-Podolanski plot. A useful cut on the invariant mass distribution to reject the tails has been applied.*

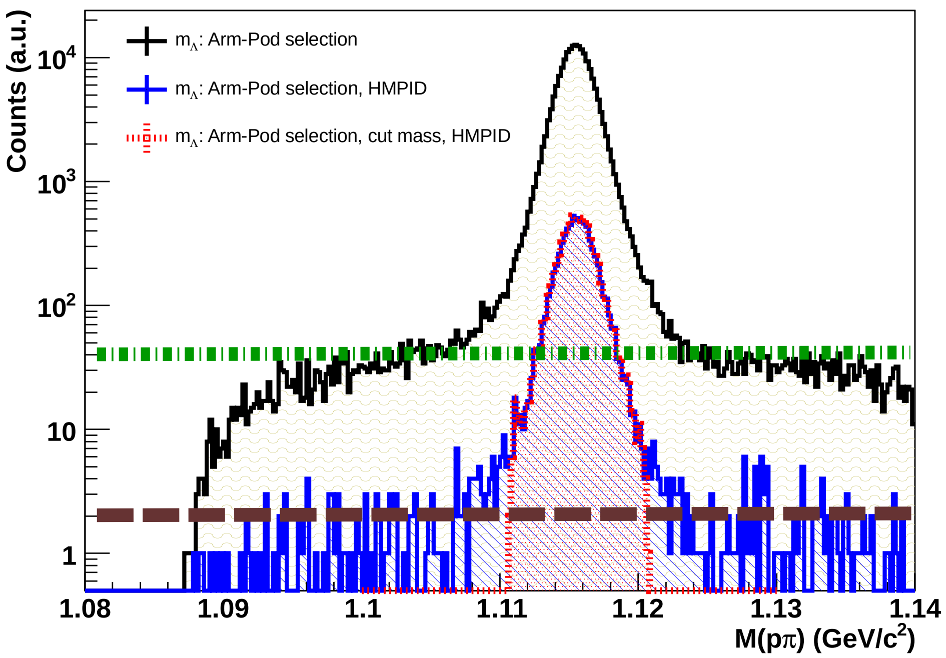

Figure 3.8: Λ *invariant mass distribution. The black line represents the invariant mass distribution obtained from the* V^0 *candidate kept after track selection and the selected Armenteros-Podolanski area. The blue curves represent the invariant mass for the* V^0 *candidate with a positive daughter in the HMPID acceptance. On the red line a cut on* Λ *mass has been applied.*

distribution obtained from the V^0 candidates kept after track selection and inside the selected Armenteros-Podolanski area. The green line helps to evaluate (qualitative evaluation) the ratio between background and signal. The value is about 0.3 %. The blue curve represents the invariant mass for the V^0 candidate with a positive daughter in the HMPID acceptance. The estimate of B/S ratio is about 0.25 %.

So, it is fair to assume that the background in the selected samples is negligible. The tails of the blue mass distribution have been rejected with proper mass cut (red line distribution) to further clean the sample. Similar results for the $\bar{\Lambda}$ and K^0_S

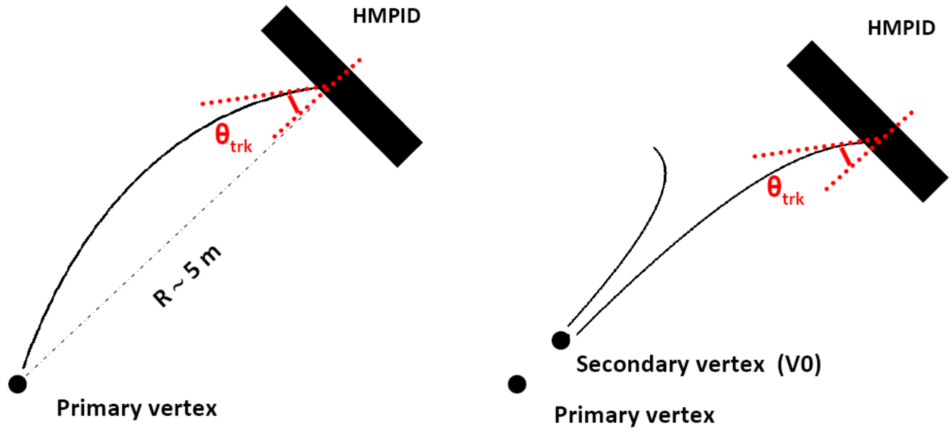

Figure 3.9: *A draw representing a primary track (left) to the HMPID and a secondary track (right) coming from V^0 vertex. The daughter of the V^0 candidate shows similar behavior to the primary track due to the short length decays (few cm) of the V^0 candidates and because the HMPID is located at $\sim$ 5 m from the primary vertex.*

background estimate have been obtained.

3.3.4 Check on the impact angle from the V^0 daughters

Fig.3.9 shows an example of a track coming from the primary vertex (left) and crossing the HMPID chambers (xy view) and a track coming from a typical V^0 vertex (right). In this section we want to explain why is possible to use secondary tracks (from V^0 vertices) to evaluate the PID efficiency that it will be used to correct the hadron spectra (evaluated trough the selection of primary tracks). First of all, we remark that the lifetime of the strange particles is short, which means that the particles decay after a few centimeters from the primary vertex. Since the HMPID detector is located at $\sim 5\ m$ from the primary vertex, the daughters coming from V^0 candidates show a very similar behavior respect to primary tracks.

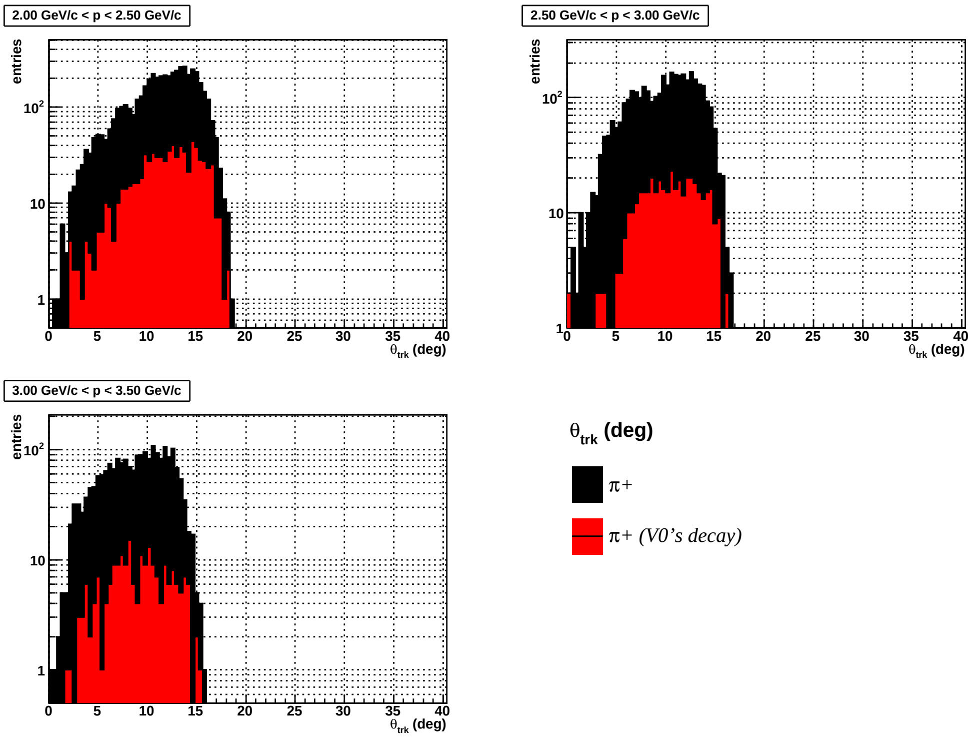

Figure 3.10: *The comparison between θ_{trk} for pions coming from V^0 and for primary tracks. To select pions coming from primary tracks a 2-σ cut has been applied.*

In addition, an experimental check on the distribution of the impact angle for the tracks coming from the V^0 and from primary tracks is described. Protons and pions coming from V^0 candidates are generated from the secondary vertex in a fiducial region between 0.2 cm up to 100 cm, as described in the previous paragraph, contrary to the primary tracks. So, we want to show that the inclination angles (θ_{trk}) of that tracks generated from the primary vertex is compatible with secondary tracks (generated from secondary vertex) as shown in Fig.3.9.

Before to evaluate the PID efficiency, it is useful to check and clarify this point. If the impact angles of the V^0 daughters are systematically shifted, the evaluated PID efficiency using the V^0 candidate, cannot be used for the primary tracks analysis

(spectra evaluation).
For this reason, two different data sets have been analyzed:

- a sample of primary tracks in the HMPID acceptance (LHC10b, LHC10c, LHC10d);

- a sample of V^0 daughters in the HMPID acceptance (LHC10b, LHC10c, LHC10d).

To select primary pions (or protons), a 2-σ cut has been applied in the Cherenkov angle distribution (in slices of track momentum) and the corresponding impact angle (θ_{trk}) has been plotted in Fig. 3.10. The figure shows the θ_{trk} distribution in three momentum track ranges for primary pions (the black area). The pion θ_{trk} coming from the K^0_S decays is shown by the red area. The θ_{trk} values cover the same range, showing good agreement. No shift, nor particular effect, in the angles has been noticed.
The comparison has been done also for protons coming from Λs and the results show again good agreement.

3.4 PID efficiency

We define the PID efficiency as the ratio between the number of particles identified by the HMPID detector and the generated particles in the HMPID acceptance.
In particular, the PID efficiency for the V^0 decays is defined:

$$Efficiency_{PID} = \frac{yield_{Cherenkov\ Angle}}{yield_{Invariant\ Mass}} \tag{3.10}$$

where we denote by $yield_{Invariant\ Mass}$ the number of V^0 candidates (mothers) with a daughter in the HMPID acceptance extracted from fitting procedure and by $yield_{Cherenkov\ Angle}$ the number of the corresponding daughters (protons/pions)

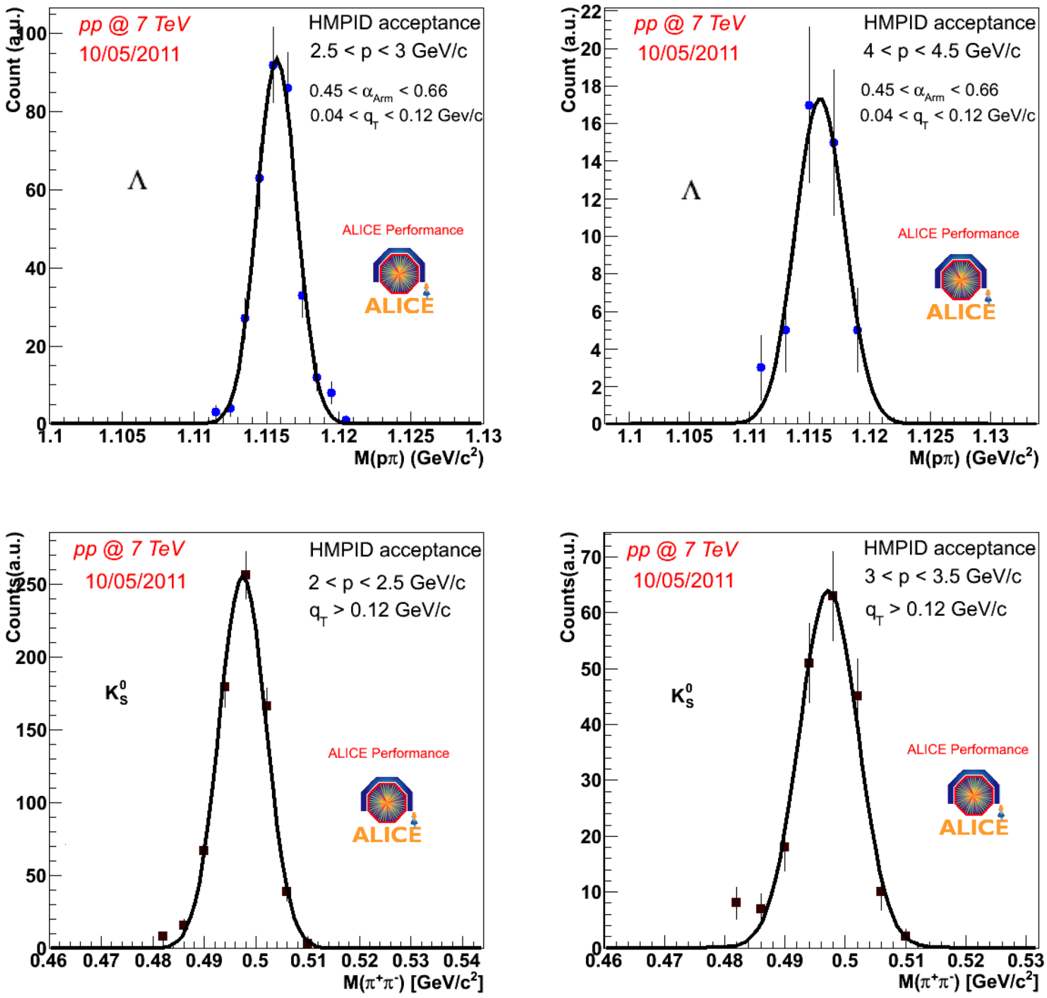

Figure 3.11: *Examples of invariant mass distribution for* Λ *with proton daughters detected by the HMPID in momentum range* $2.5 < p < 3$ *GeV/c and* $4 < p < 4.5$ *GeV/c for* Λ *(upper panel). In lower panel, two examples of* K^0_S *invariant mass (*$2 < p < 2.5$ *GeV/c and* $3 < p < 3.5$ *GeV/c) are shown. Gaussian fit has been performed and the yield has been counted (to evaluate the PID efficiency, only the entries under the Gaussian fit are counted). In the plot the selected regions in the Armenteros-Podolanski plot and the momentum track range have been included.*

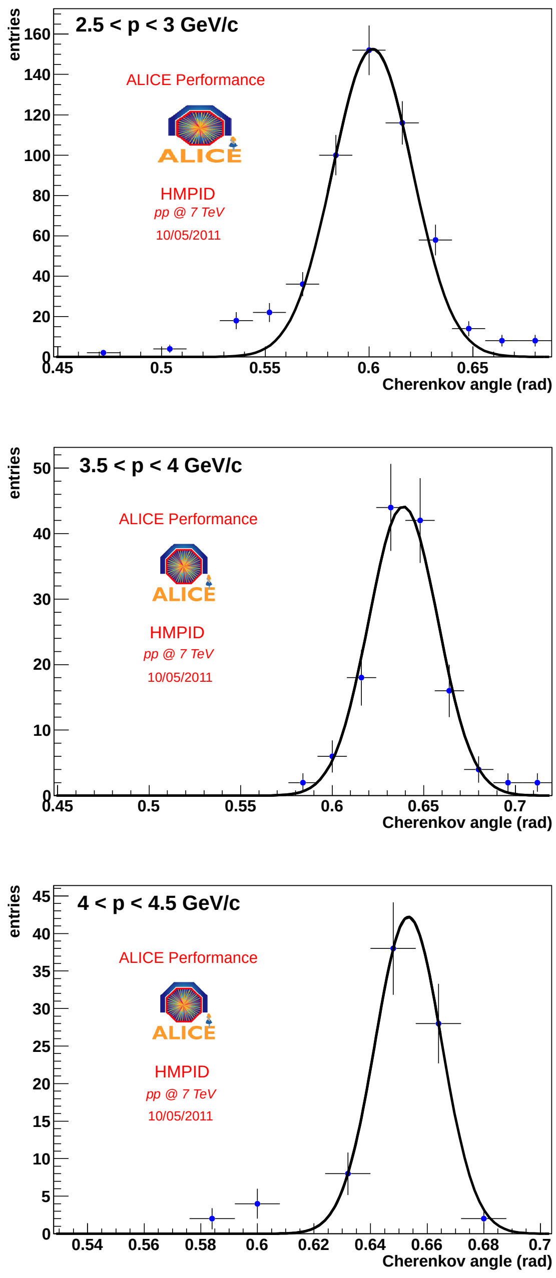

Figure 3.12: *Examples of Cherenkov angle distributions for protons and antiprotons coming from* Λ *and* $\bar{\Lambda}$*. The tails are due to the background noise.*

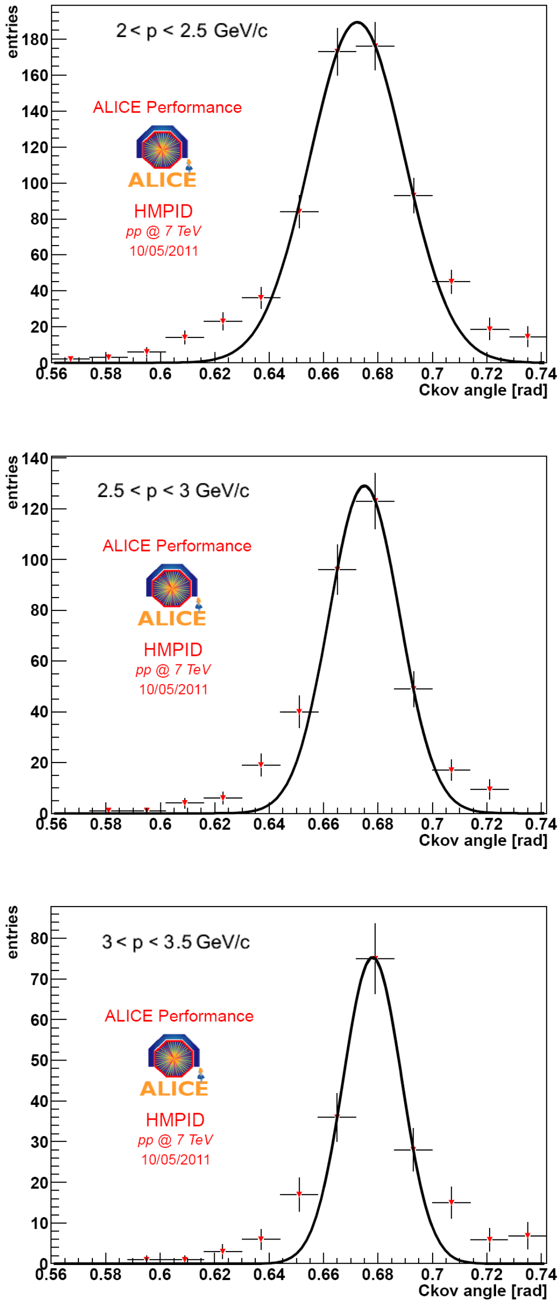

Figure 3.13: *Examples of Cherenkov angle distributions for pions from* K^0_S. *The tails are due to the background noise.*

reconstructed by the pattern recognition algorithm from fitting procedure [2]. The Gaussian fitting procedure in each p-bin for the invariant masses has been performed as shown in Fig.3.11: some example of Λ and K^0_S invariant masses in different momentum ranges are shown (similar results for $\bar{\Lambda}$). Only 5 momentum sub-ranges for pions and 8 for protons are set due to the low statistics available (note, as stressed frequently in this thesis, the HMPID acceptance is only 5% of that of the TPC). In Fig.3.12 and Fig.3.13, some examples are shown of Cherenkov angle distributions in relevant momentum p-bins for the proton coming from Λ and for pions coming from K^0_S. The Gaussian fit has been performed constraining the mean of the theoretical Cherenkov angle and allowing the sigma to vary by 20 %.
The tails of the θ_{Ckov} distributions, as shown in the Fig.3.12, can be explained taking into account different effects, for example the electronic noise that fires pads randomly and the dead zones between HMPID chambers. An estimate shows that about 0.2 % of the pads are fired due to the electronic noise. The Hough Transform Method, HTM, (as described in the previous chapter) selects some fired pads due to the noise in the pattern recognition, and it reconstructs a pattern ring giving a wrong angle value.

From the fit parameters, it has been possible to verify the agreement between the mean Cherenkov angle and the theoretical curves (solid lines) describing the Cherenkov effect for protons and pions (as shown in Fig.3.14). The sigma for each gaussian has been quoted as error bar in the plots. The agreement between the experimental points and the theoretical lines is quite good.

[2] Note that there isn't ambiguity in the protons/pions identification for the V^0 candidates. Let's consider a sample of Λ. Let's suppose that for each Λ both daughters (proton and pion) cross the HMPID chambers (it isn't the real case, in fact, most of pions don't carry enough momentum of the Λ to cross the chambers of the detector). To evaluate the PID efficiency for protons is necessary to select, in the code, the daughters with positive sign (that corresponds to protons). The track sign is provided from the tracking system and stored at level of Event Summary Data (ESD) as explained in the Chapter 2. Hence, we are always sure, to select only protons (not pions) if we want to evaluate the PID efficiency for protons.

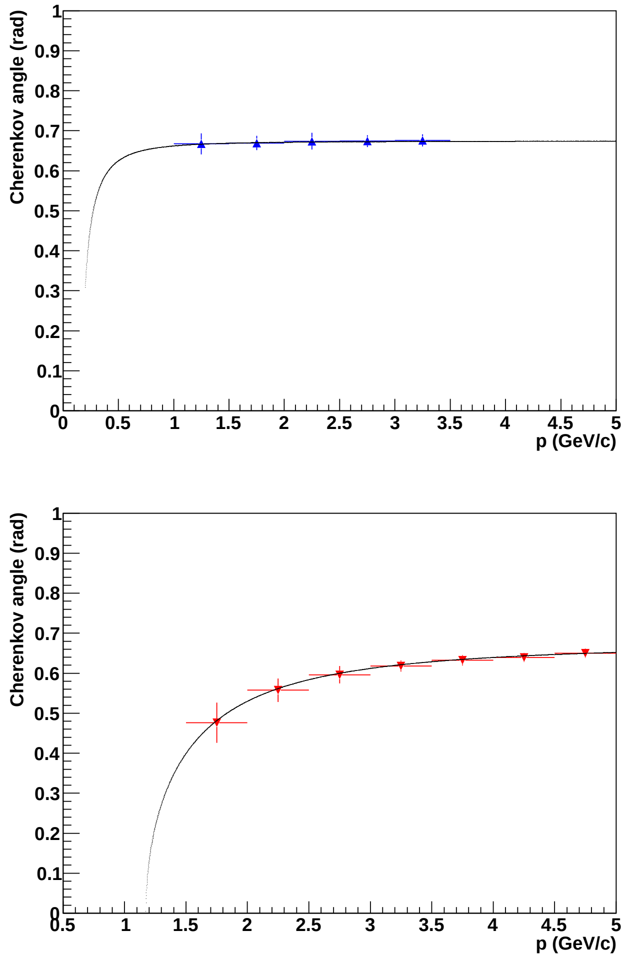

Figure 3.14: *Upper: Mean Cherenkov angle as a function of track momentum for pions coming from K_S^0. The solid line represents the theoretical curves. The points are obtained from fitting procedure. Lower: Mean Cherenkov angle as a function of track momentum for protons coming from Λ.*

In Fig.3.15 the final PID efficiency for pions (1< p < 3.5 GeV/c) and for protons (1< p < 5 GeV/c) is shown. The capability to identify protons rises up to 0.9 (90 %) in the momentum range between 3.5 up to 5 GeV/c and for pions between 2.5 and 3.5 GeV/c. At lower momenta, the Cherenkov rings are made of a smaller number of photons with respect to the tracks at higher momentum and the electronic noise affects the patter reconstruction giving more frequently a wrong reconstructed Cherenkov angle. Also, the dead zones between the HMPID chambers can affect the pattern reconstruction. Note that the HMPID detector identifies charged hadrons regardless of the particle sign. Anyway, in the early stage of the analysis, the efficiency has been calculated for protons, antiprotons, π^+ and π^- independently. The obtained results have been compared showing an excellent agreement and the efficiency presented in the Fig.3.15 is evaluated adding together positive and negative particles.

3.5 PID efficiency: MC - data comparison

The PID efficiency for protons and pions using data has been described. However the evaluation of the PID efficiency for kaons still remains an open question. For this reason the PID efficiency for the three species (pion, kaon and proton) has been evaluated using Monte Carlo simulation and the comparison with the results obtained in the previous section for pions and protons (antiprotons) is carried out. We define the MC PID Efficiency as:

$$Eff_{MC-PID} = \frac{(dN/dp_t)_{reconstructed}}{(dN/dp_t)_{generated}} \tag{3.11}$$

where the numerator denotes the number of the reconstructed tracks in HMPID acceptance with a Cherenkov ring reconstructed, while the denominator denotes the number of the total tracks in the HMPID acceptance. Clearly, the Eq.3.11 is completely equivalent to the Eq.3.10.

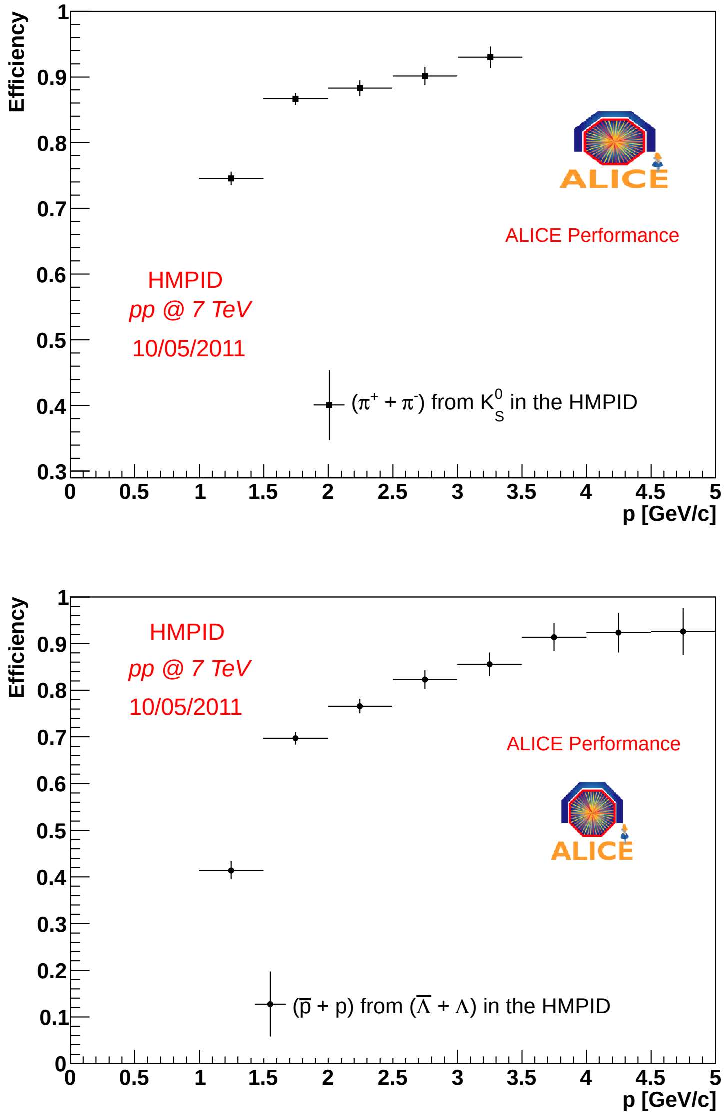

Figure 3.15: *The final PID efficiency for pions (1 < p < 3.5 GeV/c) and protons (1 < p < 5 GeV/c) obtained using the* V^0 *candidates.*

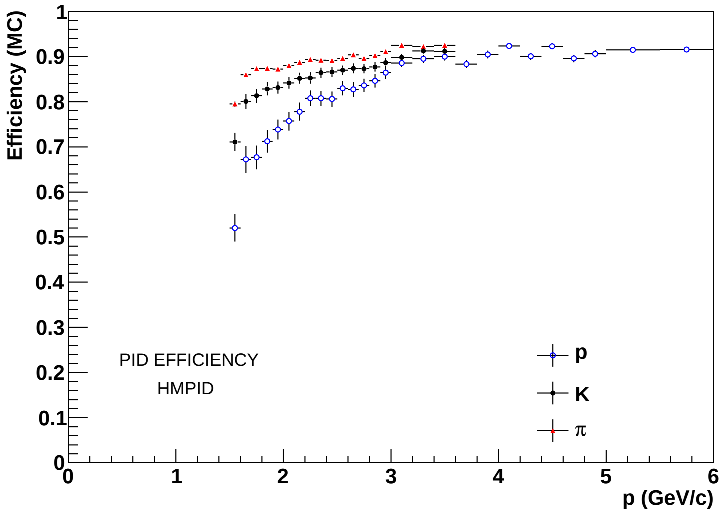

Figure 3.16: *PID efficiency for pions, kaons and protons from Monte-Carlo simulation.*

Note that, the $(dN/dp_t)_{reconstructed}$ are evaluated from the fitting procedure using a Gaussian distribution.

In Fig.3.16 the MC PID efficiency for pions, kaons and protons is shown. The comparison between MC and data is carried out and is shown in Fig.3.17, in the upper and lower panel for protons and pions respectively. The agreement between the PID efficiency (pions and protons) retrieved from V^0 decays and MC is quite good. The result is particulary satisfactory because it comes from two different techniques. The fluctuations in the MC curves can be explained by to the low statistic available. We can conclude that the MC PID efficiency for kaons can be used for spectra analysis. We remark that PID efficiency is not dependent on the charge sign of the particles: the PID response is equal to both positive and negative particles.

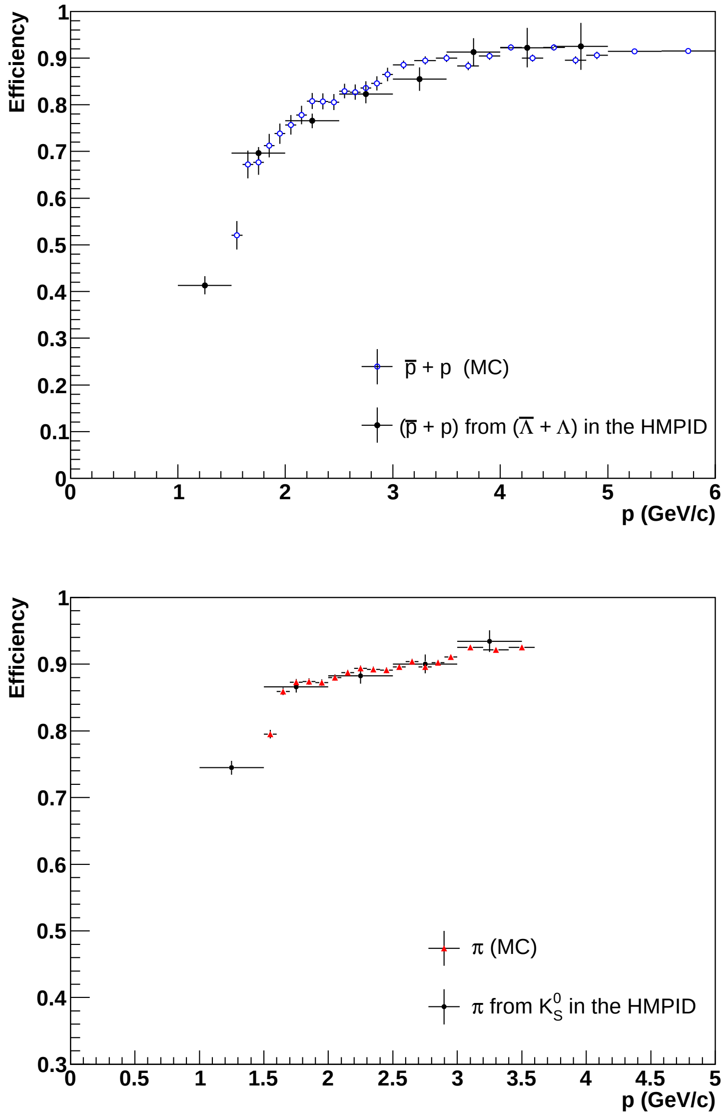

Figure 3.17: *MC - data comparison for protons (upper panel) and for pions (lower panel).*

3.6 C_6F_{14} refractive index measurement from identified protons

An additional topic (concerning the HMPID performance) that can be addressed through the V^0's decays, is the measurement of the radiator refractive index. This measurement plays an important role in the HMPID analysis, for example in the measurement of the raw yields where the precise knowledge of refractive index (and then of the Cherenkov angle) in the fitting procedure can help to reduce the error in the raw yields estimation (as explained in chapter 4).
Starting from identified protons coming from the Λ, the C_6F_{14} refractive index of the HMPID radiator has been measured (Figure 3.18). The average value of the $n_{C_6F_{14}}$ has been deduced using the well-known Cherenkov equation:

$$cos\theta_C = 1/\beta \cdot n_{C_6F_{14}} \tag{3.12}$$

The restricted sample of protons coming from Λ described in the previous sections has been used for this measurement.

To clean further the sample the following two cuts on the Λ invariant mass and on the track momentum are applied:

- $1.114 < M_\Lambda < 1.118$ GeV/c;
- $p > 3$ GeV/c;

The last cut was necessary to select only protons in saturation (rings with the maximum number of photons and PID efficiency of about 90%). The Cherenkov angle has been retrieved from the detector response, while the momentum value is obtained from the tracking system. The $n_{C_6F_{14}}$ value obtained

$$n_{C_6F_{14}} = 1.289 \pm 0.014 \tag{3.13}$$

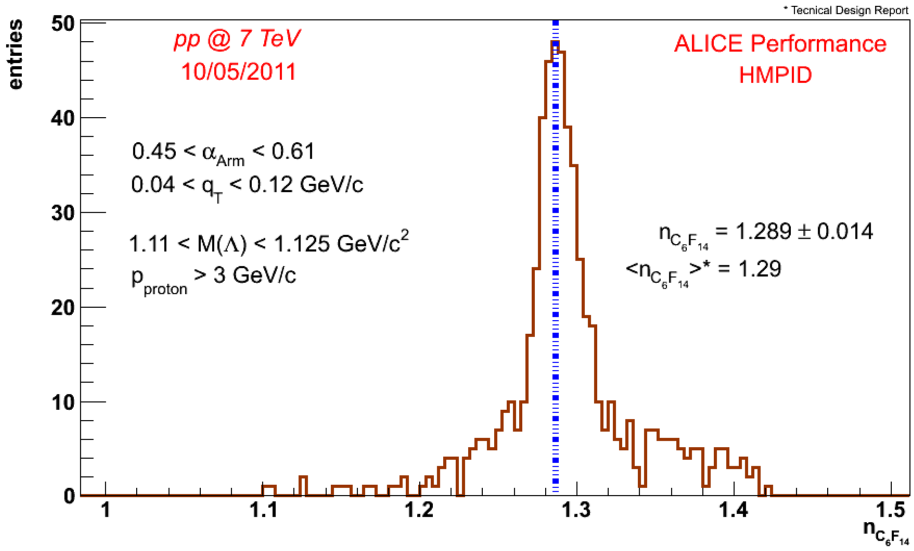

Figure 3.18: *C_6F_{14} refractive index measurement of the HMPID radiator from identified protons.*

is in excellent agreement with the average value quoted in the HMPID Technical Design Report[71, 91] and obtained by optical measurement.

3.7 Summary of Chapter 3

The HMPID detector can identify the daughters of the V^0 candidates. A measurement of the experimental PID efficiency has been performed for protons and pions in pp collisions at $\sqrt{s}$ = 7 TeV collected during 2010. As explained in the previous chapter, due to the 0.5 T magnetic field and a significant material budget before the HMPID, the Cherenkov angle measurement is affected by several systematic error sources especially at low momenta (below 2 GeV/c). In spite of these, the High Momentum Particle Identification detector shows very good PID performances. In addition, the comparison between the results obtained from the V^0 study and from Monte-Carlo simulation shows an excellent agreement. In the last part of the chapter, an experimental measurement of refractive index using the clean sample of protons coming from Λ has been presented. The results is in good agreement with the optical measurements.

The results of this analysis was presented during the Poster Session of the "Quark Matter 2011" (23 - 28 May 2011, Annecy - France).

Chapter 4

First HMPID ALICE p-p physics results at $\sqrt{s} = 7$ TeV

4.1 Introduction

Proton-proton data represents a fundamental benchmark for the understanding of heavy-ion data. In this chapter, the analysis done using the HMPID detector for the evaluation of the transverse momentum spectra and ratios of identified particles at mid-rapidity in pp collisions will be described. The data are those collected during 2010 at $\sqrt{s} = 7$ TeV. The analysis procedure can be subdivided in 4 main steps: the description of the sample selection (event and track selection), the yield extraction, the evaluation of the efficiency and the systematic uncertainties estimate. The last section of this chapter is devoted to the presentation of the preliminary results obtained: the corrected spectra are evaluated in the momentum range $1.5 < p_t < 3.4$ GeV/c for pions and kaons and $1.5 < p_t < 3.4$ GeV/c for protons; the π^-/π^+, K^-/K^+ and $\bar{p}/p$ ratios are evaluated in the same momentum ranges.

4.2 Sample selection

The focus of this chapter is on the transverse momentum distribution of identified charged hadrons. The data used for this analysis were collected during the 2010, with magnetic field of 0.5 T, with pp collisions at $\sqrt{s}$= 7 TeV. The typical bunch intensity was 1.5×10^{10} protons resulting in a luminosity L $\sim 10^{27}$ $cm^{-2}s^{-1}$. There was only one bunch per beam colliding at the ALICE interaction point. The analysis is based on about 200 M inelastic pp collisions (LHC10b, LHC10c and LHC10d period). Two levels of selection are performed on the data sample: event selection and track selection.

4.2.1 Event selection

The event selection starts with the online trigger selection that requires a signal in either the VZERO counter or at least one hit in either of the SPD layers. The selection was improved offline with recomputed trigger input quantities using the time average over all VZERO hits and a suppression of noisy channels. The contamination from beam-induced background is rejected offline using the timing information of the VZERO and by cutting on the correlation between the number of cluster and track segments - tracklets - in the SPD detector. A tracklet is defined by a hit combination, one hit in the inner and one in the outer SPD layer, pointing to the reconstructed vertex. The z-vertex range has been restricted to $|z| < 10$ cm (Fig.4.1). The vertex reconstruction efficiency is calculated via Monte Carlo and is about 96 % for events with one reconstructed track and approaches unity for events with more than two tracks.

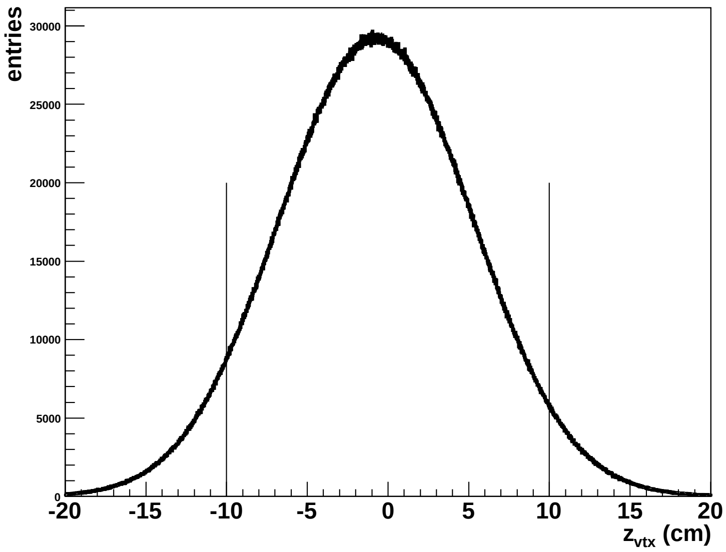

Figure 4.1: *Primary vertex distribution, z_{vtx}, along the beam axis, for the analyzed events. Selected events are required to have a reconstructed primary vertex with $|z| <$ 10 cm.*

4.2.2 Track selection

Tracks reconstructed in the TPC are used. The TPC has full acceptance for tracks with $|\eta| < 0.9$. To ensure high tracking efficiency and dE/dx resolution, while keeping the contamination from secondaries and fakes low, tracks are required to have at least 70 clusters, and a χ^2 of the momentum fit smaller than 4 per cluster. Since each cluster in the TPC provides two degrees of freedom and the number of parameters of the track fit is much smaller than the number of clusters, the χ^2 cut is approximately 2 per degree of freedom. In addition, at least two clusters in the ITS must be associated to the track, out of which at least one is from the SPD.

Tracks are further rejected based on their distance-of-closest approach (DCA) to the reconstructed event vertex. The DCA parameter is the distance of closest approach of a track to the interaction vertex. It can be projected on the transverse plane and on the z-direction (beam direction). Both components allow us to distinguish between primary particles and those not originated from the primary vertex. This parameter is useful for excluding the secondary particles from the data sample. The cut is implemented as a function of p_t taking into account the p_t dependence of the impact parameter resolution. These criteria are tuned to select primary charged particles with high efficiency while minimizing the contributions from weak decays, conversions and secondary hadronic interactions in the detector material. Tracks reconstructed in the TPC are extrapolated to the sensitive layer of the TOF and a corresponding signal is searched for. The channel with the centre closest to the track extrapolation point is selected if the distance is less than 10 cm. This rather weak criterion results in a high matching efficiency while keeping the fraction of wrongly associated tracks below 1% in the low-density environment present in pp collisions.

4.3 Yield extraction

4.3.1 Cherenkov angle as a function of track momentum

After the event and track selection, the yield extraction starts by plotting the Cherenkov angle distribution as a function of the track momentum (for the tracks crossing the HMPID). For a charged particle with mass m, energy E, momentum p, the Cherenkov relation can be written

$$cos\theta_{Ckov} = \frac{1}{n\beta} \tag{4.1}$$

where n is the C_6F_{14} refractive index of the HMPID radiators. Hence,

$$\theta_{Ckov} = arcos\left(\frac{1}{(np/E)}\right) = arcos\left(\frac{\sqrt{(p^2+m^2)}}{np}\right) \tag{4.2}$$

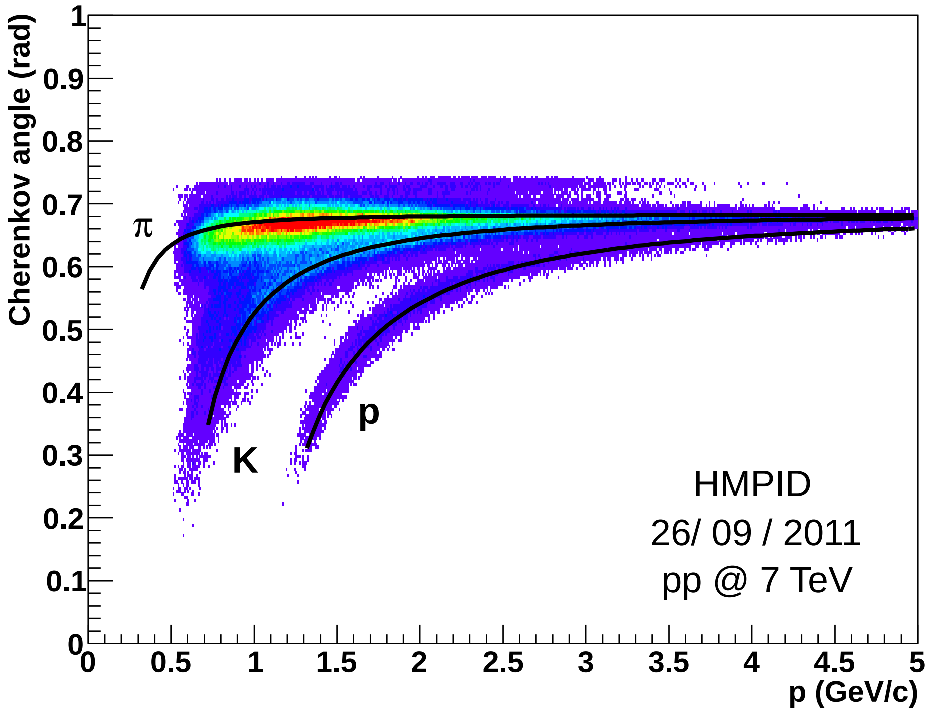

Figure 4.2: *The Cherenkov angle distribution as a function of the track momentum in pp collisions at* $\sqrt{s}$ *= 7 TeV. The Cherenkov bands (pions, kaons and protons) are clearly visible and follow the theoretical expectations (black solid lines) for nominal* C_6F_{14} *refractive index. The plot has been obtained selecting only primary tracks and using specific HMPID cuts.*

where p have to satisfy the $|cos\theta_C| \leq 1$ condition. It means:

$$p \geq \frac{m}{\sqrt{(n^2 - 1)}}; \tag{4.3}$$

The π, K and p particles, generated in the collisions produce three curves as shown in Fig.4.2. Note that tracks with p < 500 MeV/c cannot cross the HMPID chambers because are bent by the magnetic field. The contamination from electrons and muons in the pions, kaons and protons is negligible. To clean the tracks sample two cuts are applied: the cut on the MIP charge discrimination and the matching selection.

The cut on the MIP charge discrimination is needed to discriminate between a photon and a given MIP cluster. $Q_{MIP} > 150$ ADC allows to select only MIP clusters, rejecting photons clusters.
The distance between the extrapolated track point in the HMPID photocathode plane of a given chamber and the coordinate of the nearest centroid, of a charge compatible with the MIP cluster, is required to be smaller than a given limit: $d < d_{MIN} = 0.7$ cm (the matching selection). This cut reduces the probability of the mismatching of a track with the MIP cluster of another particle.
In the following sections, it will be shown how the matching selection affects the analyzed sample. The evaluation of the corresponding correction factor will be discussed.

If the mass values for each particle are inserted in the eq. 4.2, three theoretical curves (pion, kaon, proton) are obtained and can be overlapped to the experimental bands. The agreement between experimental and theoretical curves is quite good as shown in Fig.4.2. The plot plays a fundamental role because it represents the first step for PID and allows pion, kaon and proton spectra and its corresponding ratio to be measured.

4.3.2 Fitting procedure: general remarks

The extraction of the raw yield is strongly related to three factors:

- the corrected use of a fitting procedure,
- the understanding of the detector response,
- the statistics available.

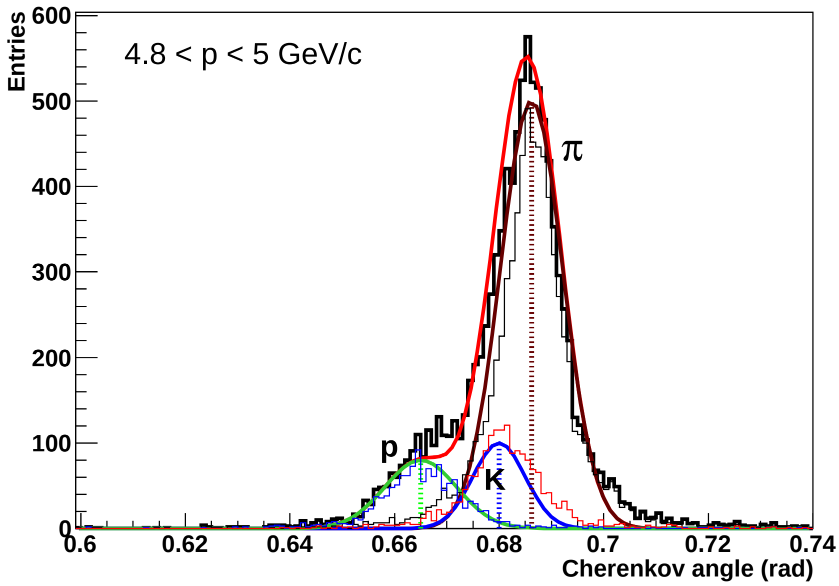

Figure 4.3: *Cherenkov angle distribution in 4.8 - 5 GeV/c from Monte-Carlo simulation. A three-Gaussian fit has been performed (red solid line) and using the parameter of the fit, three gaussian have been drawn under the red line.*

To clarify this concept, some general remarks on the fitting procedure follow. Fig.4.3 shows an example of Cherenkov angle distribution of hadrons in a 0.5 GeV/c bin centered at 4.9 GeV/c (momentum range where the overlapping between particle is higher) computed using Monte Carlo simulation. The distribution has been fitted [1]

[1]The fit is performed with ROOT framework. Another framework has been used to perform the three-Gaussian fit: RooFit. The RooFit packages provide a toolkit for modeling the expected distribution of events in a physics analysis. Models can be used to perform likelihood fits, produce plots, and generate *toy Monte Carlo* samples for various studies. The RooFit tools are integrated with the object-oriented and interactive ROOT graphical environment. In this analysis, the results from the fitting procedure using ROOT and RooFit shows no difference.

with the sum of three-Gaussian functions [2], each representing one of the three hadron species (pion, kaon and proton). The result of the fit is given by the red line in Fig.4.3. In total there are 9 parameters to estimate with the fitting procedure: 3 normalization constants, 3 mean values and 3 resolutions,

$$(N_\pi, N_K, N_p, \theta_\pi, \theta_K, \theta_p, \sigma_\pi, \sigma_K, \sigma_p) \tag{4.5}$$

The Monte-Carlo simulation allows the three Gaussian histograms to be overlapped. In the fitting procedure, the Cherenkov angle for each species is fixed to the theoretical Cherenkov angle value (θ_i): a good understanding of the detector response is very important to reduce the number of parameters to estimate. The resolution (σ_i) and the normalization constants (N_i, related to the yield) are assumed to vary between 10 - 15 % around the expected values. Hence six parameters have to be optimized by the fitting algorithm: three normalization constants (one for each species) and three resolutions (6 free parameters)

$$(N_\pi, N_K, N_p, \sigma_\pi, \sigma_K, \sigma_p)$$

In Fig.4.3 the three distribution for pions, kaons and protons are shown: the agreement with the fit results (solid lines) is quite good. Table 4.1 lists the input yields and ΔY defined as |Output yield - Input yield | (%). To stress the importance of how a detailed understanding of the detector response improves our fit, the results from a fit with three free parameters (i.e. fixing the means and the resolutions) are also added in the table: the error in the estimate is strongly reduced.

[2]The standard Gaussian formula is defined as:

$$f(\theta) = \frac{N}{\sqrt{2\pi}\sigma} \exp \frac{-(\theta - \langle\theta\rangle)^2}{2\sigma^2}, \tag{4.4}$$

Momentum	Particle	Input yield	ΔY (3 free parameters)	ΔY (6 free parameters)
4.8 - 5 GeV/c	π	7073	1.28 %	5.8 %
4.8 - 5 GeV/c	K	1797	3.78 %	6.6 %
4.8 - 5 GeV/c	p	1310	1.18 %	3.8 %

Table 4.1: *Comparing the input yields of the Monte Carlo study to yields retrieved from 3-6 parameter fit.* $\Delta Y = |Output\ yield\ \text{-}\ Input\ yield|(\%)$

.

4.3.3 Raw yields in pp collisions at 7 TeV

The yields are extracted in different p_t sub-ranges (Δp_t) in the HMPID acceptance. The Δp_t and the number of bin are summarized in the Table 4.2.

$p_t range(GeV/c)$	1.5 - 3	3 - 5	5 - 6
Δp_t	0.1	0.2	0.5
N_{bin}	15	10	2

Table 4.2: *The* p_t *range (1.5* $< p_t <$ *6 GeV/c) has been subdivided in 27* Δp_t *sub-ranges.*

This means that the range $1.5 < p_t < 6$ GeV/c is subdivided in 27 Δp_t sub-ranges. The choice is such to have the smallest Cherenkov angle variation between two neighbor bins ($\Delta\theta_{Ckov}$) and compatible with enough statistics to perform a stable fit. $\Delta\theta_{Ckov}$ has been evaluated for protons, at low p_t:

$$\Delta\theta_{Ckov} \;=\; (\theta_{Ckov})_{bin_{(i+1)}} \;-\; (\theta_{Ckov})_{bin_{(i)}} \;\leq 30\ mrad \tag{4.6}$$

where i = 1, .. 26.

We choose the protons as reference because we know that the Cherenkov angle momentum dependence is higher than for the other hadron species (close to the saturation). For each bin a fit has been performed on the Cherenkov angle distribution for positive and negative particles. In Fig.4.4 some examples of three-Gaussian fits are shown (9 parameters): the red line corresponds to the global fit while green, blue and brown lines represent the proton, kaon, and pion distributions respectively.

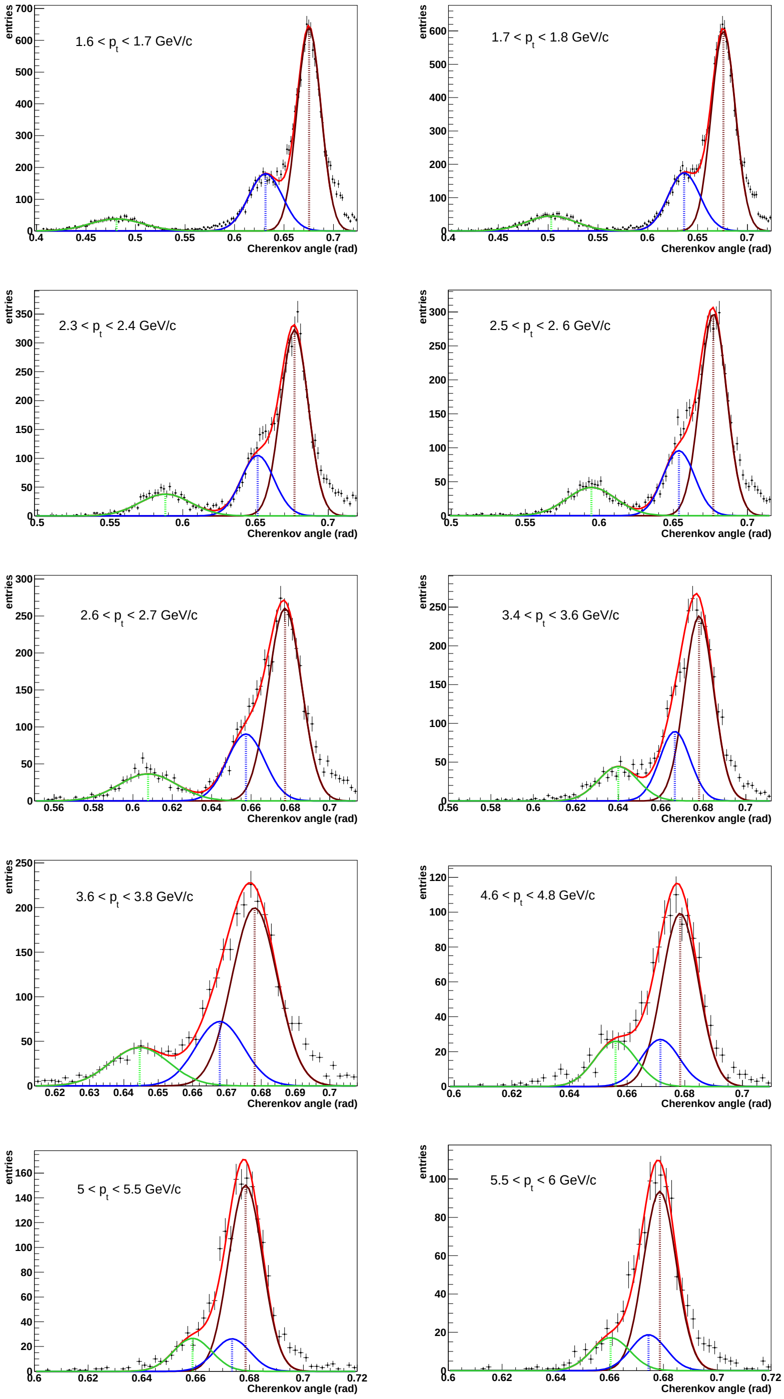

Figure 4.4: *Examples in different p_t-bins of three-Gaussian fits for negative particles. The red line represents the global fit, the green, blue and brown lines correspond to the proton, kaon and pion distributions. The fits are performed with ROOT framework.*

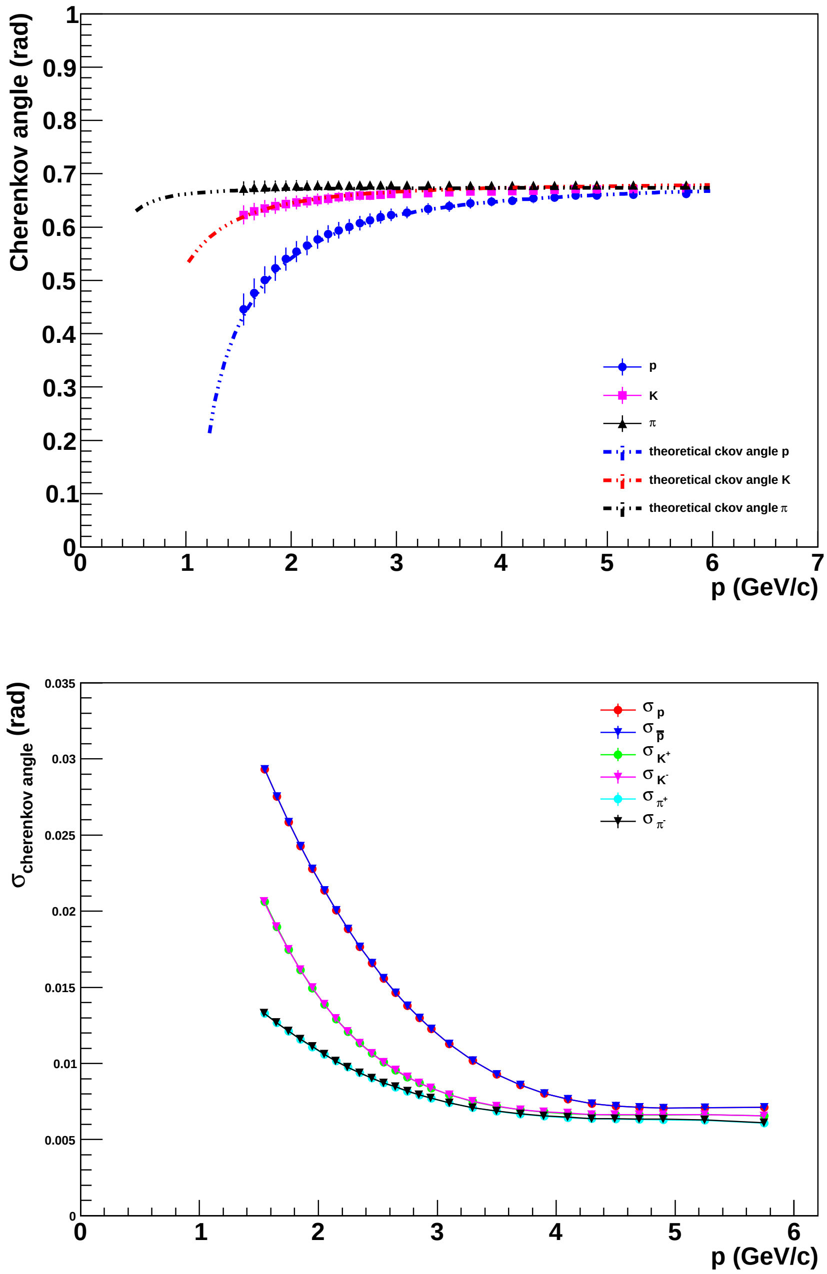

Figure 4.5: *Mean Cherenkov angle as a function of momentum is shown in the upper panel. The points have been estimate performing the fit with three-Gaussian functions. In the lower panel, the corresponding sigma* $\sigma_{cherenkov\ angle}$ *obtained from the fit are plotted.*

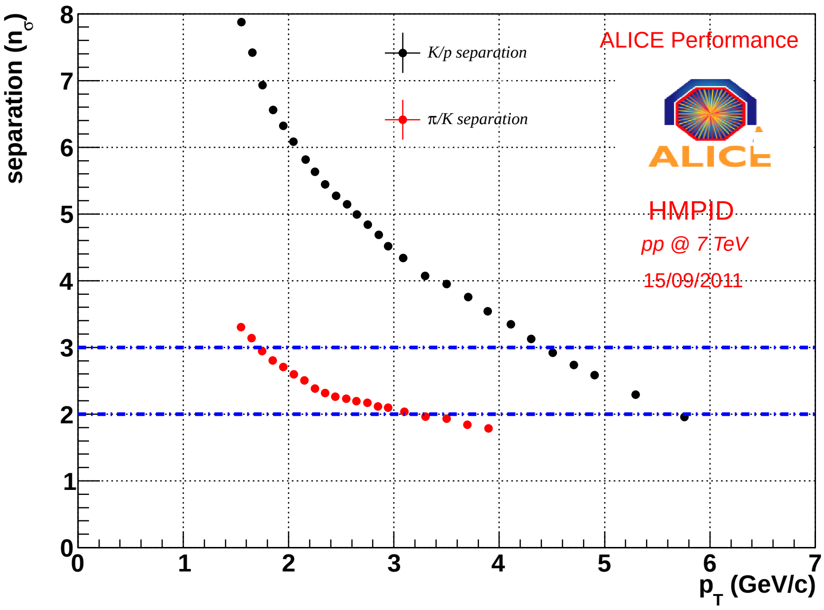

Figure 4.6: *The n-σ separation for π/K (red point) and K/p (black points) as a function of the p_t in the HMPID has been shown. The 2-σ and 3-σ separation limits are indicated by the blue dashed lines. At 3 GeV/c the π/K separation is above 2-σ and 4.4 GeV/c the K/p separation is above 3-σ.*

At intermediate momenta, pions and protons are well separated and the fitting procedure is stable, while for high p_t the separation decreases. Kaons are more difficult to identify because they are strongly contaminated by both pions and protons. Cherenkov angle values are set as input parameters allowing a variation of 5%, the resolution has been set allowing a variation of 10%. For all the fits the $\tilde{\chi}^2$ is between 1.1 and 2.6. In Fig.4.5, upper panel, the points represent the central values of the Gaussian peaks from the fitting procedure for each bin of p_t and for each species. Theoretical curves are overlapped showing the excellent agreement. In the lower panel of Fig.4.5, the corresponding sigmas obtained from the fit are also plotted as functions of momentum. The plot allows to evaluate the HMPID capability to

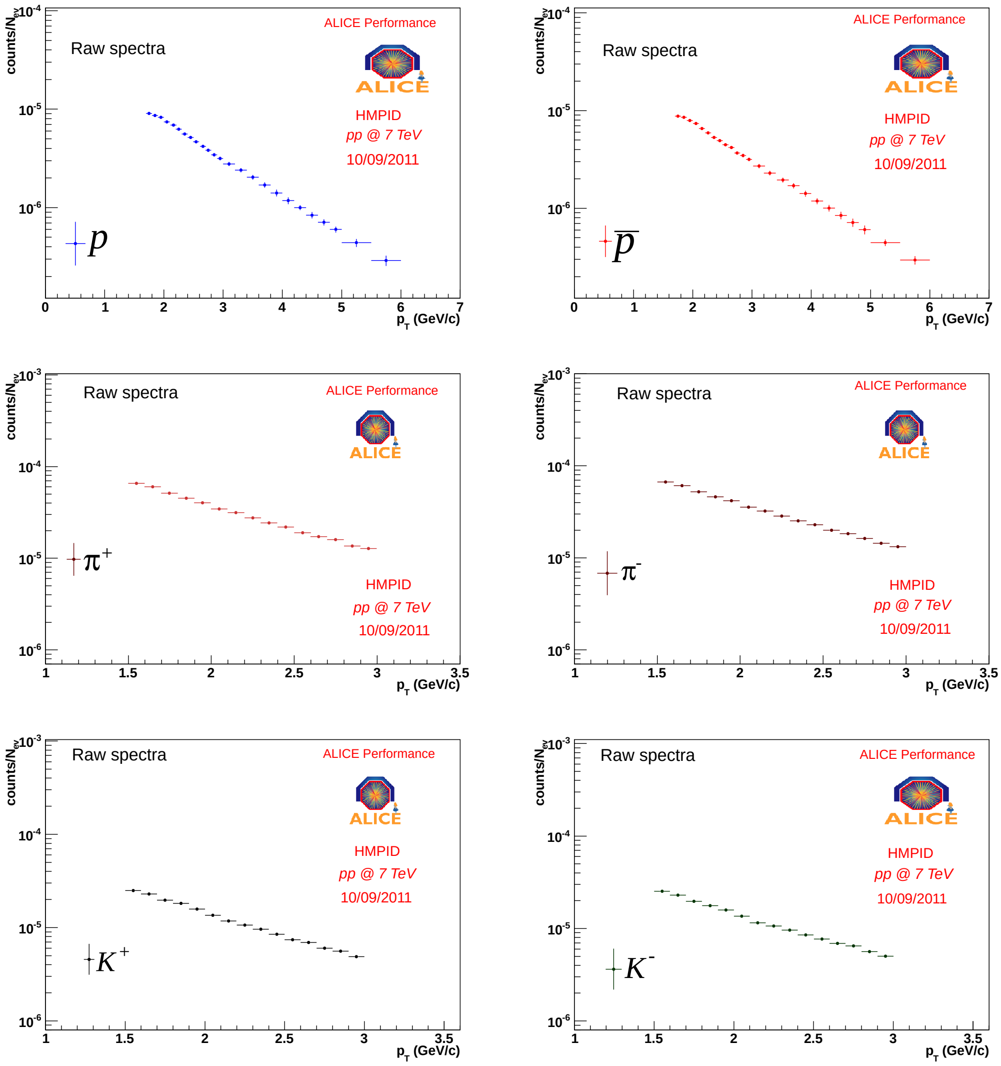

Figure 4.7: *Raw yields normalized to the number of events for positive and negative particles.*

discriminate the particles. Note that the resolution between two different particles at the same momentum is measured using the number of standard deviations of the Cherenkov angle distribution. The parameter used to indicate the separation between different Cherenkov angle distributions from two different hadron species, is defined as the ratio between ($\theta_{Ckov}(i) - \theta_{Ckov}(j)$) and the mean of the σ (for both species). The precision of the separation is measured in number of σ between the ($\theta_{Ckov}(i) - \theta_{Ckov}(j)$):

$$separation = \frac{\theta_{Ckov}(i) - \theta_{Ckov}(j)}{(\sigma(i) + \sigma(j))/2} \tag{4.7}$$

with i, j = π, K, p.

In Fig.4.6 the n-σ separation for π/K (red point) and K/p (black points) as a function of p_t is shown. The 2-σ and 3-σ separation ranges are indicated by the blue dashed lines. Up to 3 GeV/c the π/K separation is above 2-σ while the K/p separation is above 3-σ up to 4.4 GeV/c. Raw yields normalized to the number of events are shown in Fig.4.7. The yields of pions, kaons, protons and anti-protons are measured from 1.5 GeV/c up to 3.4 GeV/c for pions and kaons, from 1.5 GeV/c up to 6 GeV/c for protons and anti-protons. Only statistical errors are shown.

4.4 Corrections

In order to get the final distribution it is necessary to correct for the efficiency of the detector, for the geometrical acceptance, for the transport code used in Monte Carlo, for the contamination from secondary tracks and for the cuts used in the analysis. We can subdivide the corrections in three main categories as listed below:

- Acceptance and efficiency. Under this general name, we denote the following corrections:
  - Tracking efficiency: it is related to the detectors devoted to the tracking

procedure (ITS and TPC);

– Geometrical acceptance: the geometrical acceptance of the HMPID is only 5 % of the TPC. To compare our spectra with the other detectors, it's necessary a proper correction;

– PID efficiency: as explained in the previous chapter, the spectra are corrected for the PID efficiency evaluated both from data (protons and pions) and form Monte Carlo simulation (kaons);

– Correction factor for the MIP charge discrimination: it is related to the rejection of the tracks with Q < 150 ADC;

– Correction factor for the matching selection: it is important to understand how many tracks we reject using this cut and how to correct in properly way.

- Transport code: the particles are propagated through the detector with a transport code framework. Corrections have been evaluated.

- Feed down: the corrections needed to take into account the contamination of the secondary particles from interactions in the detector material and of strange particle decays with the primary tracks have been evaluated.

4.4.1 Acceptance and efficiency correction

The correction factors due to tracking efficiency and geometrical acceptance are evaluated from the Monte Carlo simulation. A sample of 80 M of events propagated through the detector with the GEANT3 transport code are used. The same cuts set up for the data are used in the Monte-Carlo analysis. We define the tracking efficiency as the ratio between the number of reconstructed tracks and the number of those generated by the Monte Carlo simulation in $|\eta| < 0.9$ and $|y| < 0.5$. It is given by:

$$Eff_{traking} = \frac{(dN/dp_t)_{reconstructed}}{(dN/dp_t)_{generated}} \tag{4.8}$$

and is related to the systems (TPC and ITS) devoted to the track reconstruction. The geometrical acceptance of the HMPID detector is defined as:

$$Acc_{HMPID} = \frac{(dN/dp_t)_{HMPID}}{(dN/dp_t)_{reconstructed}} \tag{4.9}$$

where the $(dN/dp_t)_{HMPID}$ are the tracks with a signal crossing the HMPID chambers. In the Acc_{HMPID} we consider the effect due to the dead zones between the HMPID chambers. In order to simplify the analysis, the convolution of tracking efficiency and geometrical acceptance has been evaluated:

$$Eff = Eff_{tracking} \times Acc_{HMPID} \tag{4.10}$$

In Fig.4.8 the convoluted tracking efficiency and geometrical acceptance is shown for positive and negative particles as function of the transverse momentum (1.5 < p_t < 3.5 GeV/c for pions and kaons, 1.5 < p_t < 6 GeV/c for protons). At very low p_t (p_t < 1 GeV/c), the 0.5 T magnetic field bends the tracks out of the HMPID profile; the geometrical acceptance rises as a function of p_t. For p_t < 3 GeV/c the anti-proton and proton behaviours are different due to the anti-protons annichilation in the material. At very high p_t (p_t > 4.5 GeV/c), the fluctuations are due to the low number of tracks crossing the HMPID. For this reason, the distributions are fitted with polynomials and these are used to correct the raw spectra.

4.4.2 Correction factor for the MIP charge discrimination

As introduced in Chapter 3, the identification of the charged particle with the HMPID requires tracks from the central tracking devices to be extrapolated and associated with a ionization cluster in the HMPID cathode plane. The basic step in the analysis procedure is the discrimination between a photon and a given MIP cluster.

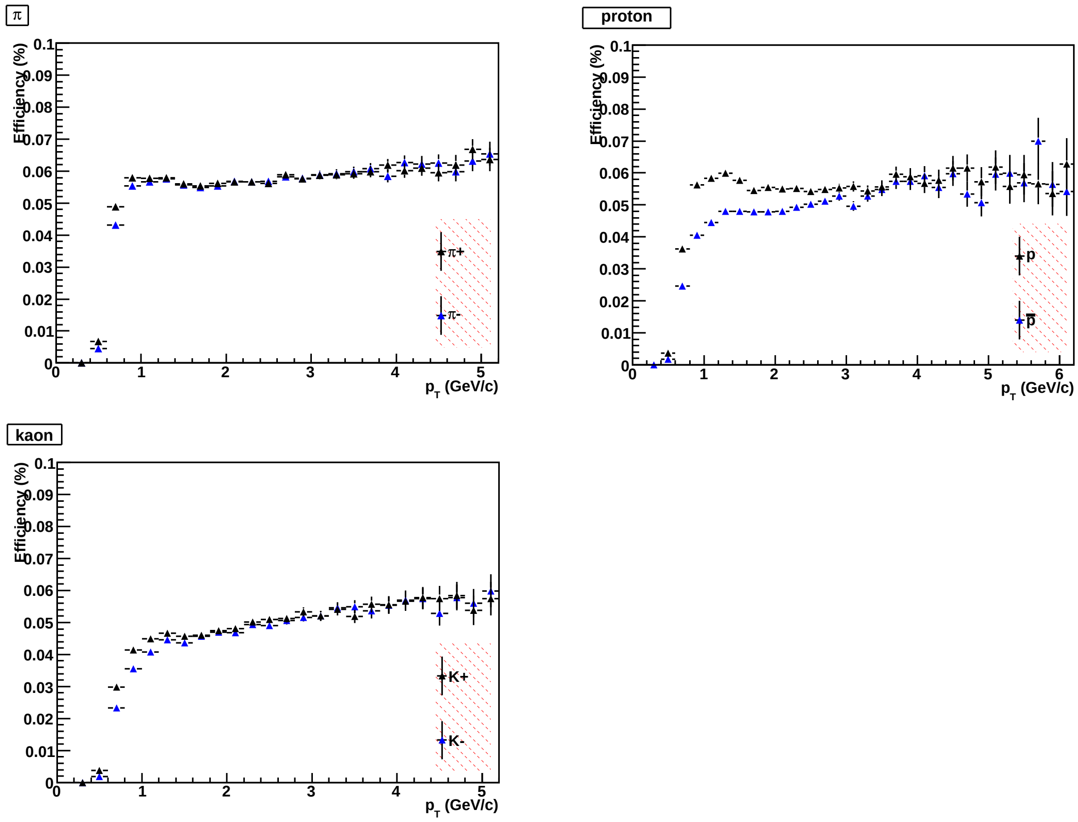

Figure 4.8: *Convolution of tracking efficiency and HMPID geometrical acceptance for positive and negative π, K, p.*

This selection is made by applying a threshold cut on the cluster charge: Q_{MIP} > 150 ADC. This cut has been applied on the present analysis and the correction factor has been evaluated from the data sample,

$$Correction\ factor_{MIP-charge} = \frac{dN/dp_t^{Q>150}}{(dN/dp_t)_{tot}} \tag{4.11}$$

and estimated to be less than 1%.

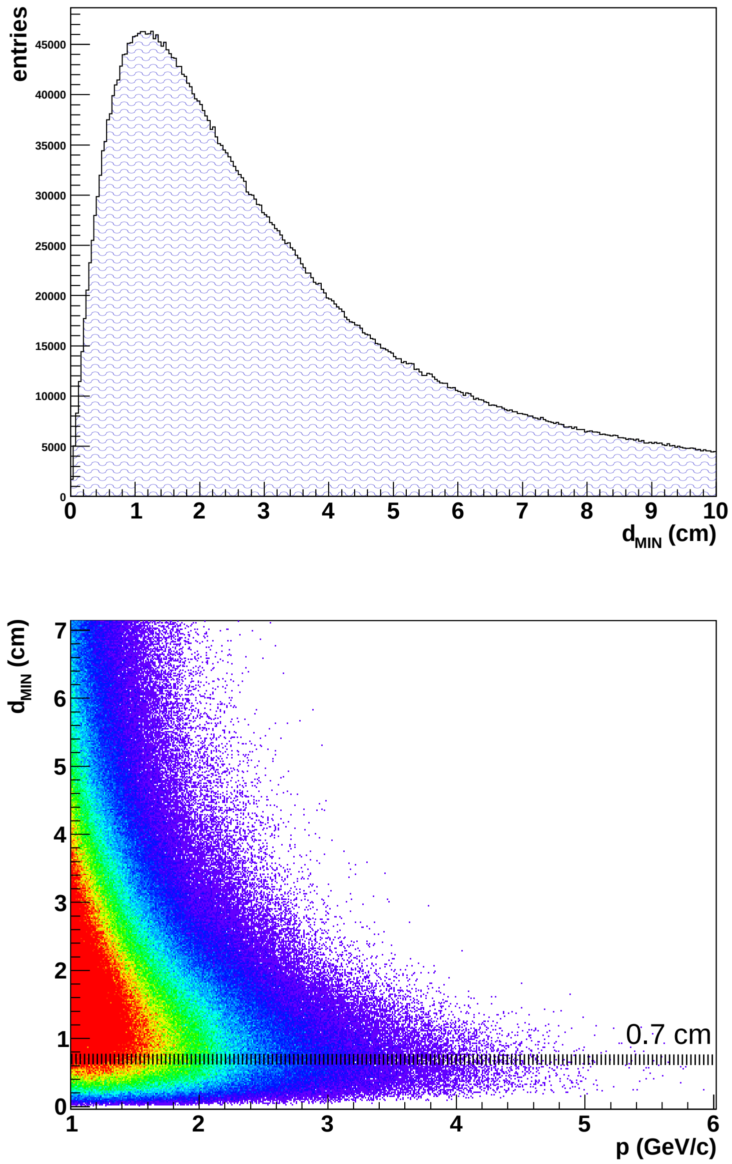

Figure 4.9: *Upper panel: distribution of the distance d_{MIN} between the extrapolated track position at the HMPID photocathode plane and the nearest MIP centroid (Q_{MIP} > 150 ADC) in pp collisions at $\sqrt{s}$ = 7 TeV. Lower panel: The plot shows the distribution d_{MIN} as a function of track momentum. At low p, the effect of the multiple scattering is more evident and the cut on the distance is very useful to reject tracks without a good matching.*

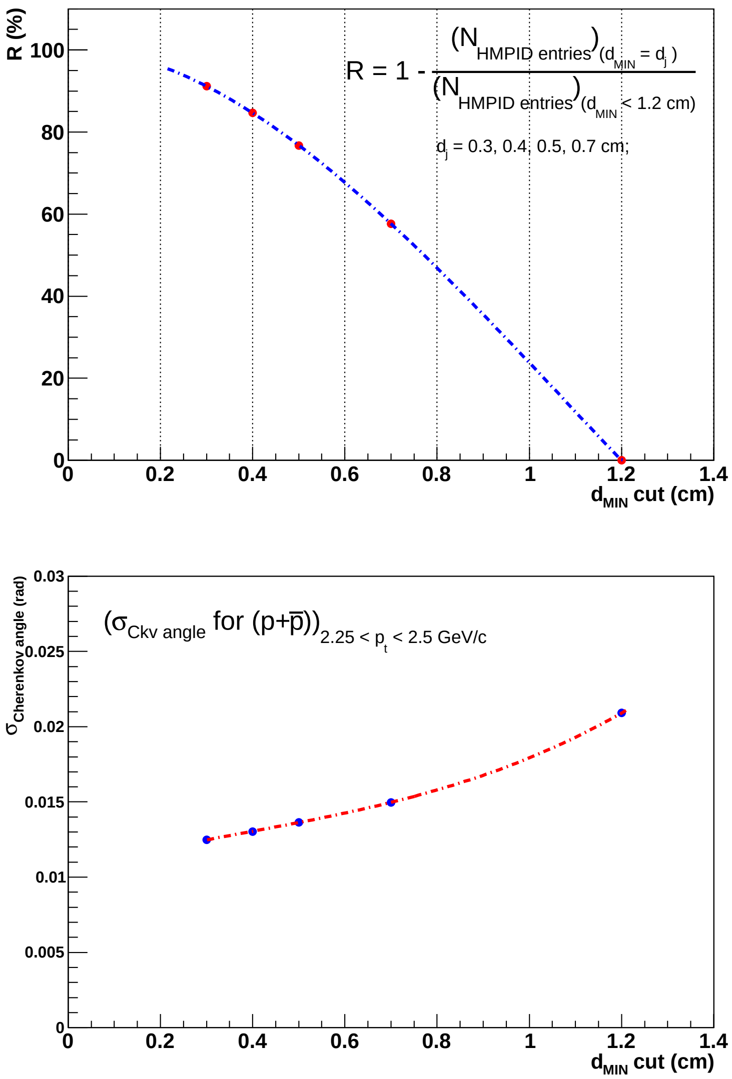

Figure 4.10: *In the upper panel the R factor as a function of d_{MIN} cut is shown. R gives an estimate of the number of lost tracks in the HMPID as a function of the d_{MIN} cut, starting from d_{MIN} = 1.2 cm. Using a cut at d_{MIN} < 0.4 cm about 80% of the tracks are rejected. In the lower panel, the $\sigma_{Cherenkov\ angle}$ in $2.25 < p_t < 2.5$ GeV/c as a function of d_{MIN} cut : if the cut is strong the resolution increases, but the statistics decreases.*

4.4.3 Correction factor for the matching selection

A cut on the distance d_{MIN} between the extrapolated track point in the HMPID photocathode plane of a given chamber and the coordinate of the nearest centroid, having a charge compatible with a MIP cluster has been applied.

In Fig.4.9 upper panel, the d_{MIN} distribution for real data is shown. In the lower panel, the plot of d_{MIN} as a function of the track momentum shows how the multiple scattering affects d_{MIN}.

It is important to stress that the inclination angle θ_{trk} [3] has to be known with high precision. In fact it determins the shape of the ring and then systematically affects the value of the Cherenkov angle θ_{Ckov}. In order to reduce the error on the inclination angle θ_{trk}, the selection $d_{MIN} < 0.7$ cm has been applied in the whole range of track momentum. This cut reduces the probability of the mismatching of a track with the MIP cluster of another particle (the cut is of the order of the pad size), even if the efficiency will decrease.

We define the ratio:

$$R = 1 - \frac{(N_{HMPID\ entries})_{d_{MIN}<d_j}}{(N_{HMPID\ entries})_{(d_{MIN}<1.2cm)}} \tag{4.14}$$

where the numerator is the number of reconstructed tracks selected after different matching cuts and the denominator is the number of reconstructed tracks after a cut of 1.2 cm. It represents the number of the total tracks lost as a function of the matching cuts. In this case, $d_{MIN} = 1.2$ cm is taken as a starting point for the

[3] It represents the inclination angle of the tracks in the HMPID reference system. We remember that for each track, it is stored the information of particle coordinates and of the inclination angles to the HMPID photo-cathode in global (ALICE) reference system:

$$(x, y, \theta_{trk}, \phi_{trk})_{global} \tag{4.12}$$

With proper coordinate transformation, the same parameters are evaluated in the local (HMPID) reference system.

$$(x, y, \theta_{trk}, \phi_{trk})_{local} \tag{4.13}$$

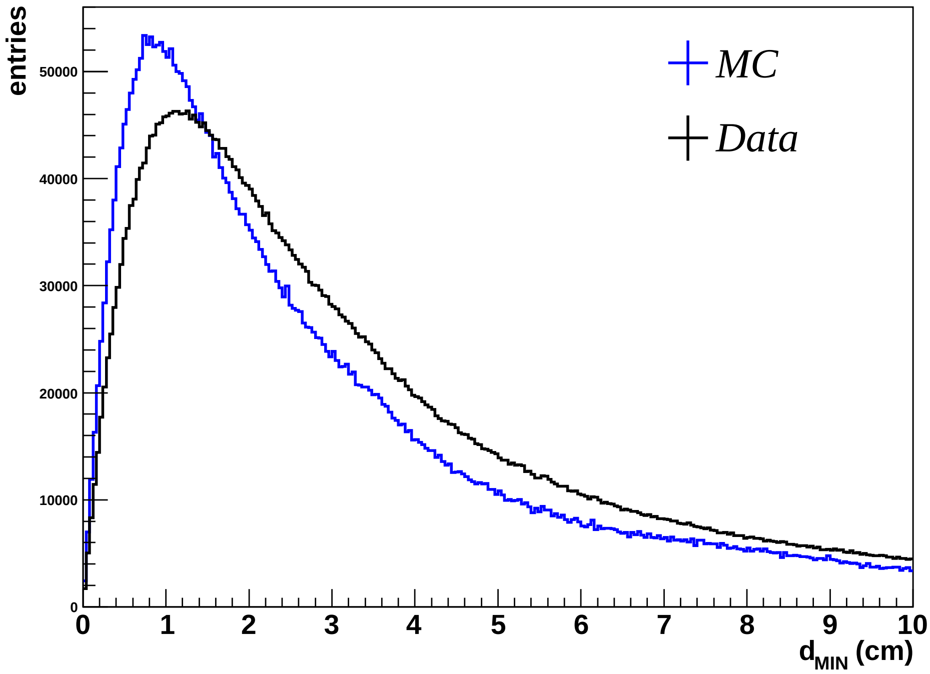

Figure 4.11: *The d_{MIN} distribution for Monte-Carlo and data. The MC - data comparison has been carried out scaling the data distribution to the Monte-Carlo. The two behaviours are clearly different: both curves show a Landau behaviours but the peak values are displaced from each other. This difference comes from the underestimate of the material budget in Monte Carlo simulation. We can deduce that the Monte-Carlo, for the matching correction, cannot be used.*

matching selections (as shown in the upper panel in Fig.4.10). Using a cut at d_{MIN} = 0.4 cm about 80% of the tracks are rejected.
In the lower panel, the $\sigma_{Cherenkov\ angle}$ is shown as a function of the d_{MIN} cut in $2.25 < p_t < 2.5$ GeV/c. If the cut is strong the resolution increase, but the statistics decrease. A good compromise has been to choose $d_{MIN} = 0.7$ cm, which gives the best resolution with minimum loss of statistics.

The correction related to the matching selection should be done using the Monte-Carlo simulation. The comparison on the d_{MIN} distribution between MC and data is shown in Fig.4.11, where the data distribution has been scaled to MC to help the comparison. The two peaks have different values: 0.8 cm for the blue line (MC), 1.2 cm for the black one (data); in addition, the MC distribution is narrower, due to the non perfect description of the material budget in the Monte Carlo simulation.

The correction factor for the matching selection has been evaluated using the HMPID PID procedure. The probability that a given reconstructed θ_C belongs to the probability density function (*pdf*) of the particle type i = π, K, p, and falls in the interval $[\theta, \theta + d\theta]$ is

$$P(\theta_C)d\theta = GAUSS(\theta_{C,i}, \sigma_{\theta_C,i})d\theta, \tag{4.15}$$

where $\theta_{C,i}$ can be found from the knowledge of the response function of the detector. The probability that a particle with given θ_C is of the type i = π, K, p is

$$P_i = \frac{GAUSS(\theta_{C,i}, \sigma_{\theta_C,i})}{\sum_{i=\pi,K,p} GAUSS(\theta_C, \sigma_{\theta_{C,i},i})} \tag{4.16}$$

It is possible to choose a significance level to identify a given particle. The selection of three bands, in the Cherenkov angle as a function of track momentum (Fig.4.12) has been performed using the probability greater than 0.7 for protons, pions and kaons. Fig.4.13, left panels, shows the d_{MIN} distribution for positive and negative particles

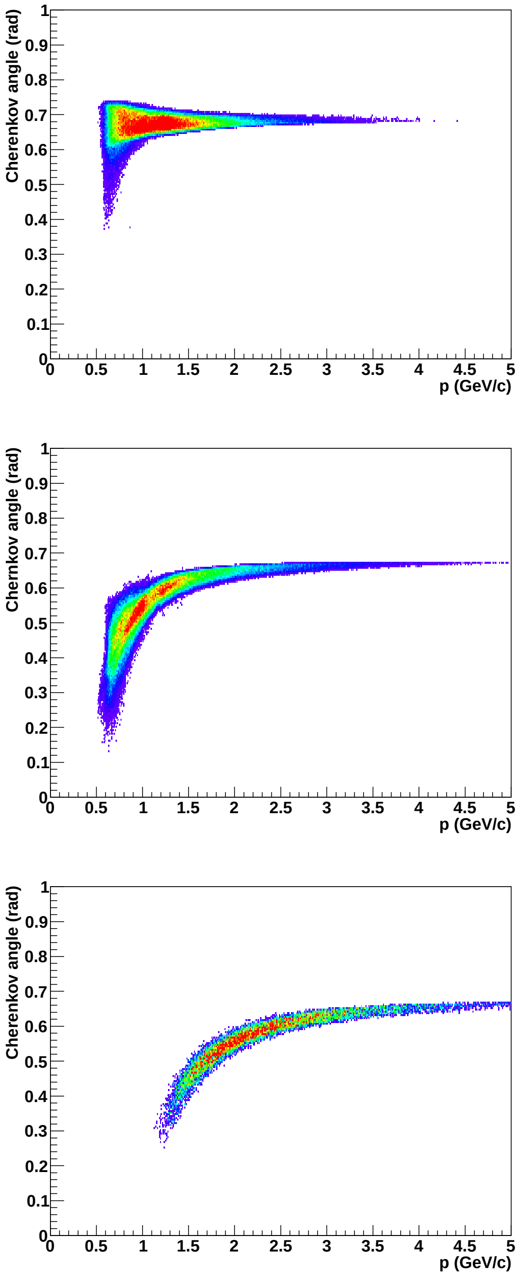

Figure 4.12: *Cherenkov angle distribution as a function of the track momentum in pp collisions at* $\sqrt{s} = 7$ *TeV using PID. PID is the only mean to correct the matching cut used in the analysis. Only positive particles are shown. Upper plot:* π^+*; Middle:* K^+*; Lower: p.*

obtained using a probability greater than 0.7, and track momentum greater than 1.5 GeV/c. We define the correction related to the matching selection as

$$Correction\ factor_{matching} = \frac{dN/dp_t^{d_{MIN}<d_{CUT}}}{(dN/dp_t)_{tot}} \tag{4.17}$$

where d_{CUT} = 0.7 cm. $dN/dp_t^{d_{MIN}<d_{CUT}}$ denote the number of the tracks after the matching selection, while $(dN/dp_t)_{tot}$ is the number of the total tracks to the HMPID without selection. The correction factor has been evaluated for each sub-range of p_t (Δp_t) and the results, for positive and negative particles, are shown in Fig.4.13 (right panels): red points represent pions while blue and black points represent kaons and protons respectively. The curves have been fitted with a second order polynomial and the values are used to correct the raw spectra.

4.4.4 Transport code correction

The tracking efficiency, the geometrical acceptance and the PID efficiency for kaons used in this analysis are calculated from Monte Carlo simulation. The events are generated with the Photojet (the event generator) and the particles are propagated through the detector with the GEANT3 transport code in AliROOT. GEANT3 reproduces the absorption cross section of hadrons incorrectly, overestimating the measured cross section. The transport code FLUKA contains a more accurate description of these cross sections [105], and a dedicated simulation is used to calculate the correction to the GEANT3 efficiency calculations. The absorption correction factors calculated with GEANT3 were scaled to match the correct (FLUKA) cross section parametrization. In the calculation, the estimate of the material budget for TPC, TOF and TRD has been taken into account. In the HMPID range, this is relevant mainly for antiprotons at low p_t, where the correction is of the order of 2% up to 2 GeV/c; for higher p_t the corrections decrease to the order of 1%. For the other particles and at higher p_t, the difference between GEANT and FLUKA calculations

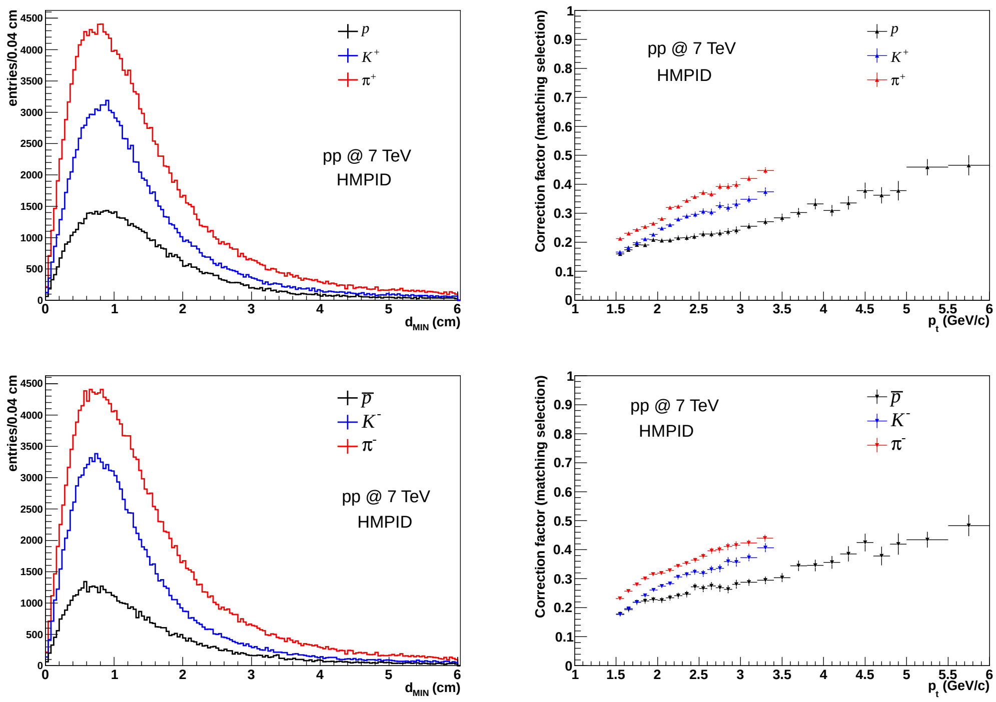

Figure 4.13: *Upper left panel (lower left panel):* d_{MIN} *distribution for* π^+, K^+ *and* p (π^-, K^- *and* $\bar{p}$)*. Only tracks with* $p >$ *1.5 GeV/c are taken into account; Upper right panel (lower right panel): correction factors for the matching selection for positive (negative) particles.*

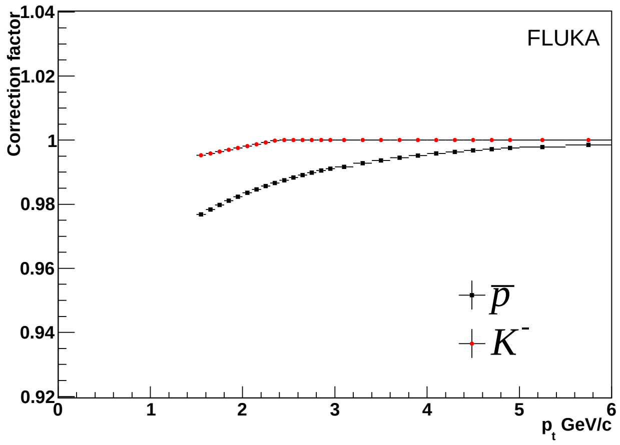

Figure 4.14: *FLUKA corrections ($\bar{p}$ and K^-) to take into account the overestimate cross section with GEANT3. At high p_t ($p_t > 4$ GeV/c), the correction is negligible for the HMPID detector.*

is negligible. Fig.4.14 shows the corrections obtained with FLUKA for antiproton and negative kaons.

4.4.5 Feed-down

The secondary particles from interactions in the detector material and strange particle decays can be mis-identified as primary tracks and have to be subtracted from the yield. These secondary tracks are indicated as feed-down contribution. The contamination from secondaries is mostly relevant for protons, and it is corrected by re-scaling the fraction of secondaries estimated from the Monte-Carlo to the data. The DCA distribution in the data (for the primary tracks with the feed-down contribution) is fitted with the Monte Carlo templates, obtained for primary particles, secondaries from weak decays and secondaries from material separately. In Fig.4.15, the DCA distribution from Monte Carlo simulation in 5 bin of p_t is shown. The black line represents the DCA for all the tracks generated, the blue one is for the primary tracks, the red line is for the tracks from weak decays and the green line is for the tracks from the interaction in the material. Only in the first bin of p_t , the latter component is present. In the case of anti-protons, the contamination of secondaries from material is negligible so that only the first template is used. In Fig.4.16, the DCA distribution for all the tracks (black points) is shown. Using the MC templates, the DCA for primary, weak decays and from material (not present) are retrieved. In Tab.4.3 the Correction factor defined as:

$$Correction\ factor_{feed-down} = \frac{(dN/dp_t)_{(weak\ decay)} + (dN/dp_t)_{(material)}}{(dN/dp_t)_{(tot\ =\ primary\ +\ weak\ decay\ +\ material)}} \quad (4.18)$$

is evaluated for proton and anti-proton. The values have to be subtracted from the final yields.

Momentum transverse (p_t)	1.5 - 2.5	2.5 - 3.5	3.5 - 4.5	4.5 - 6.
proton	4.2%	3.2 %	3.0 %	2.7 %
anti-proton	4.7%	3.6 %	3.2 %	2.8 %

Table 4.3: *Feed down correction for protons and anti-protons.*

4.5 Systematic uncertainties

Systematic errors	$\pi^{\pm}$	$K^{\pm}$	p and $\bar{p}$
fitting procedure	< 5%	< 9%	< 4%
secondary from material	negl.	negl.	negl.
secondary from weak decay	negl.	negl.	1%
tracking eff./ geom. accept./matching selection	< 7%	< 7%	< 7%
PID efficiency (MC)	< 4%	< 6%	< 4%
material budget	< 5%	< 5%	< 5%
MIP charge discrimination	negl.	negl.	negl.

Table 4.4: *Summary of the systematic uncertainties in the HMPID analysis using the standard tracking.*

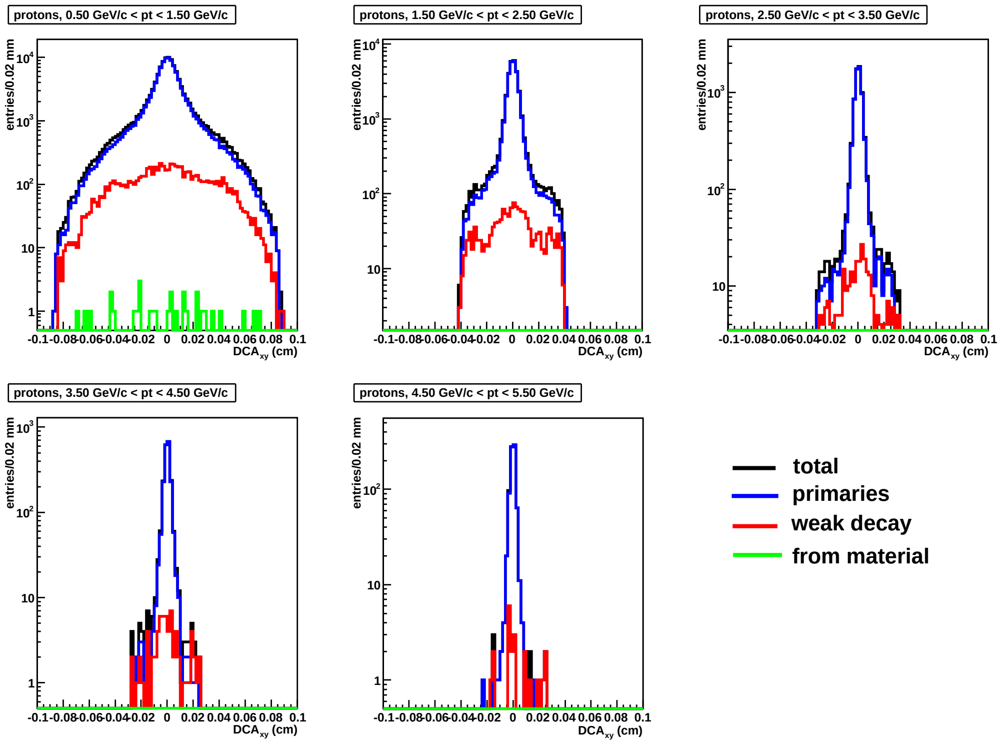

Figure 4.15: *DCA distribution from Monte Carlo simulation in 5 bins of* p_t *. The black line represents the DCA for the primary tracks selected after the cuts, the blue one the primary tracks obtained from the generator. The red line represents the tracks from weak decays, the green line the tracks from interaction in the material. The material component is only present in the first* p_t*-bin. In the HMPID analysis the component distribution coming from material is negligible.*

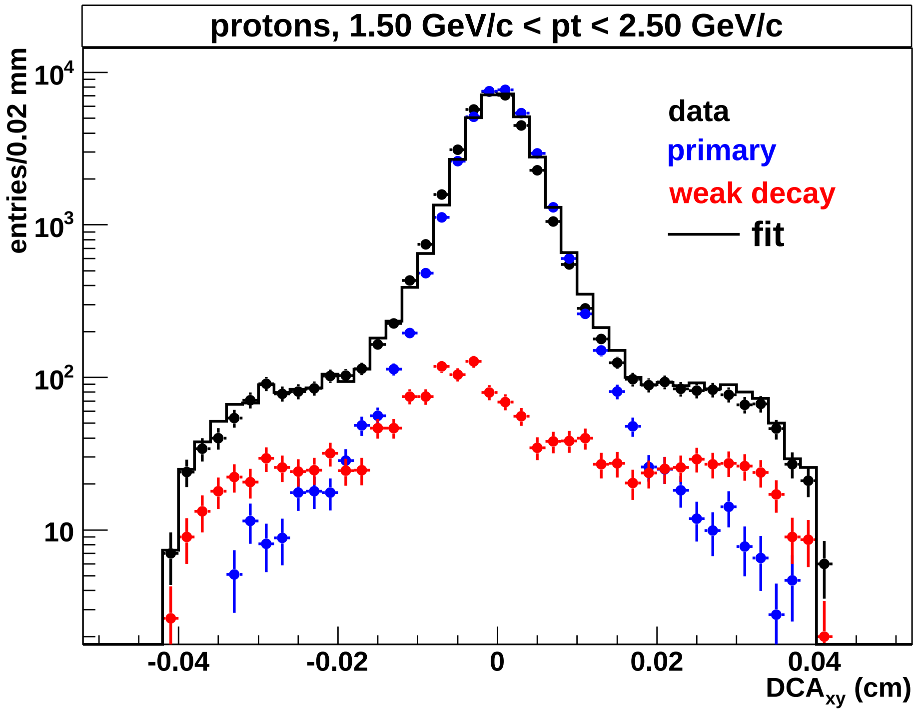

Figure 4.16: *Fit of the DCA distribution using the Monte Carlo templates. The example shows the DCA distribution for protons in 1.5 < p_t < 2.5 GeV/c. The black point represents the data, the solid line is the fit performed using the MC template. The blue points are the primary protons while the red points represent the protons coming from the weak decays.*

In this section the description of the systematic uncertainties in the HMPID analysis is presented. The main sources of systematic uncertainties are summarized in Tab.4.4 where are shown the maximal values of the errors estimated over the full transverse momentum range.

- **Fitting procedure:** the systematic contribution from the fit procedure has been estimate varying the fit conditions.

  - different fitting algorithm (e.g MIGRAD, MINUIT);
  - varying, within reasonable values, the input parameter for the mean and the sigma. Different combinations are used: changing only the mean, only the sigma and mean and sigma at the same time.

  The largest error has been inserted in Tab.4.4. Note that these systematic uncertainties are strongly dependent on the p_t as shown in Fig.4.18. The 9% quoted for kaons systematic uncertainties is due to the strong contamination by both pions and protons;

- **Secondary from material:** the contamination due to secondaries produced in the interaction with material are negligible at high p_t;

- **Secondary from weak decay:** the fits to the impact parameter DCA distribution have been repeated using different fit functions for the three components, as described before. The errors are negligible.

- **Tracking efficiency/geometrical acceptance and matching selection:** the full analysis chain has been repeated varying the number of the TPC cluster, the χ^2 and the d_{MIN} upper limits. The obtained values are summarized in Tab.4.4.

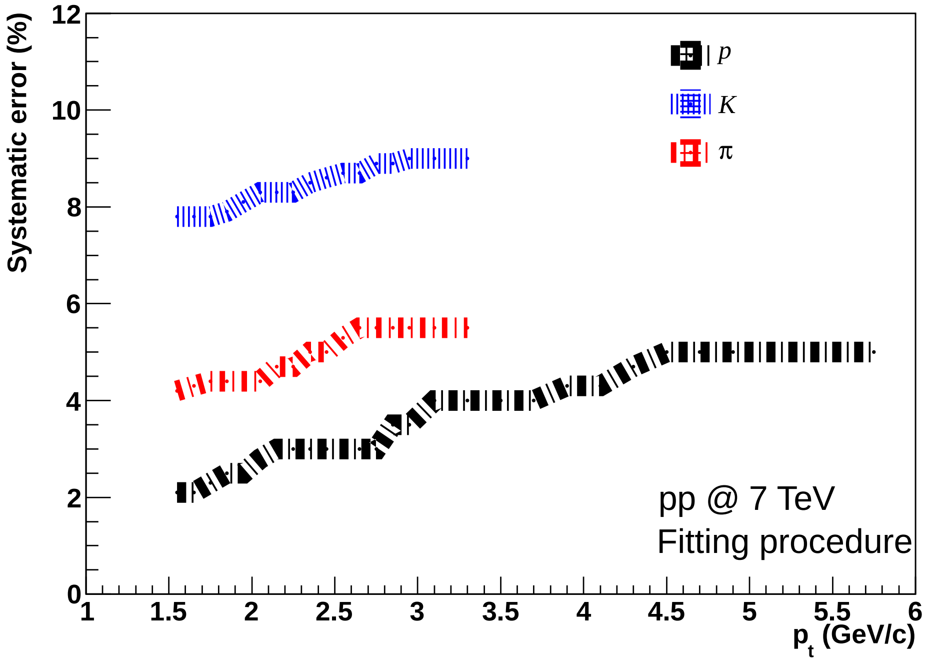

Figure 4.17: *Systematic errors coming from the fitting procedure. The errors are* p_t *dependent. Kaons are affected by greater systematic uncertainties because they are strongly contaminated by pions and protons.*

- **PID efficiency:** we evaluated the PID efficiency from data and MC. Varying the cuts used in the analysis (MC and data) the estimate of the error is less than 4% for protons and pions and less than 6% for the kaons (MC). The errors coming from the fitting procedure are negligible.

- **Material budget:** as explained in the Chapter 2, there is a significant material budget before the HMPID. The related uncertainty has been estimated with a dedicated Monte Carlo simulation by modifying the material budget by $\pm$ 10 %.

- **MIP charge discrimination:** The systematic uncertainties related to the MIP charge selection are negligible.

4.6 Results on identified charged hadrons

4.6.1 Spectra

Finally, the raw yields have been extracted performing three-Gaussian fits to the Cherenkov angle distribution. The final spectra have been corrected for several factors evaluated both from data and Monte Carlo simulation. The PID efficiency for protons and pions has been evaluated from data and for kaons from MC as described in the Chapter 3. The tracking efficiency plus geometrical acceptance (calculated together), feed down and transport code correction factors have been evaluated using MC simulation. Correction factors for matching selection have been retrieved from data using the PID method (assigning a probability to each track). In the last step, the systematic uncertainties have been included. The fully corrected HMPID spectra in pp collisions at $\sqrt{s} = 7$ TeV are shown in Fig.4.18.

The spectra from ITS stand-alone, TPC, TOF and HMPID will be combined in order to cover the full transverse momentum range (see Tab.4.5). Preliminary

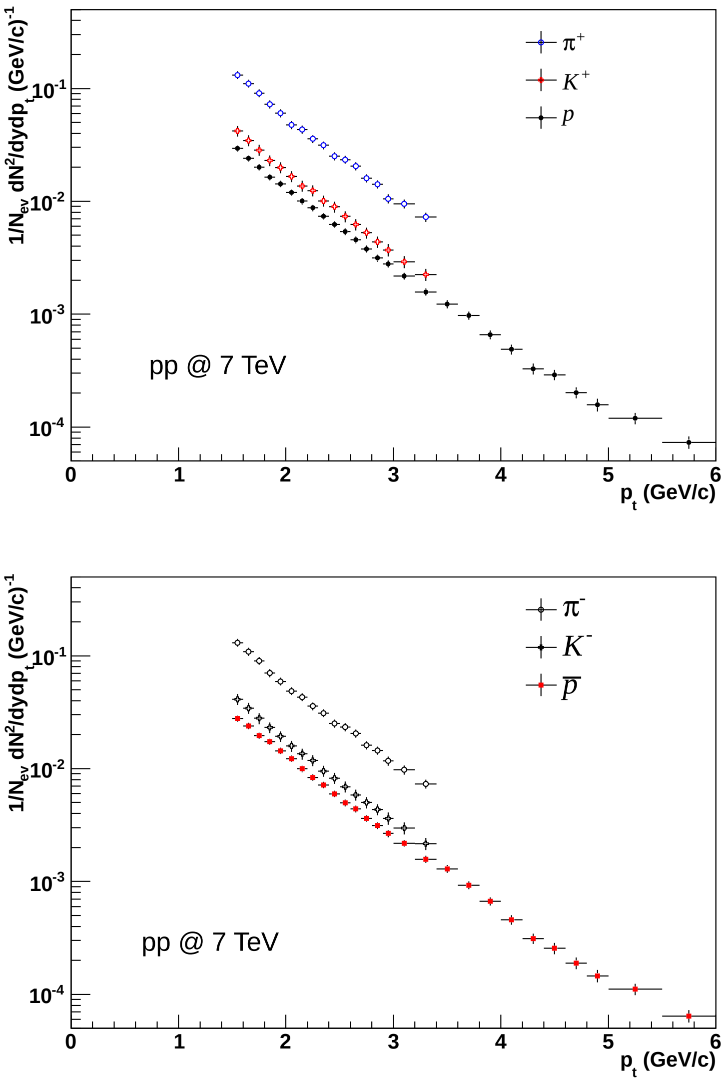

Figure 4.18: *Transverse momentum spectra of positive and negative hadrons for pp collisions at* $\sqrt{7}$ *TeV obtained using the HMPID detector. In the error bars, the statistical and systematic errors are considered.*

comparisons between different analysis show good agreement with difference less than 5 %.

	ITS	TPC	TPC-TOF	TOF	HMPID
TRACKS	stand-alone	global	global	global	global
Type of PID signal	dE/dx	dE/dx	dE/dx , time	time	Cherenov
Method of extraction	σ cut	unfolding	unfolding	unfolding	unfolding
Ranges in p_t (GeV/c)	0.1 - 0.5 (π) 0.2 - 0.5 (K) 0.3 - 0.55(p)	0.2 - 0.55 (π) 0.25 - 0.5 (K) 0.4 - 0.85 (p)	0.2 - 1.4 (π) 0.25 - 1.4 (K) 0.4 - 0.85 (p)	0.5 - 2.5 (π) 0.5 - 2.5 (K) 0.9 - 3.5 (p)	1.5 - 3.4 (π) 1.5 - 3.4 (K) 1.5 - 6. (p)

Table 4.5: *The PID in the ALICE experiment is performed by different detectors and techniques.*

The measured HMPID spectra cover a limited range. Parameterizing the spectra with an analytical function, it is possible to extrapolate into the unmeasured p_t regions in order to determinate the yields and to evaluate the $\langle p_t \rangle$.

In the past, exponential functions (as explained in Chapter 1),

$$\frac{d^2N}{p_t dy dp_t} = Ae^{\frac{-m_t}{T}} \tag{4.19}$$

have been used to extrapolate spectra to low transverse momentum while QCD-inspired power-law functions,

$$\frac{d^2N}{p_t dy dp_t} = B(1 + \frac{p_t}{p_0})^{-n} \tag{4.20}$$

seem to provide a better description of the high p_t region ($p_t \geq 3$ GeV/c) [97, 110, 111, 112, 113]. We can assume that the p_t coverage of HMPID detector is large enough that a function which accounts for both the power-law component of the spectra and the low p_t turnover becomes necessary to describe the data. In the ALICE experiment, for the pp collisions at $\sqrt{s} = 900$ GeV and for the preliminary results at $\sqrt{s} = 7$ TeV the Lévy (or Tsallis) function [108, 109] has been used:

$$\frac{d^2N}{p_t dy dp_t} = \frac{dN}{dy}\frac{(n-1)(n-2)}{nC(nC+m_0)(n-2)}(1 + \frac{\sqrt{p_t^2 + m_0^2} - m_0}{nC})^{-n} \tag{4.21}$$

with the fit parameters are n, C, dN/dy. For the present analysis, the spectra has been fitted for the three species with eq. 4.20 and eq. 4.21.

Normalization to the number of INELASTIC collisions A common classification of inelastic pp collisions (**INEL**) is into **non-diffractive (ND)**, **single-diffractive (SD)**, **double-diffractive (DD)** events. The distribution of the particles in the final state are significantly different for each of these processes. Non-diffractive collisions have many particles in the central region (falling to higher rapidities). In a single-diffractive collision only one of the beam particles break-up and produces particles at high rapidities on one side. In a double-diffractive collision both beam particles breaks-up and produce particles at positive and negative high rapidity; In the central region a dip is present.
The normalization to the number of INEL has been carried out. ALICE, in fact, is not able to distinguish the physics processes event-by-event but different trigger algorithms that maximize the overall efficiency in selecting inelastic (INEL) and non single-diffractive (NSD) events can be defined combining signals from several detectors (forward and central detectors) [107, 106].

In order to compare to previous experimental results, which are only published for the non single diffractive (NSD) class, the HMPID spectra are scaled for the measured ratio,

$$\frac{(dN/d\eta)_{NSD}}{(dN/d\eta)_{INEL}} \simeq 0.864 \tag{4.22}$$

The first attempt is made with eq. 4.20 and then with eq. 4.21. A summary of the resulting χ^2/ndf from each fit is given in the Tab.4.6.

The χ^2/degree-of-freedom is calculated using the total (statistical and systematic) error. This explains the low χ^2 values less than 1. In particular, for kaons, the systematic errors probably have been overestimated. The contribution coming from the extrapolation of the spectra to infinite momentum is negligible. We remark that the fitting procedure is made on 27 points for the proton and antiproton spectra, and on 17 points (and in a smaller transverse momentum range) for pions and kaons.

	Power-Law	Lévy
Particle	χ^2/ndf	χ^2/ndf
π^+	4.9/14	4.8/14
π^-	2.67/14	2.66/14
K^+	0.85/14	0.827/14
K^-	0.229/14	0.22/14
p	8.15/24	8.05/24
$\bar{p}$	10.424/24	10.19/24

Table 4.6: *A summary of χ^2 per degree of freedom values for different fit-functions to p_t spectra.*

Both functions give a good description of the HMPID spectra. In Fig.4.19 and Fig.4.20 the fit with power-law and Lévy function are shown. To evaluate the mid-rapidity yields and mean transverse momenta the Lévy function has been used.

$$\langle p_t \rangle = \frac{\int p_t f(p_t) dp_t}{\int f(p_t) dp_t} \tag{4.23}$$

where f(p_t) is the Lévy function and the integral is made from the lowest p_t experimentally accessible p to infinite momentum. The values obtained are summarized in the Tab.4.7 with statistical errors. The first comparison of this measurement is done with the results obtained from ALICE at lower p_t . Fig.4.21, upper panel, shows $\langle p_t \rangle$ for π, K and p for different collisions energies. The plot has been obtained using ITS, TPC and TOF detectors (see Tab.4.5 for the momentum ranges). The red empty triangles represent the ALICE results for $\sqrt{s}$ = 7 TeV. They are compared to the results at $\sqrt{s}$ = 200 GeV (star markers, average value of the results from the STAR and the PHENIX Collaboration) and $\bar{p}p$ reactions at $\sqrt{s}$ = 900 GeV (open squares). Some data points are displaced for clarity.

In the lower panel, the mean momentum transverse values extrapolated from the HMPID stand-alone analysis (blue points), are added to the published results (ALICE, pp at $\sqrt{s}$ = 900 GeV and STAR/PHENIX, pp at $\sqrt{s}$ = 200 GeV [94, 93]). Only statistical errors are added. The stand-alone HMPID analysis (Fig.4.21, lower panel, blue points) agrees well with the results from ALICE at $\sqrt{s}$ = 7 TeV for each species (Fig.4.21, upper panel, red empty triangles).

The mean p_t rises very little with increasing $\sqrt{s}$. This result is interesting because this behaviour is not expected due to the fact that spectral shape takes into account increasing contribution from hard processes. Same behaviour was observed to RHIC: the increase in mean p_t at $\sqrt{s}$ = 200 GeV compared to studies at $\sqrt{s}$ = 25 GeV was observed small.

	Lévy function	
Particle	dN/dy	$\langle$ p$_t$ $\rangle$ (GeV/c)
π^+	1.419 ± 0.014	0.499 ± 0.002
π^-	1.454 ± 0.013	0.482 ± 0.002
K^+	0.209 ± 0.012	0.751 ± 0.007
K^-	0.251 ± 0.012	0.708± 0.007
p	0.107 ± 0.009	0.950 ± 0.001
$\bar{p}$	0.104 ± 0.009	0.983 ± 0.001

Table 4.7: *Integrated yield dN/dy, with only statistical errors, and $\langle$ p$_t$ $\rangle$, as obtained from the Lévy function (pp collisions $\sqrt{s}$ = 7 TeV, HMPID spectra) are summarized.*

4.6.2 Ratio: π^-/π^+, K^-/K^+ and $\bar{p}/p$

The ratio of π^-/π^+ and K^-/K^+ as a function of p$_t$ between 1.5 and 3.4 GeV/c is shown in Fig.4.22. The ratios are close to unity within the errors (systematics and statistics). Very similar results have been obtained for π^-/π^+ and K^-/K^+ measurements (performed by the ITS and the TPC) at lower p_t (up to 1 GeV/c).

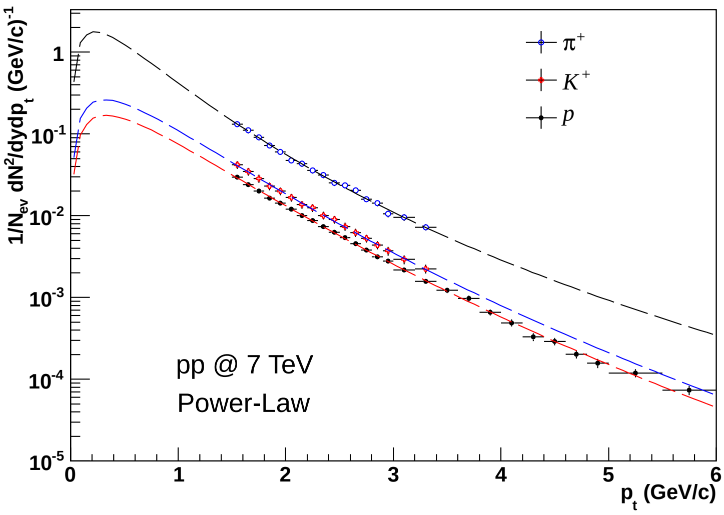

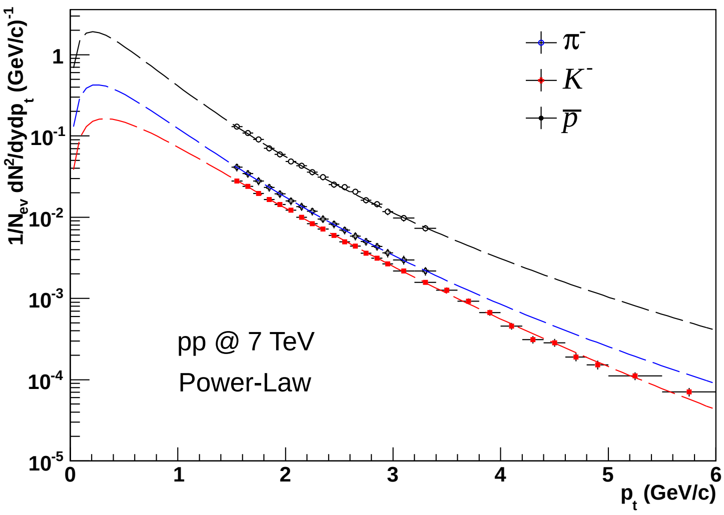

Figure 4.19: *Transverse momentum spectra of positive and negative hadrons for pp collisions at* $\sqrt{7}$ *TeV using the HMPID detector. The curves are fitted using the power law function.*

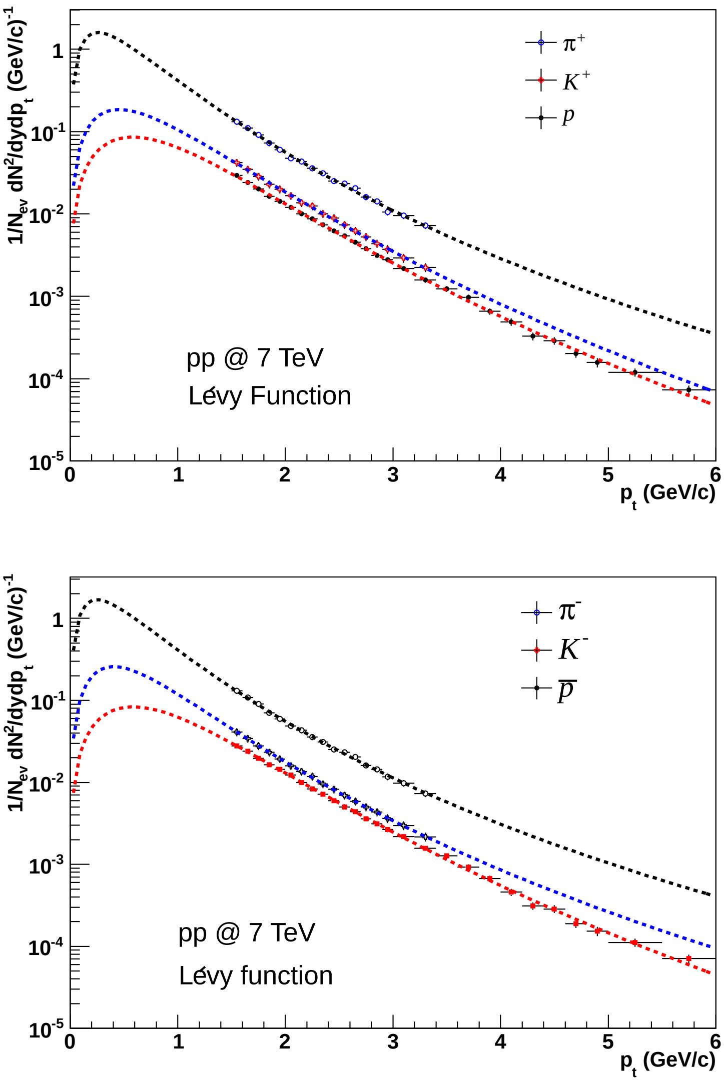

Figure 4.20: *Transverse momentum spectra of positive and negative hadrons for pp collisions at* $\sqrt{7}$ *TeV using the HMPID detector. The curves are fitted using the Lévy function.*

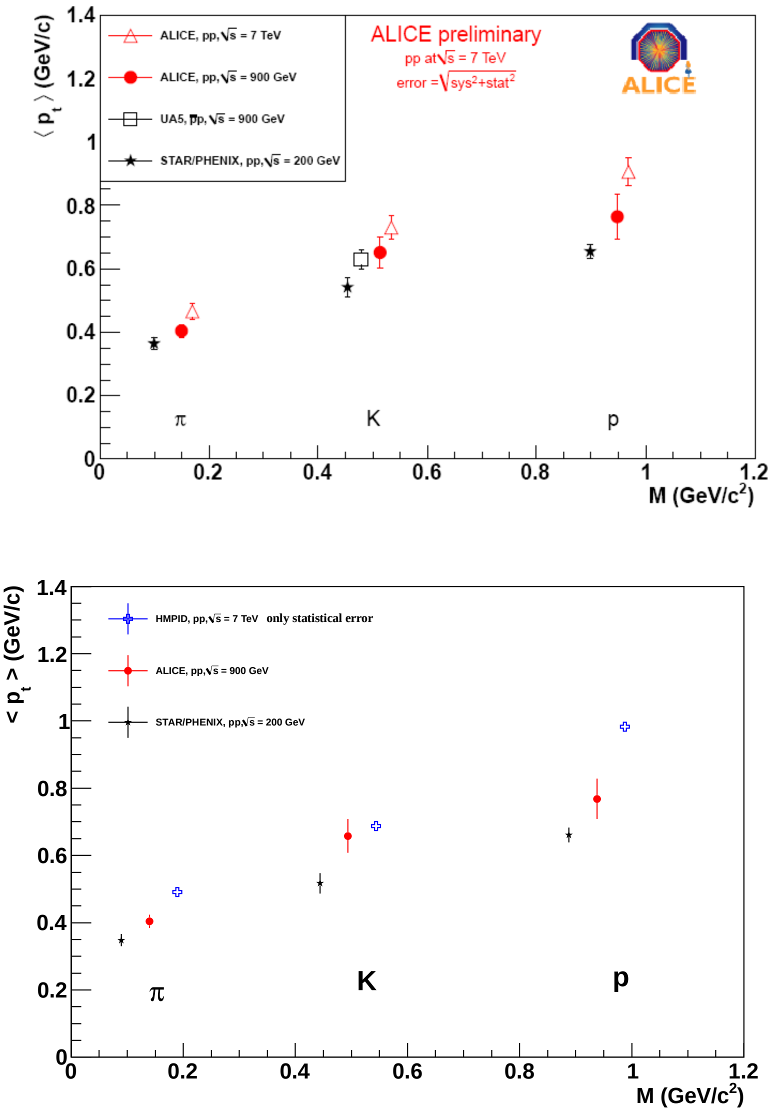

Figure 4.21: *Mean transverse momentum as a function of the mass for pion, kaon and proton. Different collision energies are considered. Upper panel, a recent preliminary result from the ALICE at* $\sqrt{s} = 7$ *TeV. In the lower panel, the HMPID values obtained with the Lévy function are inserted (only statistical error). Some points are displaced for clarity.*

The latter measurement has been carried out in momentum range between 0.45 and 1.05 at 900 GeV and 7 TeV.

The measurement of the antiproton-to-proton ratio is an important probe of the collision dynamics. In particular, it provides information about the transport of the baryon number (BN) [98, 99, 100, 101, 102, 103, 104]. The results obtained from experimental data on soft hadronic processes are understood within a model, the Quark-Gluon String Model (QGSM). This model describes the baryon as a bound diquark-quark state and the break-up of this configuration is the mechanism responsible for the baryon-number transport. Since diquarks retain a large fraction of the proton momentum, they stay close to beam rapidity (within one or two units), so additional processes have been proposed to transport the baryon number over larger distances in rapidity. In particular, via purely gluonic exchanges, where the proton breaks up into three quarks. In this case, the BN resides in a configuration (non-perturbative) of gluon field, called *baryon string junction*, which connects the valence quarks. In this context, the baryon number transport is suppressed exponentially

$$(BN) \propto exp[(a_J - 1)\Delta y], \tag{4.24}$$

where a_J represents the intercept of the junction. At $a_J \sim 0.5$, baryon transport will approach zero with increasing Δy while for $a_J \sim 1$ it will approach a constant and finite value.

The baryon transport mechanism can be probed over very large rapidity intervals measuring the antiproton-to-proton ratio

$$R = \frac{N_{\bar{p}}}{N_p} \tag{4.25}$$

or, the proton-antiproton asymmetry,

$$A = \frac{(N_p - N_{\bar{p}})}{(N_p + N_{\bar{p}})} \tag{4.26}$$

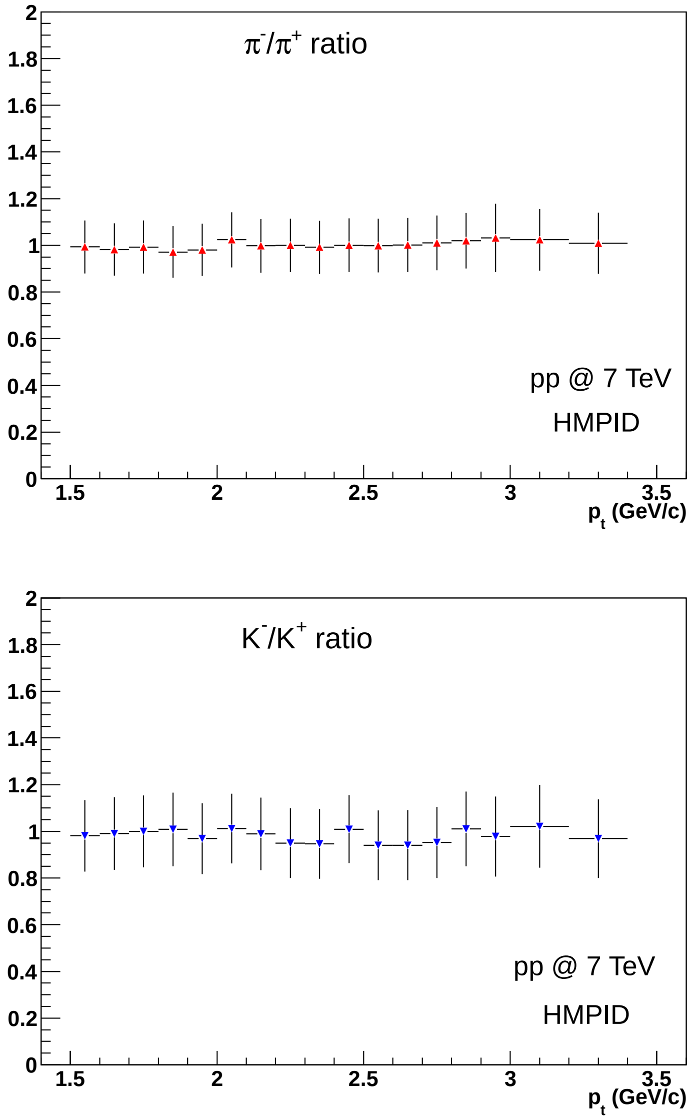

Figure 4.22: *π^-/π^+ and K^-/K^+ ratios as a function of p_t in pp collision at $\sqrt{s}$ = 7 TeV.*

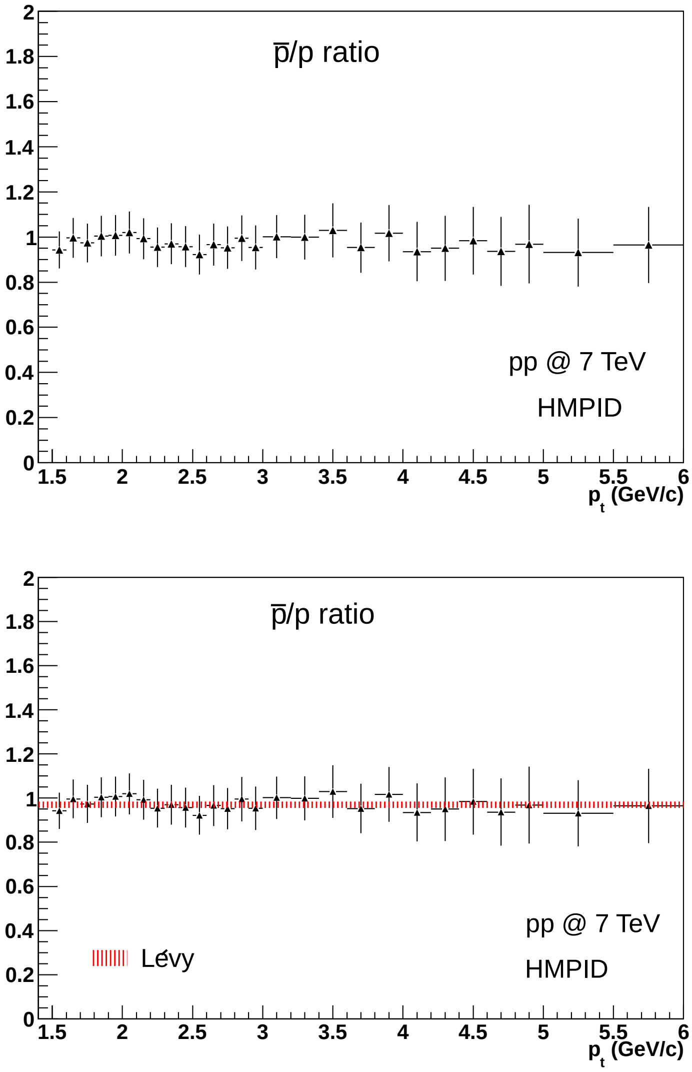

Figure 4.23: *Upper panel: $\bar{p}/p$ ratio as a function of the p_t in pp collisions at $\sqrt{s} = 7$ TeV. Lower panel: the red line represents the antiproton-proton ratio obtained from the Lévy function.*

Most of the proton and antiproton at mid-rapidity are created as baryon-antibaryon pairs. This implies equal yield and R = 1. Any excess of protons over antiprotons is therefore associated with the baryon-number transfer from the incoming beam. The ratio of proton to anti-proton production in the ALICE experiment at $\sqrt{s} = 0.9$ and 7 TeV has been measured[96] using the ITS, TPC and V^0 detector. The measurement has been performed between $0.45 < \mathrm{p}_t < 1.05$, and in $|y| < 0.5$, and the ratio is found to be very close to unity,

$$(\bar{p}/p)_{|y|<0.5} = 0.957 \pm 0.006(stat) \pm 0.014(syst.) \quad at \quad 0.9 \quad TeV \tag{4.27}$$

and

$$(\bar{p}/p)_{|y|<0.5} = 0.991 \pm 0.005(stat) \pm 0.014(syst.) \quad at \quad 7 \quad TeV \tag{4.28}$$

The ratios are independent of both rapidity and transverse momentum, and are fully consistent with the standard picture of the baryon transport. We note that, although the ratio at $\sqrt{s}$ = 900 GeV is close to unity, there is a small excess of protons over antiprotons corresponding to a $p-\bar{p}$ asymmetry of A = 0.022 ± 0.003 (stat.) ± 0.007 (syst.) At $\sqrt{s}$ = 7 TeV, the ratio is consistent with the unity and corresponds to A = 0.005 ± 0.003 (stat.) ± 0.007 (syst.). The latter result sets a limit on the amount of baryon transport over 9 units in rapidity. It is possible to exclude the large value for the asymmetry even at infinite energy, which has been predicted to be A = 0.035 using $\mathrm{a}_J = 1$.
Note that such study has not been carried out in high-energy proton-antiproton colliders (Sp$\bar{p}$S, Tevatron [4]) because of the symmetry of the initial system at midrapidity.

The HMPID detector contributes on this item measuring the antiproton over proton ratio for high p_t (momentum range between $1.5 < \mathrm{p}_t < 6$ GeV/c). Fig.4.23 shows the preliminary ratio obtained from the fully corrected spectra for pp collisions

[4] Tevatron energies: 1.8 TeV and 1.96 TeV. Two detectors: CDF and DZero.

at $\sqrt{s} = 7$ TeV. The errors take into account the statistical and systematic uncertainties. The ratio is compatible with unity and is comparable with the low p_t ratio from ALICE. We can conclude that for high p_t, the ratio is independent from the transverse momentum. In Fig.4.23, lower panel, the value of the ratio obtained from the Lévy functions corresponding to protons and anti-protons (red line) has been overlapped to the data points.

Chapter 5

Charged hadrons identification in p-p collisions at $\sqrt{s} = 2.76$ TeV

5.1 Introduction

The pp data at $\sqrt{s} = 2.76$ TeV allow a direct comparison with the PbPb data [1] at the same energy.

In this chapter, the preliminary results for pp collisions at $\sqrt{s} = 2.76$ TeV collected during 2011, and reconstructed in the middle of the same year are presented: raw hadron spectra (without efficiency correction) and $\pi^-/\ \pi^+$, K^-/K^+, $\bar{p}/p$ ratios. Only the corrections needed for the measurement of the particle ratio have been evaluated. This analysis has been performed using an *improved* tracking algorithm. As explained in the Chapter 2, significant effort has been done to improve the tracking during year 2011. With the new procedure it is possible to exploit the precise knowledge of the HMPID MIP information in the track fitting procedure. Improved tracking information brings the resolution of the Cherenkov angle close to the design values.

[1]PbPb collisions at $\sqrt{s} = 2.76$ have been collected during the 2010 and during the last part of 2011.

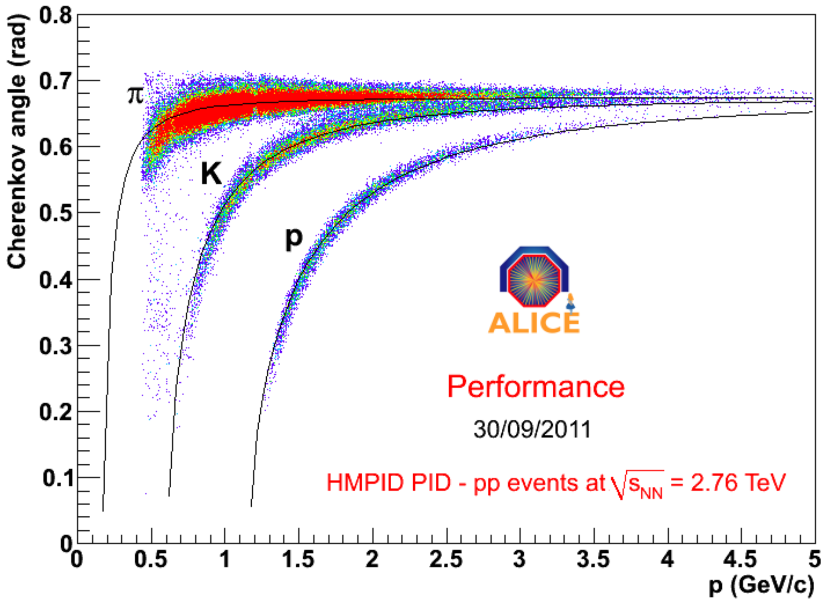

Figure 5.1: *Cherenkov angle distribution as a function of the track momentum in pp collisions at $\sqrt{s}$ = 2.76 TeV is shown. Pion, kaon and proton bands are visible. Theoretical curves are overlapped showing the excellent agreement. Improved tracking information brings the resolution of the Cherenkov angle close to the design value.*

5.2 Data analysis: p_T spectra

Data taking conditions are described in the previous chapter. The same procedure has been followed and the same cuts for event and track selection have been used.

In Fig.5.1 the Cherenkov angle distribution as a function of the track momentum in pp collisions at $\sqrt{s} = 2.76$ TeV is shown. The comparison between standard and improved tracking (Fig.5.1 and the corresponding figure at $\sqrt{s} = 7$ TeV in Chapter 4 - Fig.4.2) clearly shows the improvements in the Cherenkov angle resolution. This allows a cut for the matching selection equal to $d_{MIN} < 5$ cm [2].

[2]Standard tracking: $d_{MIN} < 0.7$ cm.

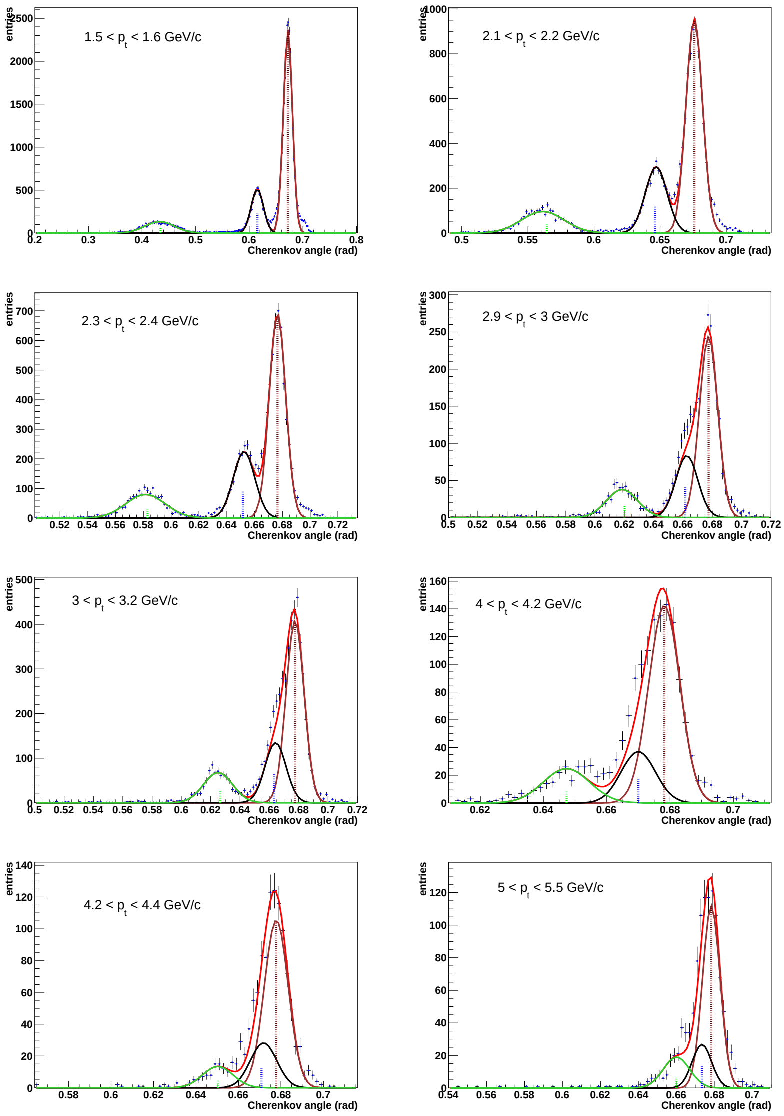

Figure 5.2: *Examples in different* p_t *bins of three-Gaussian fits for negative particles.*

To extract the raw yields, the same procedure as described in the previous chapter was followed. A three-Gaussian fit has been performed in Cherenkov angle distribution in slices of p_t . The same convention on the number and width of the p_t bins has been used. We remark that the statistics available for this analysis consists of 40 M of events. In the fitting procedure, the Cherenkov angle for each species is constrained to vary by 5% around the theoretical Cherenkov angle value, while the resolution and the normalization constant (related to the yield) are assumed to vary by 10 % around the expected values. Some examples of three-Gaussian fits for negative particles are shown in Fig.5.2. The red line represents the global fit, the green line represents the proton distribution, while black and brown lines are the kaon and pion distributions respectively.
In Fig.5.3 the Cherenkov angle is plotted as a function of the track momentum. The points have been obtained from the fits with three-Gaussian functions. The lines (black, red and blue) represent the theoretical curves. The agreement is quite good.

The n-σ separation,

$$separation = \frac{\theta_{Ckov}(i) - \theta_{Ckov}(j)}{(\sigma(i) + \sigma(j))/2} \tag{5.1}$$

with i, j = π, K, p, has been evaluated from the fit parameters: it is shown in Fig.5.4 as a function of p_t. We summarize the main differences between standard and improved tracking here:

- Standard tracking:
  - π/K 2σ-separation up to 3 GeV/c;
  - K/p 3σ-separation up to 4.2 GeV/c;
- Improved tracking:
  - π/K 3σ-separation up to 3.1 GeV/c;

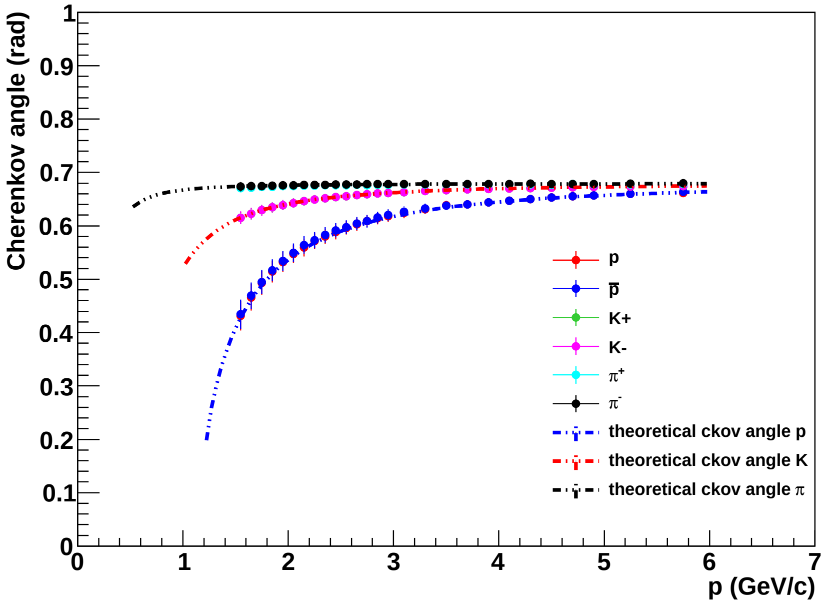

Figure 5.3: *Cherenkov angle as a function of track momentum. The points are obtained from the fitting procedure. The lines represent the theoretical curves.*

– K/p 3σ-separation up to 5.1 GeV/c;

Raw spectra for pion, kaon and proton, normalized to the number of events are shown in Fig.5.5. Kaons and pions yields are evaluated in momentum range $1.5 < p_t < 3$ GeV while proton and anti-proton yields between $1.5 < p_t < 5$ GeV/c. The raw spectra are approved as Performance plot from the ALICE Collaboration.

5.3 Corrections

As mentioned at the beginning of this chapter, only the corrections needed for the measurement of particle ratio have been evaluated namely: the geometrical acceptance, the tracking efficiency, the matching efficiency correction factor, transport code correction and feed down correction).

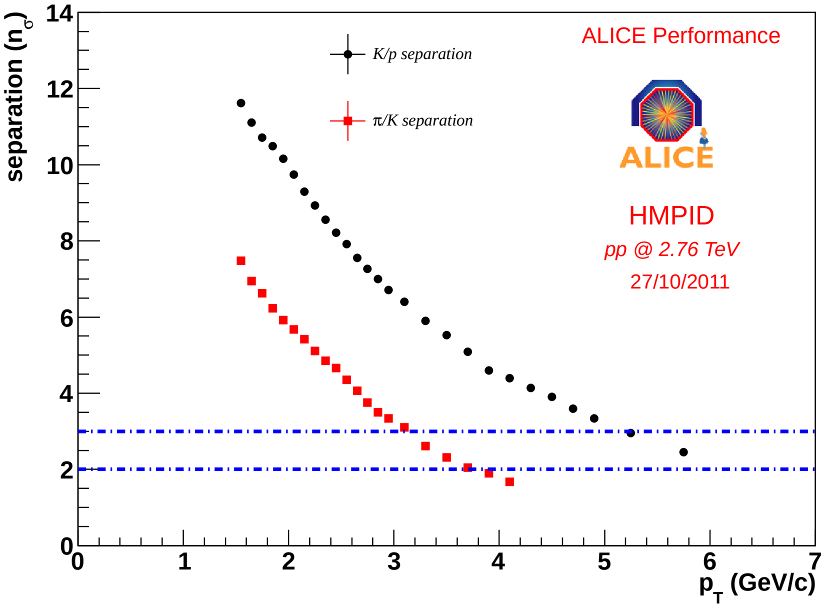

Figure 5.4: *n-σ separation for π/K (red point) and K/p (black point) as a function of the p_t in the HMPID using the improved tracking.*

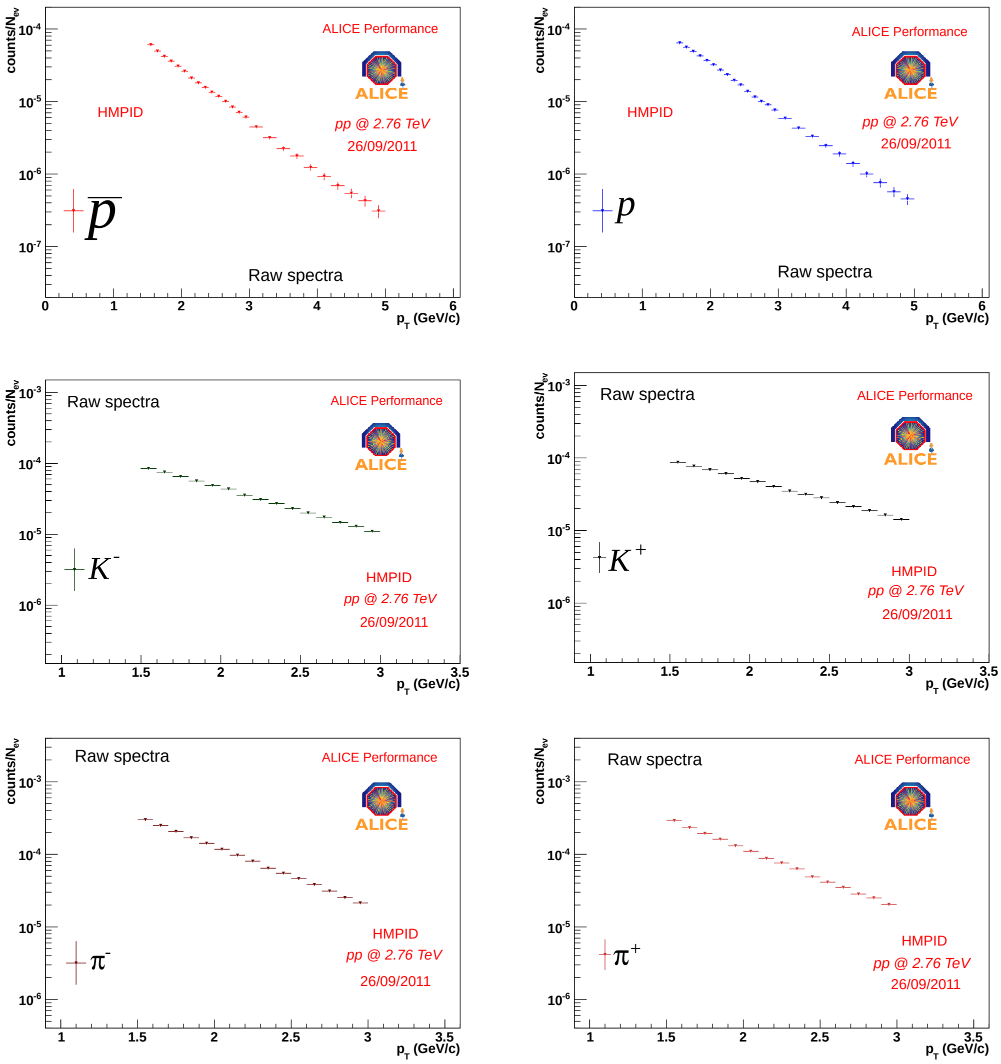

Figure 5.5: *Raw spectra (not corrected for efficiency) for negative and positive particles at* $\sqrt{s}$ = *2.76 TeV.*

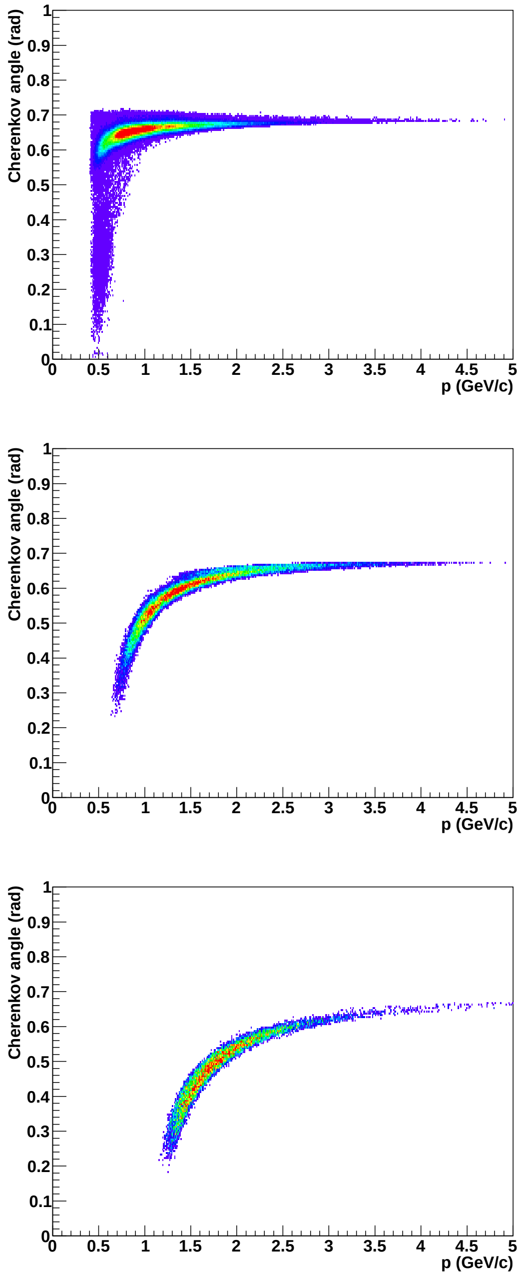

Figure 5.6: *Three selected bands corresponding to pions, kaons and protons. For each track a probability has been assigned.*

The MIP charge correction

$$Correction\ factor_{MIP-charge} = \frac{dN/dp_t^{Q>150}}{(dN/dp_t)_{tot}} \tag{5.2}$$

is estimated to be less than 1%, so it is negligible.

The geometrical acceptance and tracking efficiency are evaluated together using Monte Carlo simulation (20 M of events). We define geometrical and tracking efficiency in the same way explained in the previous chapter:

$$Eff_{traking} = \frac{(dN/dp_t)_{reconstructed}}{(dN/dp_t)_{generated}} \tag{5.3}$$

$$Acc_{HMPID} = \frac{(dN/dp_t)_{HMPID}}{(dN/dp_t)_{reconstructed}} \tag{5.4}$$

The convolution of tracking efficiency and geometrical acceptance has been evaluated:

$$Eff = Eff_{tracking} \times Acc_{HMPID} \tag{5.5}$$

For the evaluation of the matching efficiency ($d_{MIN} < 5$ cm) the same procedure described in the previous chapter was followed:

- selection of three clean sample of pions, kaons and protons using the PID (assigning a probability for each track). In Fig.5.6 the three bands selected (positive particles) are shown;
- evaluation of the correction faction (ratio between the number of tracks after the selection and the total tracks in the HMPID acceptance):

$$Correction\ factor_{matching} = \frac{dN/dp_t^{d_{MIN}<d_{CUT}}}{(dN/dp_t)_{tot}} \tag{5.6}$$

In Fig.5.7 (upper panel) the distribution of the distances (d_{MIN}) selected for $p_t >$ 1.5 GeV/c is shown: black line represents the proton distribution, while blue and red lines represent kaon and pion distributions respectively. In the lower panel, the distributions are scaled to each other to allow the comparison. The curves are peaked at the same values and nearly identical, so that it is possible to use a common correction factor for the three species. For each sub-range of p_t, the correction factor (defined in the previous chapter) has been evaluated. Fig.5.8 shows the correction factor for positive (blue points) and negative particles (black points).

Transport code correction. For this preliminary analysis, we assumed that the correction for 7 TeV is still valid for $\sqrt{s} = 2.76$ TeV.

Feed-down correction:

$$Correction\ factor_{feed-down} = \frac{(dN/dp_t)_{(weak\ decay)} + (dN/dp_t)_{(material)}}{(dN/dp_t)_{(tot\ =\ primary\ +\ weak\ decay\ +\ material)}} \quad (5.7)$$

As for $\sqrt{s} = 7$ TeV the estimate of this factor is carried out using the Monte Carlo simulation. In the first step, the DCA distribution for all the tracks in Monte Carlo and data is evaluated. Using the MC information, the DCA distribution for primary tracks, for secondary tracks coming from interaction with the material and for secondary tracks coming from the weak decays are evaluated. The templates are used to fit the data distributions. The correction factor is in agreement with the results obtained at $\sqrt{s} = 7$ TeV.

5.4 Results on particle ratios

In Fig.5.9 the preliminary results are presented on $\pi^-/\ \pi^+$, K^-/K^+ and $\bar{p}/p$ ratios in momentum range $1.5 < p_t < 3$ GeV/c for pions and kaons and $1.5 < p_t < 5$ GeV/c. Only the statistical errors are shown. The pions and kaon ratios are close to the unity as expected. The anti-proton proton ratio also close to one independent by of both rapidity and transverse momentum, is consistent with the standard picture of the baryon transport.

We remark that the measurements performed at $\sqrt{s} = 2.76$ TeV will allow the comparison with the results in PbPb collisions at same energy. The good performance due to the improved tracking allows an analysis with 40 M of events. The result is quite satisfactory but further checks are necessary.

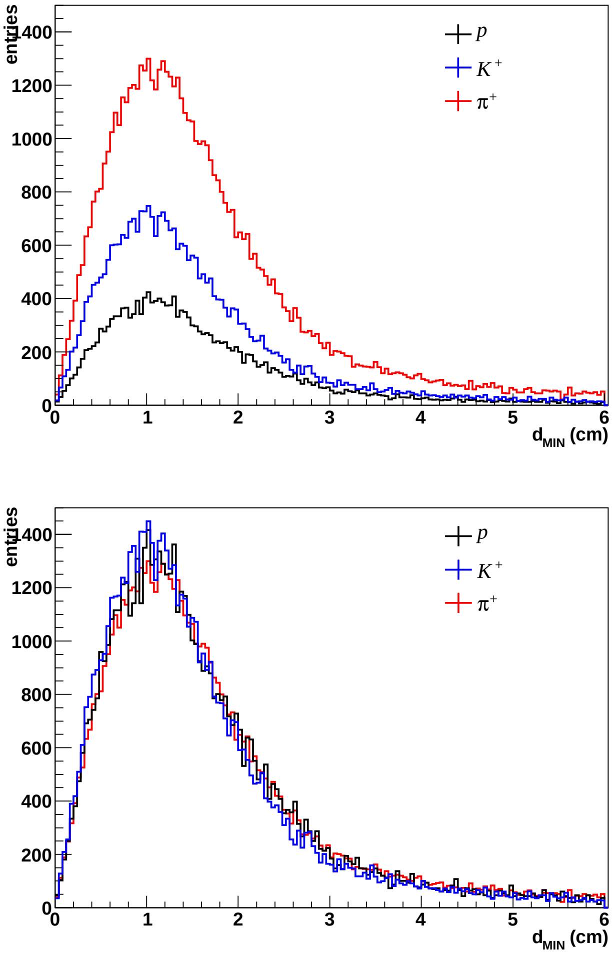

Figure 5.7: *Upper panel: d_{MIN} distributions for positive particles. Black line represents the proton distribution, while blue and red lines represent kaon and pion distributions respectively. Lower panel: the same distributions have been scaled to allow the comparison each other.*

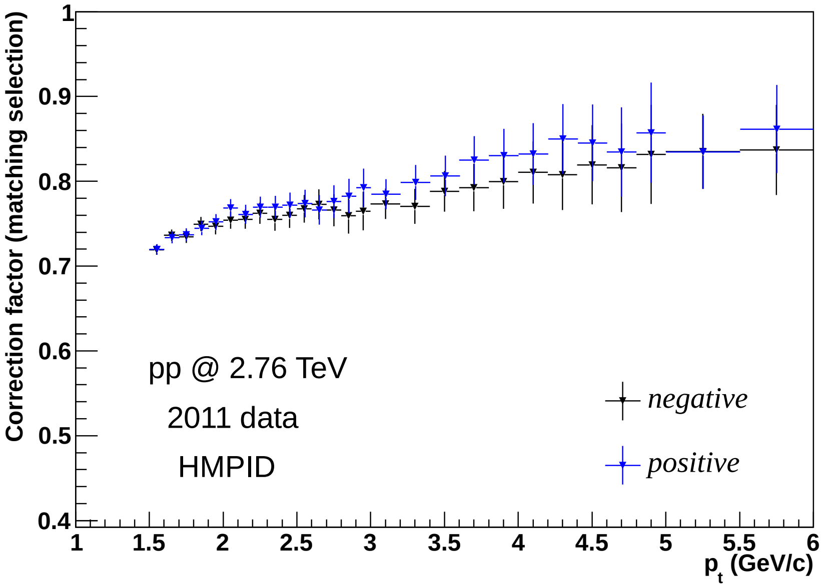

Figure 5.8: *Correction factors for positive and negative particles for each p_t sub-range.*

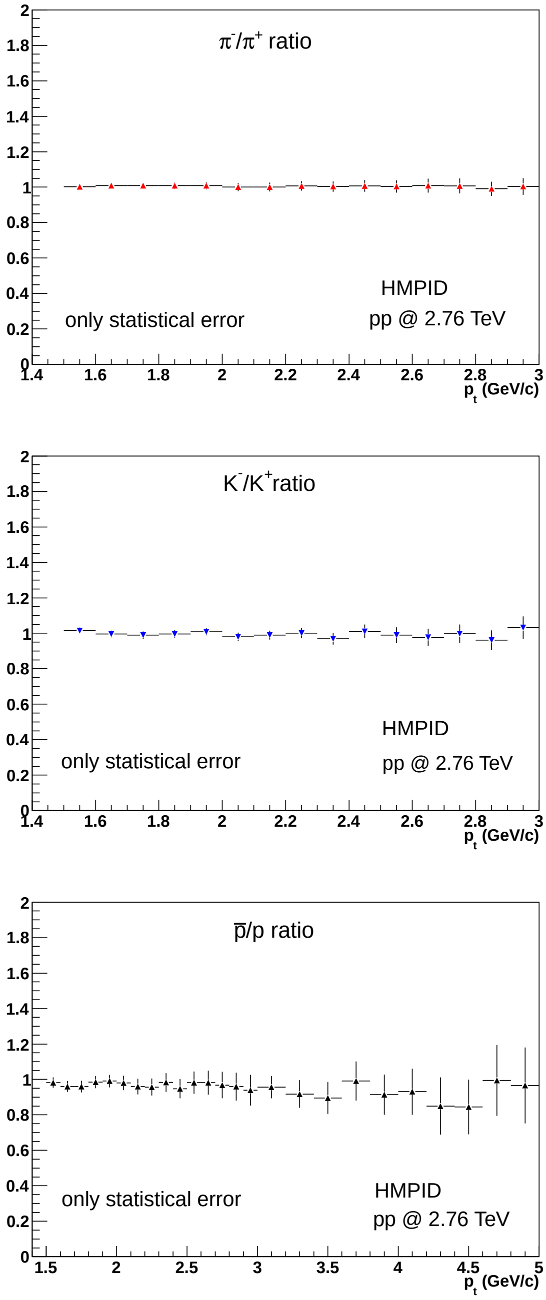

Figure 5.9: *Preliminary particle ratios are shown. All the corrections needed have been evaluated. Momentum range:* $1.5 < p_t < 3$ *GeV/c for pions and kaons, between* $1.5 < p_t < 5$ *GeV/c for protons.*

Conclusion and Outlook

The aim of this thesis is the measurement of the transverse momentum spectra and ratios for identified particles in proton proton collisions at $\sqrt{s} = 7$ TeV. They are the first physics results obtained exploiting the ALICE - HMPID detector, a small geometrical acceptance Cherenkov counter, installed in 2006, and located at 5 m from the interaction vertex. I developed, tested and optimized a general method to perform such a study on pp collisions at $\sqrt{s} = 7$ TeV and used it to obtain preliminary results at $\sqrt{s} = 2.76$ TeV. A three-Gaussian fitting algorithm to extract the pion, kaon and proton yields has been developed and tested. Different fitting procedures have been tested and different frameworks (ROOT and RooFit) have been compared. During the analysis work, I tested several cuts taking into account that tight cuts improve the resolutions, but at the same time, reduce the number of events available for the analysis at higher p_t. I have calculated all the correction factors for the raw yields. The PID efficiency (Chapter 3) has been evaluated using the V^0 decay. This study allowed to appreciate the HMPID capability of Particle IDentification and represents a good reference for Monte Carlo simulation. Moreover, it provided a measurement of the refractive index of the HMPID radiators (necessary for a good understanding of the detector response). In addition, I evaluated the correction factor for the matching selection, the tracking efficiency, the HMPID geometrical acceptance, feed down correction factor and transport code correction. Also, the systematic uncertainties have been evaluated. The corrected spectra and particle ratios are measured and the results are discussed and compared with other experiments at different energies. Almost 600 M events (taking into account data at $\sqrt{s}$ = 7 TeV, data at $\sqrt{s}$ = 2.76 TeV, MC for the trigger study, MC and data for the corrections) have been analyzed.

The preliminary data analysis in pp collisions at $\sqrt{s}$ = 2.76 TeV has been presented (Chapter 5). The analysis is ongoing, but preliminary results (particle ratios) show good agreement with the expected values. Raw spectra (not corrected for the efficiency) are also presented.

The results obtained in Chapter 4 (and in Chapter 5) will be included in the ALICE paper on transverse momentum spectra using ITS, TPC, TOF and HMPID (publication for next year - 2012). Preliminary comparisons in common momentum regions shown a very good agreement.

Note: the figures with the ALICE logo have been approved as Performance plots from the ALICE Collaboration. The other figures are not yet approved.

Appendix A

Kinematic variables

A particle, with the energy E, the rest mass m_0, and the momentum $\overrightarrow{p}$, is described by its four-momentum

$$P = (E, \overrightarrow{p}) = (E, p_x, p_y, p_z) \tag{A.1}$$

The Mandelstam [114] variables (relativistic invariant) are used to describe

$$1 \; + \; 2 \; \rightarrow \; 3 \; + \; 4 \tag{A.2}$$

particle reactions, and are defined:

$$s = (P1 + P2)^2 = (P3 + P4)^2, \tag{A.3}$$

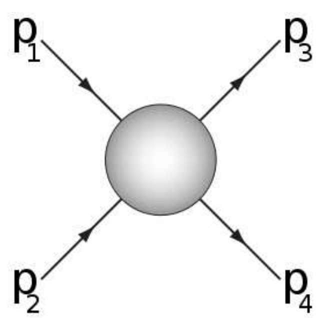

$$t = (P1 - P3)^2 = (P2 - P4)^2, \tag{A.4}$$

$$u = (P1 - P4)^2 = (P2 - P3)^2. \tag{A.5}$$

where the second part of each equation comes from the energy and momentum conservation:

$$P1 + P2 = P2 + P3 \tag{A.6}$$

s represents the square of the total energy of the collision in the center-of-mass of the colliding particles. t is the square of the momentum transfer in the reaction 1 to 3, or 2 to 4. u is the square of the momentum transfer in the reaction 1 to 4, or 2 to 3. It can be shown that

$$s + t + u = m_1^2 + m_2^2 + m_3^2 + m_4^2 \tag{A.7}$$

Thus s + t + u = 0 for massless particles.

The momentum of a particle is divided into its longitudinal momentum p_L and transverse momentum p_T:

$$p_L = pcos\theta = p_z \tag{A.8}$$

$$p_T = psin\theta = \sqrt{p_x^2 + p_y^2} \tag{A.9}$$

only the transverse momentum is invariant under Lorentz transformation. We define the *rapidity* y as

$$y = \frac{1}{2} ln \left(\frac{E + p_L}{E - p_L} \right)$$

where E = $\sqrt{p^2 + m^2}$. The rapidity depends to the particle mass. This means that to determinate the rapidity is necessary to know the energy. E cannot be easily measured without determining the particle type. The quantity, independent to the particle mass is the *pseudorapidity* η:

$$\eta = -ln \left(tan \left(\frac{\theta}{2} \right) \right)$$

where θ increases from z ($\theta = 0$) passing the x-y plane ($\theta = \pi/2$) to -z ($\theta = \pi$). It is valid:

$$\eta = -ln\left(tan\left(\frac{\theta}{2}\right)\right) = \frac{1}{2}ln\left(\frac{|\bar{p}| + p_L}{|\bar{p}| - p_L}\right)$$

in the case E $\gg m_0$. For ultra-relativistic particles the rapidity y approaches the pseudorapidiy η.

It is important to remember that the transverse momentum and the rapidity intervals are invariant under Lorentz transformations. We consider a boost along z:

$$\begin{pmatrix} E' \\ P'_x \\ P'_y \\ P'_z \end{pmatrix} = \begin{pmatrix} \gamma & 0 & 0 & \pm\beta\gamma \\ 0 & 1 & 0 & 0 \\ 0 & 0 & 1 & 0 \\ \pm\beta\gamma & 0 & 0 & \gamma \end{pmatrix} \begin{pmatrix} E \\ P_x \\ P_y \\ P_z \end{pmatrix}$$

la rapidity in the new reference system become:

$$y = -ln\left(\frac{E - P_z}{E + P_z}\right) \rightarrow y' = -ln\left(\frac{E' - P'_z}{E' + P'_z}\right)$$

substituting the transformation to the components:

$$y' = -ln\left(\frac{E' - P'_z}{E' + P'_z}\right) = -ln\left(\frac{E - P_z}{E + P_z}\right) - ln\left(\frac{1 \pm \beta}{1 \pm \beta}\right) = y - ln\left(\frac{1 \pm \beta}{1 \pm \beta}\right) \quad \text{(A.10)}$$

where β = v / c and $\gamma = 1 \ / \ \sqrt{1 - \beta^2}$. this means that Δ y' = Δ y or dy' = dy.

Appendix B

The ALICE coordinate system

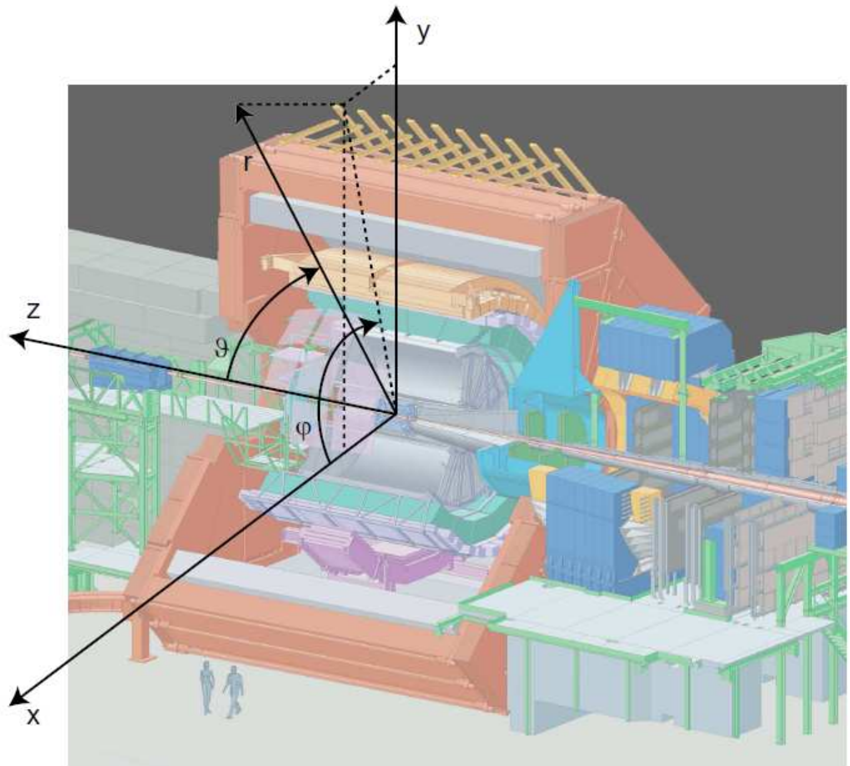

Figure B.1: *The ALICE coordinate system.*

The coordinate system of ALICE defines:

- the point of origin x = y = z = 0 at the nominal interaction point;
- the x-axis perpendicular to the mean local beam direction, aligned with the local horizontal plane of the LHC and pointing to the accelerator center. Positive x is from the point of origin toward the accelerator centre, negative x is from the point of origin outward;
- the y-axis perpendicular to the x-axis and the mean local beam direction, pointing upward; Positive y is from the point of origin upward, negative y is from the point of origin downward;
- the z-axis parallel to the mean local beam direction. An observer looking to positive z has the accelerator center on the left. The muon arm is at negative z;
- the polar angle θ which increases from z ($\theta = 0$) passing the x-y plane ($\theta = \pi/2$) to -z ($\theta = \pi$). At $\theta = \pi/2$ the rapidity y is 0; this is called $mid-rapidity$;
- the azimuthal angle ϕ which increases clockwise from x ($\phi = 0$) passing y ($\phi = \pi/2$) to x ($\phi = 2\pi$) with the observer standing at negative z and looking towards the point of origin.

Appendix C

The Armenteros-Podolanski Plot

Let's consider the kinematics of the decay of a neutral V^0 candidate in two charged particles. We consider this system in both the laboratory system (in which measurements are made) and in the centre of mass system (in which the V^0 is at rest and consequently the two charged particles must come off back-to-back so as to conserve momentum).

In the center of mass system the transverse and longitudinal momenta relative to the direction in which the V^0 was moving in the laboratory system, are defined as

$$q_T^* = p^* sin\theta^* \tag{C.1}$$

$$q_L^* = p^* cos\theta^* \tag{C.2}$$

where all the quantities in the centre of mass system are denoted by *. The use of the Lorentz transformations allows to express these variables in the laboratory system:

$$\begin{pmatrix} E \\ p_x \end{pmatrix} = \begin{pmatrix} \gamma & \beta\gamma \\ \beta\gamma & \gamma \end{pmatrix} \begin{pmatrix} E^* \\ p_x^* \end{pmatrix}$$

where $\beta = v/c$, v is the velocity of the particle, c is the speed of light and $\gamma = 1/\sqrt{1-\beta^2}$. Expanding the Lorentz transformation, it will give a definition of q_L in

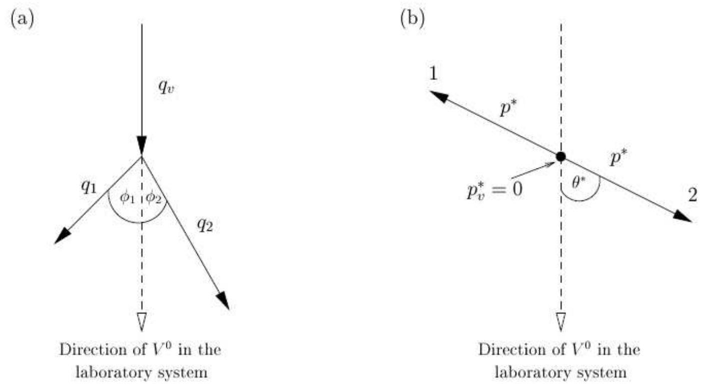

Figure C.1: *The decay of a neutral V^0 decays into two charged tracks in (a) the laboratory system and (b) the center of mass system.*

terms of

$$q_L = \gamma\beta E^* + \gamma q_T^* \tag{C.3}$$

and substituting the eq.C.2 in eq.C.3 we obtain

$$q_L = \gamma\beta E^* + \gamma p^* cos\theta^*. \tag{C.4}$$

Since, transverse momentum is Lorentz invariant,

$$q_T = q_T^* = p^* sin\theta^* \tag{C.5}$$

The Armenteros α variable is defined as

$$\alpha = \frac{q_L^+ + q_L^-}{q_L^+ + q_L^-}. \tag{C.6}$$

Using the eq.C.3, assuming particle 1 is the positively charged particle and particle 2 is the negatively charge one, we obtain

$$\alpha = \frac{\gamma\beta(E_1^* - E_2^*) + 2\gamma p^* cos\theta^*}{\gamma\beta(E_1^* + E_2^*)}. \tag{C.7}$$

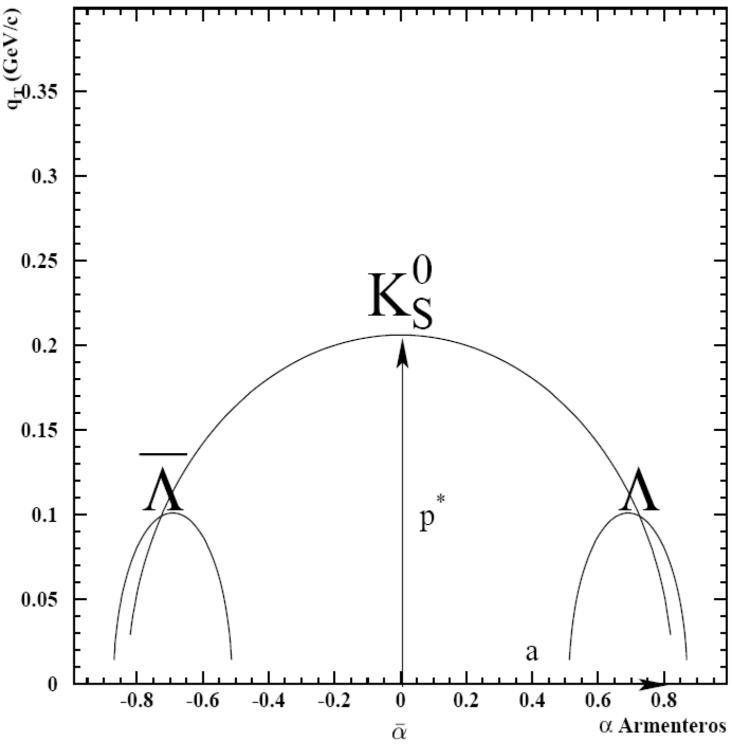

Figure C.2: *The Armenteros-Podolanski plot showing the K_S^0 , $\bar{\Lambda}$ and Λ half ellipses. Also marked are the parameters p^*, a and $\bar{\alpha}$ for the K_S^0.*

It is valid, in the centre of mass system,

$$E^* = E_1^* + E_2^* \tag{C.8}$$

where $E^2 = p^2 + m^2$, E^*, E_1^*, E_2^* and $E^* = m_v$. The eq.C.7 becomes

$$\alpha = \frac{(E_1^* + E_2^*)}{m_v} + \frac{2p^* cos\theta^*}{m_v}. \tag{C.9}$$

We define the variables $\bar{\alpha}$ and a:

$$\bar{\alpha} = \frac{(E_1^* + E_2^*)}{m_v} \tag{C.10}$$

$$a = \frac{2p^*}{m_v} \tag{C.11}$$

then,

$$\alpha = \bar{\alpha} + acos\theta^* \tag{C.12}$$

and, using the trigonometrical relationship, we obtain,

$$(\frac{\alpha - \bar{\alpha}}{a})^2 + (\frac{q_T}{p^*})^2 = 1 \tag{C.13}$$

which is the equation of an ellipse.

Appendix D

Trigger study in p-p events for the HMPID detector

The HMPID detector, with low geometrical acceptance (- 0.6 $< \eta <$ 0.6 and $\approx$ 60^0 azimuthal coverage), covers $\approx$ 5 % of the TPC detection volume. A preliminary study of a topological trigger in p-p events for the HMPID has been carried out [1]. The aim of this study is to understand, by means of simulation (Monte-Carlo), if the implementation of a topological trigger using the two innermost layer of the Inner-Tracking-System and the Time-Of-Flight detector can reject events which are not interesting for the HMPID (events without any tracks in the HMPID). Moreover, the trigger should not introduce a bias in the kinematic variables. The advantages are numerous, for example, a dedicated trigger could reduce the high number of events to analyze: almost 200 M events are used for the current analysis for the evaluation hadrons spectra. Moreover, it could be possible to use the detector for PID (with

[1] "Study of a trigger in p-p events for the HMPID detector in the ALICE experiment at LHC" F. Barile for the ALICE Collaboration contribution for proceedings of "12th Topical Seminar on Innovative Particle and Radiation Detectors (IPRD10)",
Siena - Italy, 7 - 10 June 2010
Published in Nucl.Phys.Proc.Suppl.215:215-217,2011.

specific and optimized cuts) in higher momentum ranges, where the statistics is very low. The systematic uncertainties due to several data periods [2] could be reduced. The use of a trigger [88] allows fast performance checks (alignment, calibration) selecting clean samples of data. This appendix has been organized in the following way: in the first part, a description of the detectors used in the analysis, the event generation and the description of the trigger. In the last part, the trigger performance and the conclusions are discussed.

Trigger [86] is an electronic system which makes a decision whether the collision is worth to save or not. The input to the trigger is represented by triggering detectors which send the signal to the trigger when the collision occurs. The output from the trigger is represented by readout detectors which detect the collision. The basic scheme for the signal propagation is:

$$triggering\ detector\ \ -> \ \ trigger\ \ -> \ \ readout\ detector$$

where triggering detectors can be also readout detectors [3]. The trigger system consists of numerous parts. Two basic parts are:

- Central Trigger Processor (CTP) which is the decision maker;
- Local Trigger Unit (LTU) which works as an interface between readout detector and CTP.

LTUs are the same for all detectors. Summarizing:

$$triggering\ detector\ \ - \ \ trigger\ input\ \ ->$$

[2]For example, LHC10d, LHC10b, LHC10c used in the last chapters for the analysis. Several periods in the analysis could mean different experimental conditions during the data taking.

[3]The signals from triggering detectors to the trigger are called *trigger inputs*. Signals from trigger to readout detectors are called *signals* or simply *triggers* and sometimes they are called also *trigger signals*.

$$CTP \;-\; trigger\ signal \; -> LTU \; -> readout\ detector$$

The ALICE trigger is a 3-level trigger system. It can have 3 consecutive trigger inputs - L0, L1 and L2 and 3 consecutive signals (or triggers) - also L0, L1 and L2. 3-level trigger is a consequence of the different event processing speed of the various detectors.

D.1 Data Analysis

D.1.1 Trigger strategy

How can the SPD Fast-OR signal and the Time-Of-Flight be used to a useful topological trigger for the HMPID ?
The basic idea is to evaluate the SPD chips and the TOF-plates in the HMPID acceptance using Monte-Carlo simulation. The study can be divided in two main steps. In the first step, a track generation on the HMPID detector had been done recording the SPD chips and TOF plates in the HMPID acceptance. In the second step, the evaluation of the trigger performance using pp collisions has been carried out.

D.1.2 Main detectors used for the analysis

D.1.2.1 General remarks on SPD Fast-OR

The ITS [7][8], as described in the Chapter 2, consists of six cylindrical layers of silicon detectors with radii of 3.9/7.6 cm (Silicon Pixel Detector), 15.0/23.9 (Silicon Drift Detector) and 38/43 cm (Silicon Strip Detector). The Silicon-Pixel-Detector (SPD) constitutes the two innermost layers of the ITS. The basic building block of the SPD is a module consisting of 5 chips. Two modules are mounted together along the z direction to form a 141.6 mm long half-stave. A stave is made of two

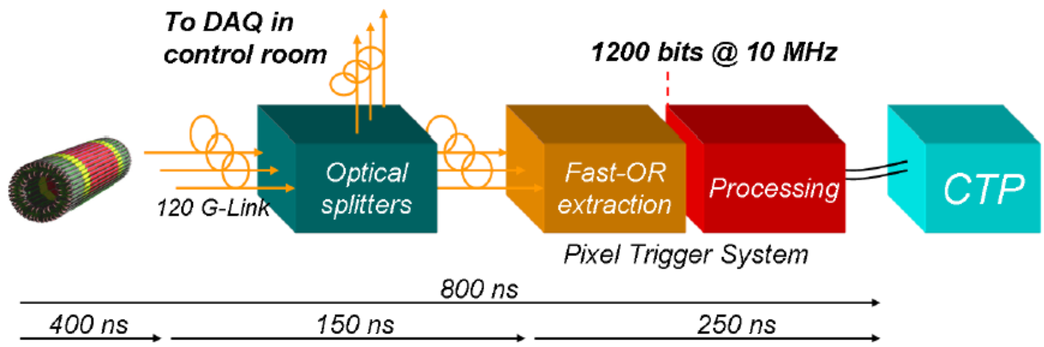

Figure D.1: *Pixel trigger system architecture.*

mirrored halfstaves. In total, the SPD includes 60 staves, consisting of 240 modules with 1200 readout chips for a total of 9.8×10^6 cells. A unique feature of the SPD is its capability to generate a prompt trigger based on an internal Fast-OR. Each pixel chip provides a Fast-OR digital pulse when one or more of the pixels in the matrix are hit. The Fast-OR signals of the 10 chips on each of the 120 half-staves are read by the PILOT chip and transmitted every 100 ns on the 120 optical links that are also used for the data readout. The pre-processed Fast-OR data can be used to contribute to the Level 0 trigger decision in the ALICE Central Trigger Processor (CTP). This feature is very useful in particular in the case of events with very low multiplicities in pp runs and in fact various trigger algorithms including the Fast-OR are being investigated showing that background rejection in pp interactions and event selection in heavy-ions runs is significantly improved by using the Fast-OR information in the L0-trigger decision. The pixel trigger signal generated by the Fast-OR processor must reach the CTP within about 800 ns of the interaction in order to meet the latency requirements of the L0-trigger electronics. The Fast-OR output is synchronized with the 10 MHz pixel system clock, this means that the signal is integrated over 100 ns corresponding to 1 bunch-crossing in the case of operation with heavy ions, or 4

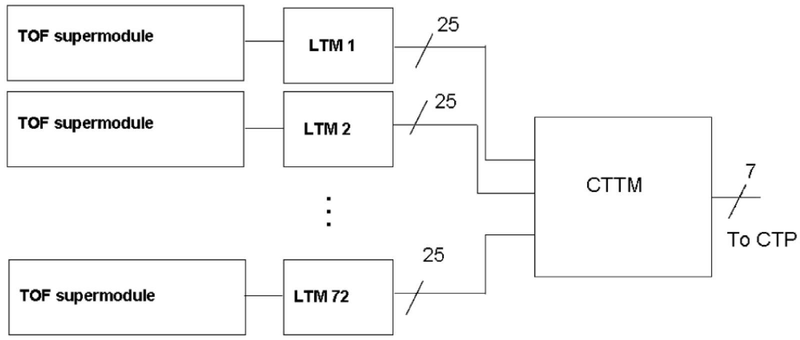

Figure D.2: *Sketch of the TOF trigger.*

consecutive bunch-crossings in pp operation [4]. All 120 half-staves are synchronized to the same integration period covering the same set of bunch-crossings in order to limit this ambiguity when all Fast-OR signals are simultaneously processed and to minimize the latency. In the ALICE trigger system, the bunch-crossing ambiguity can be resolved by considering the coincidence between the pixel trigger signal and the ALICE V0 detector signal. The pixel trigger system architecture is shown in Fig. D.1. For this study, the Fast-OR represents the optimal choice to select clean sample of events for the HMPID detector.

D.1.2.2 TOF and L0 trigger

The Time-Of-Flight detector [7][8] covers a cylindrical surface of polar acceptance $|\theta - 90°| < 45^0$. It has a modular structure corresponding to 18 sectors in ϕ (the azimuthal angle) and to five segments in z (the longitudinal coordinate along the beam axis). The basic unit of the TOF system is an MRPC strip 1220 mm long and 130 mm wide, with an active area of 1200×74 mm^2 subdivided into pads of 35×25 mm^2. Five modules of three different types are needed to cover the full cylinder along the z direction. They all have the same structure and width (128 cm)

[4]The basic time unit for (almost) all electronics in ALICE and in LHC is 25 ns or one bunch crossing (BC) - it is a time distance between two bunches of protons.

but differ in length. Taking advantage of the MRPC, the TOF detector provides very fast signals with low noise. The idea is to use the information from this large area with about 157,000 channels for a fast estimate of the event track multiplicity. The signals from the detector are available in a short time (< 1 ns) so that the TOF trigger [87] can contribute to the ALICE L0 trigger decision. The ionization taking place in the gas volume of the MRPC produces a signal, which is picked up by 96 pads, each of 8.8 cm^2 area. One supermodule is equipped at each end with two 9 U VME crates and covers an azimuthal angle of 20^0. The architecture of the TOF trigger uses a first layer of 72 VME (9 U) boards, called Local Trigger Module (LTM), housed in these crates. Four LTMs are needed to process the data produced by one supermodule. The LTMs act as an interface between the front-end electronics and the trigger board, called Cosmic and Topology Trigger Module (CTTM), made of a single, large size board, which will handle the information from the 72 LTMs (Fig.D.2). The TOF detector can be a good candidate for this study (note that, TOF and HMPID are very close and this allow a track selection dedicated to high momenta).

D.1.3 Event generations

To perform this study, two samples of events have been generated. About 800K tracks (protons and antiprotons at B = 0.5 T and momentum between 1 - 10 GeV/c) have been generated in the acceptance of the HMPID (see Fig.D.3, upper panel) and 100 K pp collisions at $\sqrt{s}$ = 7 TeV to evaluate the trigger performance. The simulation has been executed in the AliRoot framework. To simulate the particle interaction with matter, the programm GEANT3, interfaced with AliRoot, has been used. The analysis has been carried out using different levels of data information generated by AliRoot (as explained in the Chapter 2). For the chip selection, the objects of the AliTrackReference classes have been used. It is are applied to retrieve the position of simulated particles at given location of interest (e.g. when the particle enters or exits a detector or it decays). The Event Summary Data (ESD) are used to read Fast-OR signals. The signal produced from the track on the TOF (for plates determination) and on the HMPID detector are stored at the Digits level.

D.1.4 SPD Chips selection

A track produces a signal on the detector during its passage. The SPD detector is the first detector closest to the primary vertex, so, if the track crosses the HMPID chamber, it is possible to understand which SPD chip has been fired. To obtain such information it is necessary to follows this sequence:

$$Layer \ \ -> \ \ Module \ \ -> \ \ Chip$$

In Fig.D.3, upper panel, ITS and HMPID 2D cut views along the xy direction are shown: each point corresponds to the “track reference” point released on the detectors. The “track reference” points can give all the useful track information needed for this analysis (x, y, z, θ, ϕ). The selection of the SPD layers has been performed by a distance cut:

$$d_{vtx-P} = \sqrt{(x_v - x_p)^2 + (y_v - y_p)^2 + (z_v - z_p)^2} \tag{D.1}$$

where vtx(x_v, y_v, z_v) and P(x_p, y_p, z_p) are the primary vertex coordinate and the coordinate signal on the SPD layers respectively. The distance between the primary vertex and the signal released to the detectors has been evaluated: the distance distribution for all the tracks on the ITS layers is shown in Fig.D.3. The peaks correspond to the six ITS layers. Since the target is to accept only points coming from the innermost layer of the ITS, the following cuts are applied:

$$0 < d_{vtx-P} < \ \ 4.5 \ cm \ \ -> \ \ SPD \ \ Inner \ \ Layer \tag{D.2}$$

$$4.6 < d_{vtx-P} < \ \ 10 \ cm \ \ -> \ \ SPD \ \ Outer \ \ Layer \tag{D.3}$$

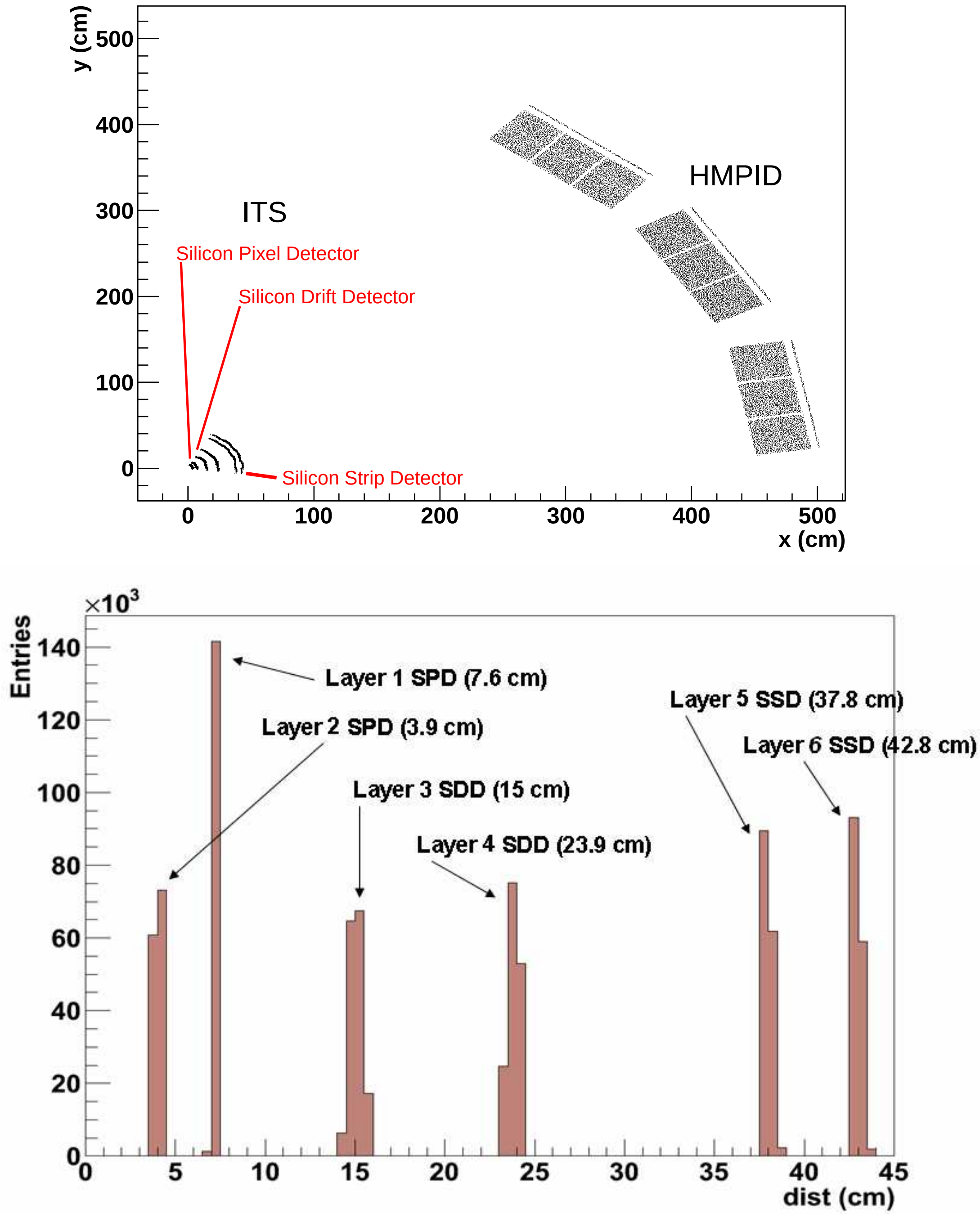

Figure D.3: *Upper panel: ITS and HMPID 2D cut views along the xy direction. Each point represents the track signal in the detector: the six ITS layers and the HMPID are clearly visible. Lower panel: the distance (primary vertex - signal track in the ITS layers) distribution for the six peaks corresponding to the ITS layers are shown.*

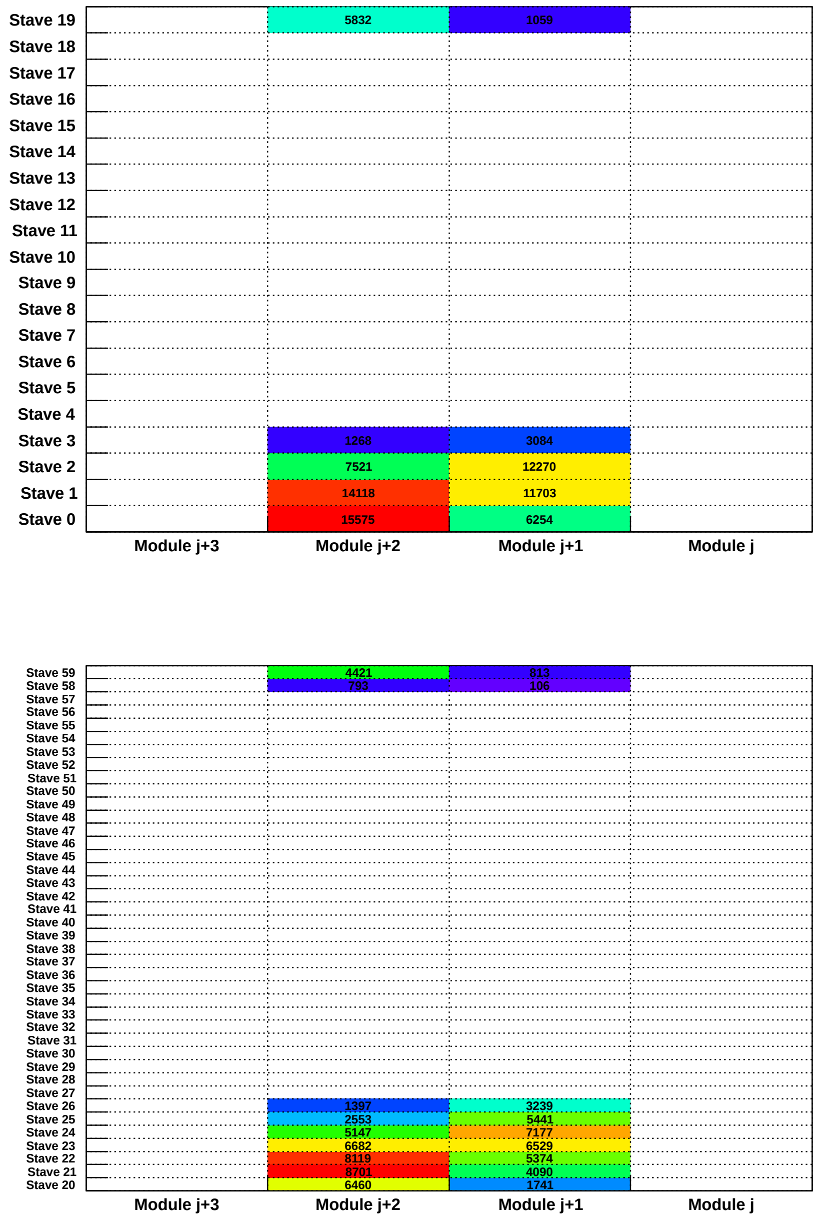

Figure D.4: *Inner (upper pannel) and outer (lower pannel) ITS modules in the HMPID acceptance are shown.*

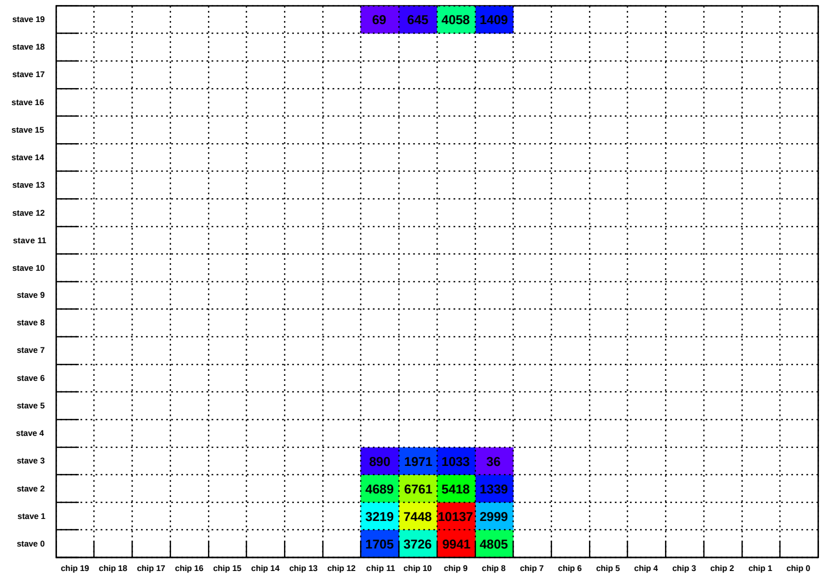

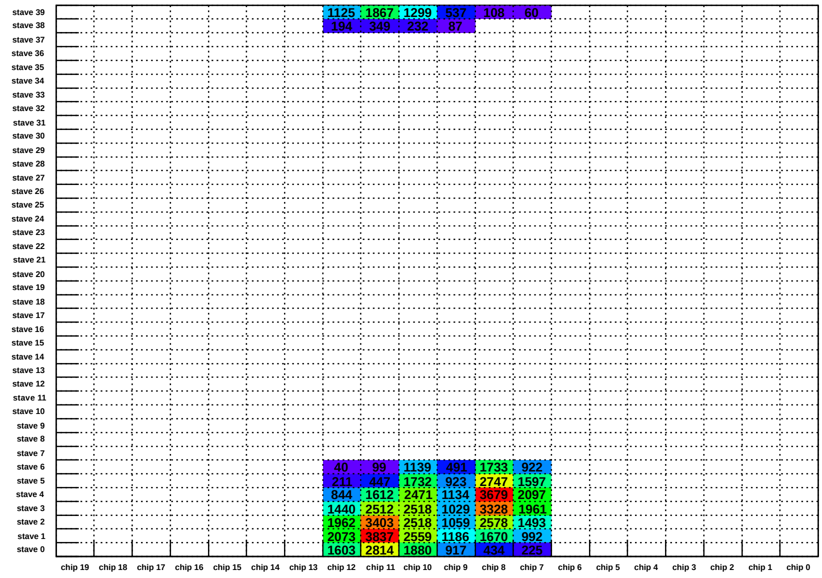

Figure D.5: *Fired chips in the inner layer (upper panel) and in the outer layer (lower panel) in HMPID acceptance.*

The determination of the module requests the information of the ϕ_{trk} (see Appendix B) and z_{global}, the z-axis in the global reference system [5]. The (inner and outer) SPD modules corresponding to the HMPID acceptance have been recorded: 10 (over 80) inner layer modules (L0) are interesting in the HMPID acceptance, while 18 (18/160) outer modules correspond to the HMPID acceptance. At this point, after a coordinate transformation (global to local),

$$z_{global} \quad -> \qquad z^{SPD}_{local}$$

the number of chips is provided (AliITSsegmentationSPD::GetChipFromLocal(parameter, z^{SPD}_{local})). Fig.D.4 and Fig.D.5 are useful graphic tools to understand which modules/chips are in the HMPID acceptance. On the x-axis there are the modules following the current SPD convention and on the y-axis the staves. The number that appears on each element of the grid represents the number of times that modules/chips are fired. The chips in the HMPID acceptance are recorded in a database. The simulation shows that about 20/400 (about 5 %) of the inner layer chips and 52/800 (about 6.5 %) of the outer layer chips correspond to the HMPID acceptance (see Fig.D.5). The low number of interesting chips selected is due to the great distance between SPD and HMPID (the HMPID is located at about 5 m from the primary vertex).

D.1.5 Chips correlation

The correlation between chips of the inner layer and chips of the outer layer in the acceptance of the HMPID has been carried out. A grid has been created: each element in the grid corresponds to a chip pairs ($chip^{L0}_i$, $chip^{L1}_j$) fired after the crossing

[5] In AliROOT, there is a class STEER with the following method

$$AliITSTrackleterSPDEff :: FindDetectorIndex(layer, \phi, z_{global}) \qquad (D.4)$$

used to retrieved the SPD modules.

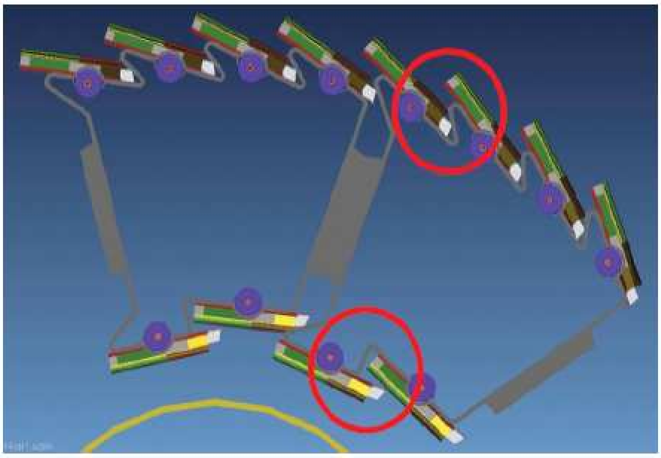

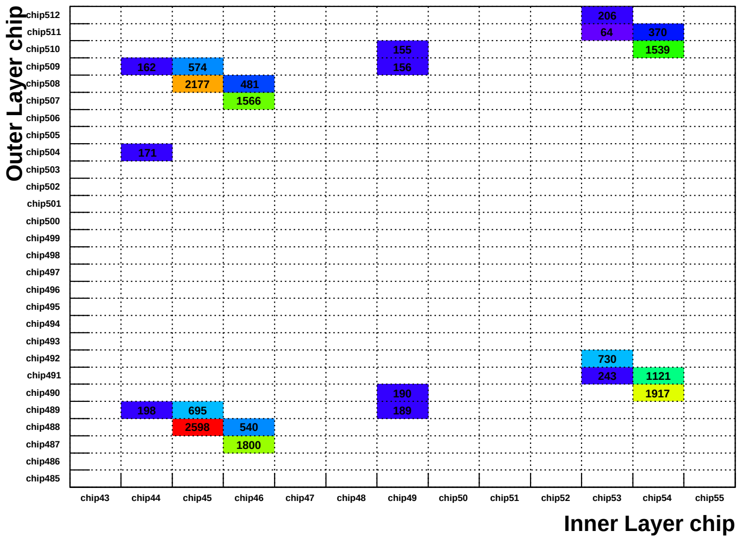

Figure D.6: *Upper panel: an example of correlation between chips (inner-outer layer). In the lower panel the selected couples ($chip_i^{L0}$, $chip_j^{L1}$) corresponding to the HMPID acceptance.*

of the track (see Fig. D.6, upper panel). In Fig.D.6 (lower panel) the correlation is shown: in the x-axis there are the inner layer chips while in the y-axis, the outer layer chips. It has been noticed that to each inner layer chip correspond up to 6 outer layer chips. Hence, all pairs of chips (chip$_i^{L0}$, chip$_j^{L1}$) have been retrieved and put in a database. The trigger algorithm to select tracks (and to reject events without tracks in the HMPID) is the following:

$$(chip_i^{L0}, chip_j^{L1})_{DATABASE} \quad \longrightarrow \quad Event \ \ selection$$

When a track crossed a (chip$_i^{L0}$, chip$_j^{L1}$) couple recorded in the database, the event is selected.

D.1.6 TOF plates selection

In this study, the TOF signal has been added, selecting the TOF plates in the geometrical acceptance of the HMPID. In this case, the procedure to select TOF plate is quite similar to the chip selection:

- plate selection in the HMPID acceptance;
- database creation;
- trigger scheme.

Only tracks that cross TOF plates and impact the HMPID chambers are taken into account. In Fig.D.7 TOF plates in the HMPID acceptance are shown. Sector 0, 1, 2 and 17 are in the HMPID acceptance. About 17 % (15/90) of TOF plates are in the HMPID acceptance: the track selection and then the event selection has been carried out:

$$PLATE_{DATABASE} \quad \longrightarrow \quad Event \ \ selection$$

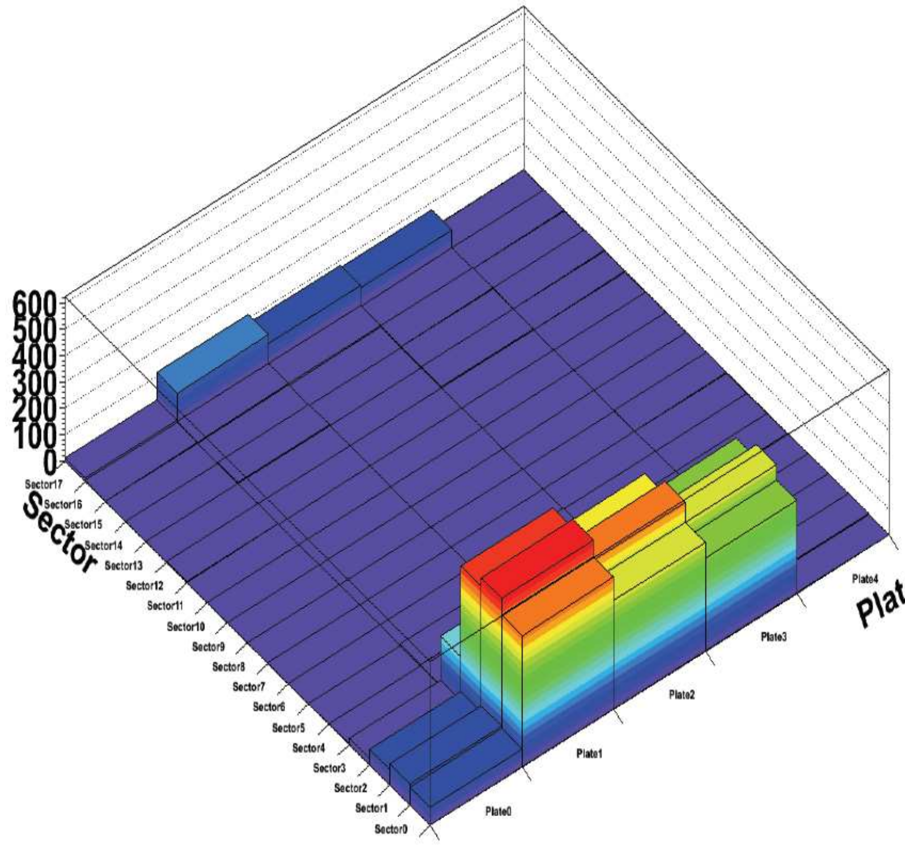

Figure D.7: *TOF plates in the HMPID acceptance. Sector 0, 1, 2, and 17 are in HMPID acceptance.*

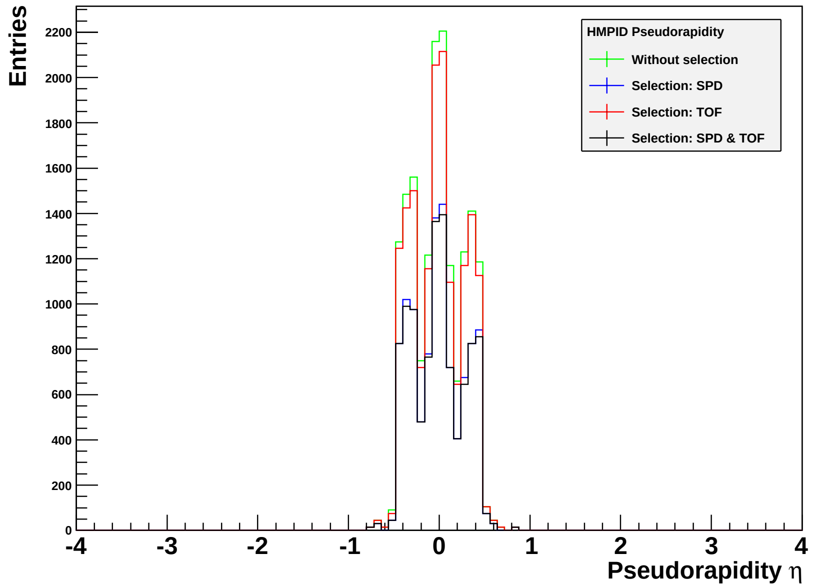

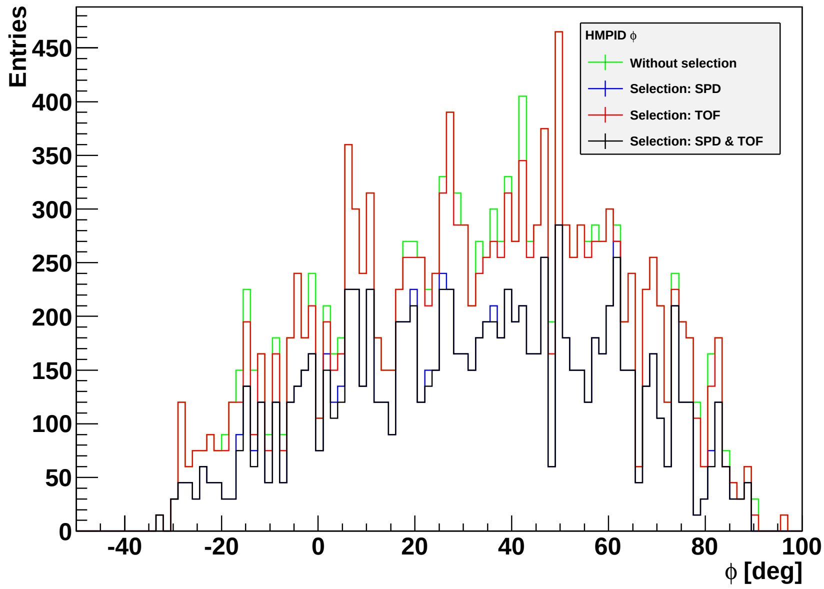

Figure D.8: *Pseudorapidity η (top) distribution for the tracks in the HMPID acceptance is shown. The three pecks correspond to the three chambers (one-dimensional projection), while the two empty regions are due to the dead zones between the chambers. Azimuthal angle (bottom) of the tracks in the HMPID acceptance as a function of events selection.*

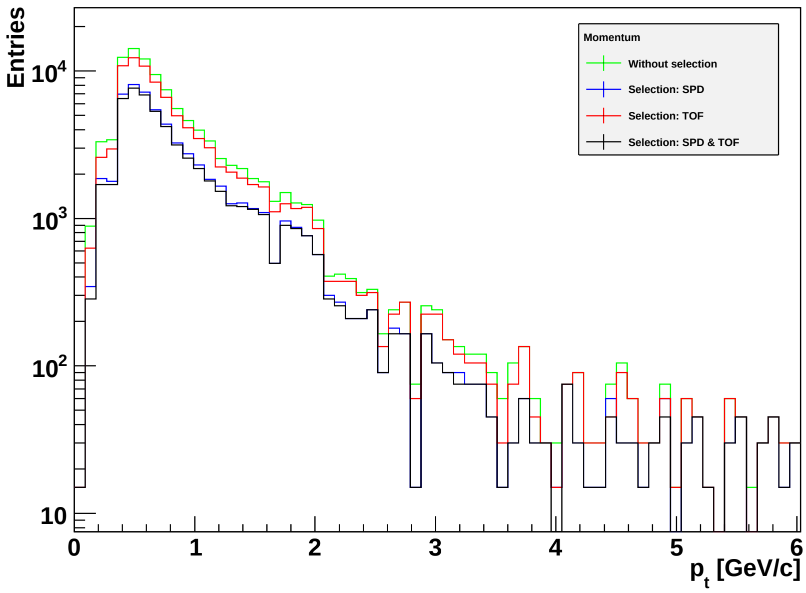

Figure D.9: *p_t distribution in the HMPID acceptance.*

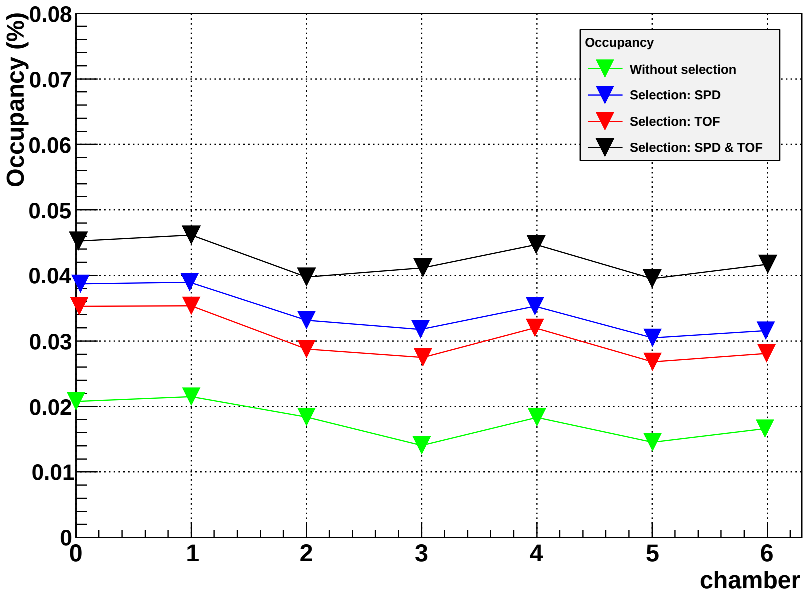

Figure D.10: *HMPID occupancy as a function of events selection.*

D.1.7 Trigger Performance

The interesting chips for the HMPID have been recorded and all the ($\text{chip}_i^{I.L.}$, $\text{chip}_j^{O.L.}$) correlations have been evaluated. The same procedure has been followed for the TOF plates.

$$SPD\ \&\ HMPID \longrightarrow Event\ \ selection$$

$$TOF\ \&\ HMPID \longrightarrow Event\ \ selection$$

$$SPD\ \&\ TOF\ \&\ HMPID \longrightarrow Event\ \ selection$$

The distortion effects introduced in the distribution of the kinematic variables are irrelevant as shown in Fig.D.8. In the upper panel the pseudorapidity η distribution (for the tracks in the HMPID acceptance) and in the lower panel the ϕ distribution (for the tracks in the HMPID acceptance) as a function of the events selection are shown. The three peaks are due to the dead zone between the chambers. The p_t spectra in the HMPID acceptance have been evaluated (Fig.D.9): the black line (SPD & TOF selection) and green line (without selection) are closer for momenta above 3 GeV/c because of the selection of tracks with higher momenta. The SPD trigger condition selects the 35% of events, while the TOF selects 57 % of events. Combining the SPD and TOF signal the number of selected events drops to 25%. A relevant parameter for the HMPID is the number of tracks per event: the increase of the tracks number with only SPD selection is a factor of about two (same factor using only TOF) and the increase of the tracks number with SPD and TOF is about a factor three. This means, we reject events without track in the HMPID. A simple performance analysis (for example, alignment, calibration and check on tracking algorithm of the HMPID) could result faster using this proposed trigger scheme. Moreover, the behavior of the HMPID occupancy has been checked. It is defined as the ratio between the fired pads over the total pads, $\text{Occupancy}_{HMPID} = \text{N}_{fired-pads}/\ \text{N}_{total-pads}$. The total number of pads is $N_{total\ pads} = 161280$, as described in the Chapter 2. The occupancy as a function of event selections has been shown in Fig.D.10. Again, this parameter increases by a factor 2 if the SPD and TOF selection are used.

The trigger algorithm implementation is a more complex phase and several steps are necessary. This study represents a first step. The Monte-Carlo simulation shows that it is possible to perform a selection of good events for HMPID (i.e. events with at least one track in its acceptance) using the combined signal from SPD and TOF, improving some important parameters (occupancy, the number of tracks per event) and introducing irrelevant distortion effects in the distributions of the kinematic variables. Although the trigger does not show excellent factor gain (about 3), it could well be applied for performance studies, for example in alignment, calibration or on tracking algorithm studies of the HMPID, where great amount of MB events to analyze is needed.

Bibliography

[1] F. Karsch, Nucl. Phys. A 698, 199c (2002).

[2] Z. Fodor, Nucl. Phys. A 715, 319c (2003).

[3] G. F. Chapline et al, Phys. Rev. D 8, 4302 (1973).

[4] J. D. Bjorken, Phys. Rev. D 10, 2445 (1974).

[5] B. Muller and J. Rafelski, Phys. Rev. Lett. 48, 1066 (1982).

[6] T. Matsui and H. Satz, Phys.Lett. B 178, 416 (1986).

[7] ALICE Collaboration, ALICE Physics Performance Report, Volume I, J. Phys. G: Nucl. Part. Phys. **30** (2004) 1517

[8] ALICE Collaboration, ALICE Physics Performance Report, Volume II, J. Phys. G: Nucl. Part. Phys. **32** (2006) 1295

[9] James L Nagle et al 2011 New J. Phys. 13 075004 doi:10.1088/1367-2630/13/7/075004;

[10] Blaizot; Iancu; Rebhan (2003) Thermodynamics of the high-temperature quark-gluon plasma arXiv:hep-ph/0303185;

[11] Bohr, Henrik; Nielsen, H. B. (1977), Hadron production from a boiling quark soup: A thermodynamical quark model predicting particle ratios in hadronic collisions Nuclear Physics B 128 (2): 275. Bibcode 1977NuPhB.128..275B

[12] airXiv:hep-ph/0407360 v1 30 Jul 2004;

[13] arXiv:1012.1004v1 [nucl-ex] 5 Dec 2010;

[14] Eur.Phys.J.C 71(6): 1655, 2011, DOI:10.1140/epjc/s10052-011-1655-9.

[15] Phys Rev Lett Vol.105, No.7, (2010)

[16] http://user.web.cern.ch/public/en/About/History71-en.html

[17] http://www.bnl.gov/rhic/

[18] J. Adams *et al.* (STAR Collaboration), Nucl. Phys. A **757** (2005) 102

[19] K. Adcox *et al.* (PHENIX Collaboration), Nucl. Phys. A **757** (2005) 184

[20] B. B. Back *et al.* (PHOBOS Collaboration), Nucl. Phys. A **757** (2005) 28

[21] I. Arsene *et al.* (BRAHMS Collaboration), Nucl. Phys. A **757** (2005) 1

[22] Roberto Preghenella (for the ALICE Collaboration) The 2011 Europhysics Conference on High Energy Physics, EPS-HEP 2011, July 21-27, 2011 Grenoble, Rhône-Alpes, France;

[23] Schnedermann, J. Sollfrank and U. Heinz, Phys. Rev. C48, 2462 (1993);

[24] http://arxiv.org/PS-cache/arxiv/pdf/0812/0812.1609v2.pdf

[25] J. Adams et al. (STAR), Nucl. Phys. A757, 102 (2005), nucl-ex/0501009.

[26] K. Adcox et al. (PHENIX), Nucl. Phys. A757, 184 (2005), nucl-ex/0410003.

[27] M. Gyulassy and L. McLerran, Nucl. Phys. A750, 30 (2005), nucl-th/0405013.

[28] B. Muller (2004), nucl-th/0404015.

[29] J. Adams et al. (STAR), Phys. Rev. Lett. 92, 112301 (2004), nucl-ex/0310004.

[30] E. Schnedermann, J. Sollfrank, and U. W. Heinz, Phys. Rev. C48, 2462 (1993), nucl-th/9307020.

[31] F. Retiere and M. A. Lisa, Phys. Rev. C70, 044907 (2004), nucl-th/0312024.

[32] S. A. Voloshin, A. M. Poskanzer, and R. Snellings (2008), 0809.2949.

[33] J. Adams et al. (STAR), Phys. Rev. Lett. 92, 182301 (2004), nucl-ex/0307024.

[34] S. S. Adler et al. (PHENIX), Phys. Rev. C69, 034909 (2004), nucl-ex/0307022.

[35] http://indico.cern.ch/getFile.py/access?contribId=469-sessionId=6-resId=0-materialId=slides-confId=30248;

[36] http://indico.cern.ch/confAuthorIndex.py?view=full-letter=k-confId=30248;

[37] L. Evans and P. Bryant (editors), JINST **3** (2008) S08001

[38] lhc.web.cern.ch/;

[39] LHC commissioning with beam. CERN. Retrieved 2009-04-17.

[40] http://op-webtools.web.cern.ch/op-webtools/vistar/vistars.php

[41] http://atlas.ch/

[42] http://cms.web.cern.ch/

[43] http://lhcb.web.cern.ch/lhcb/

[44] http://user.web.cern.ch/public/en/LHC/LHCf-en.html

[45] http://totem.web.cern.ch/Totem/

[46] http://web.me.com/jamespinfold/MoEDALsite/Welcome.html

[47] F. Prino [ALICE Collaboration], Nucl. Phys. A830, (2009) 527C; R. Santoro et al. [ALICE Collaboration], JINST 4, (2009) P03023; P. Christakoglou et al. [ALICE Collaboration], PoS (EPS-HEP 2009) 124; K. Aamodt et al. [ALICE Collaboration], JINST 5(2010) P03003.

[48] J. Alme et al. [ALICE Collaboration], arXiv:1001.1950 [physics.ins-det].

[49] http://aliceinfo.cern.ch/Public/en/Chapter2/Chap2TOF.html

[50] https://edms.cern.ch/document/460192/1

[51] http://www-alice.gsi.de/trd/

[52] http://www-alice.gsi.de/trd/tdr/index.html

[53] http://www.panic05.lanl.gov/abstracts/466/proc466PHOSproceedings4PANIC05v26.pdf

[54] https://trac.cc.jyu.fi/projects/alice/wiki/EMCAL

[55] http://aliceinfo.cern.ch/Public/en/Chapter2/Chap2dimspec.html.

[56] http://aliceinfo.cern.ch/Public/en/Chapter2/Chap2ZDC-en.html.

[57] http://www.phy.iitb.ac.in/basanta/publichtml/pmd/ALICE/Software/

[58] http://aliceinfo.cern.ch/Public/en/Chapter2/Chap2FMD.html

[59] K. Aamodt et al. [ALICE Collaboration], JINST 3, (2008) S08002.

[60] https://www.jyu.fi/fysiikka/en/research/accelerator/alice/detector.html

[61] R. Brun et al., 1985 GEANT3 User Guide, CERN Data Handling Division DD/EE/841; R. Brun et al., 1994 CERN Program Library Long Write- up, W5013, GEANT Detector Description and Simulation Tool.

[62] ALICE Collaboration, AliRoot, ALICE Offline simulation, reconstruction and analysis framework, http://aliceinfo.cern.ch/Offline/

[63] http://aliweb.cern.ch/Offline/AliRoot/Manual.html.

[64] http://root.cern.ch

[65] X. N. Wang and m. Gyulassy, Phys. Rev. D **44** (1991) 3501
M. Gyulassy and X. N. Wang, Comput. Phys. Commun. **83** (1994) 307
http://www-nsdth.lbl.gov/˜xnwang/hijing

[66] H.U. Bengtsson and T. Sjostrand, Comput. Phys. Commun. **46** (1987) 43
http://www.thep.lu.se/˜torbjorn/Pythia.html

[67] R. Engel, J. Ranft and S. Roesler, Phys. Rev. D **52** (1995) 1459

[68] S. Agostinelli *et al.*, Geant 4, *A Simulation Toolkit*, CERN-IT-20022003

[69] http://geant4.cern.ch/

[70] http://www.fluka.org; A. Fasso, A. Ferrari, J. Ranft, P.R. Sala, "FLUKA: a multi-particle transport code", CERN-2005-10 (2005), INFN/TC05/11, SLAC-R-773; G. Battistoni, S. Muraro, P.R. Sala, F. Cerutti, A. Fer- rari, S. Roesler, A. Fasso, J. Ranft, "The FLUKA code: Description and benchmarking", AIP Conference Pro- ceeding 896, (2007) 31.

[71] CERN / LHCC 9819, ALICE TDR 1, 14 August 1998.

[72] P.Martinengo et al., Nucl.Instrum.Meth. A639 (2011) 7-10.

[73] A. Di Mauro et al. ALICE Internal Note 2007-003.

[74] http://alice-hmpid.web.cern.ch/alice-hmpid/

[75] http://alice-hmpid.web.cern.ch/alice-hmpid/intnotes.htm

[76] http://aliceinfo.cern.ch/Public/en/Chapter2/Chap2-HMPID-en.html;

[77] E. Nappi, The CsI-RICH detector for high momentum hadron identification in the ALICE experiment at CERN- LHC, Proceedings of the XLII International Winter Meeting on Nuclear Physics, 25-31 January 2004, Bormio, Italy - Suplemento n.123 Ricerca Scientifica ed Educazione Permanente, Università degli Studi di Milano;

[78] DOI: 10.1063/1.2823853 arXiv: 0801.2695;

[79] http://villaolmo.mib.infn.it/ICATPP13th-2011/pending-for-corrections/Adv-Det-Part-Id/Molnar-Article.pdf;

[80] The STAR-RICH Detector, CERN-ALICE-PUB-2001-10;

[81] Nuclear Instruments and Methods in Physics Research Section A, Volume 486, Issue 3, p. 590-609.

[82] http://alice-hmpid.web.cern.ch/alice-hmpid/publicns/NPHYSA698.pdf;

[83] http://cdsweb.cern.ch/record/494443/;

[84] http://alice-hmpid.web.cern.ch/alice-hmpid/publicns/ali-2001-010.pdf;

[85] http://www.sciencedirect.com/science/article/pii/S0168900202019691;

[86] http://www.ep.ph.bham.ac.uk/twiki/bin/view/ALICE/AliceTriggerIntroduction;

[87] Nuclear Instruments and Methods in Physics Research A 602(2009) 372-376.

[88] F. Barile (Bari U. and INFN, Bari) for the ALICE collaboration, Published in Nucl.Phys.Proc.Suppl. 215 (2011) 215-217.

[89] Eur. Phys. J. C 71 (3), 1594 (2011) DOI:10.1140/epjc/s10052-011-1594-5.

[90] J. Podolanski and R. Armenteros. Phil. Mag., 45(13), 1954

[91] http://alice-hmpid.web.cern.ch/alice-hmpid/

[92] R.E. Ansorge et al.(UA5 Collaboration),Phys. Lett. B 199, 311 (1987).

[93] B.I.Abelev et al.(STAR Collaboration), Phys.Rev.C79,034909(2009). arXiv:0808.2041.

[94] A. Adare et al. (PHENIX Collaboration), 2010,

[95] ALICE900) arXiv:1005.3674. Eur.Phys.J.C 71(6): 1655, 2011 DOI:10.1140/epjc/s10052-011-1655-9

[96] Phys Rev Lett Vol.105, No.7, (2010)

[97] arXiv:nucl-ex/0607033v1

[98] G.C. Rossi and G. Veneziano, Nucl. Phys. B123, (1977) 507.

[99] A. Capella et al. Phys. Rep. 236, 225 (1994); A.B. Kaidalov and K.A. Ter-Martirosyan, Sov. J. Nucl. 411 Phys. 39, 1545 (1984).

[100] X. Artru, Nucl. Phys. B85, (1975); M. Imachi, S. Otsuki and F. Toyoda Prog. Theor. Phys. 52, (1974); Prog. Theor. Phys. 54, 280 (1975).

[101] B.Z. Kopeliovich, Sov. J. Nucl. Phys. 45, 1078 (1987); B.Z. Kopeliovich, B. Povh, Z. Phys. C75, 693 (1997); B.Z. Kopeliovich, B. Povh, Phys. Lett. B446, 321 (1999).

[102] D. Kharzeev, Phys. Lett. B378, 238 (1996).

[103] C. Merino et al. Eur.Phys.J. C54 577 (2008); C. Merino, M.M. Ryzhinskiy, Yu.M. Shabelski, arXiv:0906.2659.

[104] S. E. Vance and M. Gyulassy, Phys. Rev. Lett. 83, 1735 (1999).

[105] P. Christakoglou et al., ALICE Internal Note ALICE-INT-2008-010 (2008); P. Christakoglou et al. ALICE Collaboration, PoS (EPS-HEP 2009) 405.

[106] Eur.Phys. J. C (2010) 68: 345-354 DOI 10.114/epjc/s10052-010-1350-2;

[107] arXiv:1004.3034v2 [hep-ex] 6 May 2010;

[108] C. Tsallis, J.Stat. Phys. 52, 479 (1988);

[109] B.I. Abelev et al. (STAR Collaboration), Phys. Rev. C75, 064901, (2007). airXiv:nucl-ex/0607033;

[110] G. Bocquet et al., Phys. Lett. B 366, 441 (1996)

[111] R.E. Ansorge et al (UA5 Collaboration), Nucl. Phys. B 328, 36 (1989).

[112] R.E. Ansorge et al (UA5 Collaboration), Nucl. Phys. B 119, 311 (1987).

[113] R. Hagedorn, Riv. Nuovo Cimento 6, n. 10, 1, (1984).

[114] Mandelstam, S. (1958). Determination of the Pion-Nucleon Scattering Amplitude from Dispersion Relations and Unitarity. Phys. Rev. 112, 1344. DOI:10.1103/PhysRev.112.1344.

List of Figures

List of Tables